Techniques de haute résolution pour l'imagerie GPR en champ proche et à large bande

Pamela Manase

COLLEGE DOCTORAL BRETAGNE

MATHS, TELECOMS
INFORMATIQUE, SIGNAL
SYSTEMES, ELECTRONIQUE

Université de Rennes

THESE DE DOCTORAT DE

L'UNIVERSITE DE RENNES 1

ECOLE DOCTORALE N° 601
Mathématiques, Télécommunications, Informatique, Signal, Systèmes, Electronique
Spécialité : *Télécommunications*

Par

Pamela MANASE

Techniques de Haute Résolution en Champ Proche et à Large Bande pour l'Imagerie Géoradar

Near Field and Wide Band High Resolution Techniques for Ground Penetration Radar Imaging

Thèse présentée et soutenue à Grenoble, le 6 octobre 2023

Unité de recherche : IETR et CEA-Leti

Rapporteurs :

	Hervé AUBERT	Professeur à INP Toulouse-ENSEEIHT - LAAS - CNRS
	Xavier DEROBERT	Co-directeur du laboratoire GeoEND - GERS - Université Gustave Eiffel

Jury :

Président :	Bernard UGUEN	Professeur à l'Université de Rennes 1 - IETR - CNRS - Dir. adjoint de ESIR
Examinateurs :	Michèle LALANDE	Professeur à l'Université de Limoges - Laboratoire XLIM
	Tullio TANZI	Professeur à Télécom Paris
Dir. de thèse :	Laurent FERRO-FAMIL	Professeur à ISAE-SUPAERO à l'Université de Toulouse - DEOS - CESBIO
Encadrant de thèse :	Raffaele D'ERRICO	Ingénieur de recherche au CEA-Leti Grenoble

to my amazing Father Rev. Manase and my gorgeous Mother Rev. Jenifa

to my lovely young sisters M.D. Raisa, Carina and Nadine

"Whatever Your Mind Can Conceive and Believe, It Can Achieve"

Napoleon Hill

Acknowledgements

First and foremost, I would like to express my profound gratitude to the Almighty for His unwavering presence, providing the foundation upon which I have lived, moved, and found my purpose.

I extend my warmest appreciation to my two thesis directors, Professor Laurent Ferro-Famil, a distinguished University Professor at ISAE Supaero of the University of Toulouse, and Dr. Raffaele D'Errico, an accomplished Research Engineer and Project Manager at CEA Grenoble. Their exceptional support, mentorship, wealth of experience, boundless enthusiasm, and profound scientific expertise have been instrumental in bringing this study to fruition.

I am equally indebted to Mr. Dimitri Ktenas, the head of the wireless service and Dr. Christophe Delavaud the Head of the LAPCI Laboratory from CEA for providing me with an excellent and congenial research environment that fostered my thesis work. I am deeply appreciative of CEA Leti Grenoble for providing funding during the course of my thesis.

I wish to express my sincere appreciation to Professor Hervé Aubert, and Dr. Xavier Derobert for graciously agreeing to assess and serve as rapporteurs for this work. My gratitude extends to Professor Bernard Uguen, Professor Michelle Lalande, and Professor Tullio Tanzi for their willingness to be part of the thesis jury.

Special thanks go to Dr. Gloria Makhoul and Mathieu Caillet for their invaluable guidance during various experiments. I wish to highlight Dr. Gloria Makhoul's active involvement in the discussions related to my thesis and her consistent moral support over these three years.

I owe a debt of gratitude to the entire University of Rennes 1 and IETR lab team, particularly Madam Marie Hubert and Elodie Cottrel, for their kindness and exceptional efficiency in navigating administrative and logistical challenges.

My heartfelt thoughts extend to all the doctoral students and colleagues with whom I have shared not only a room but also countless cups of coffee, meals, and

sports activities throughout these transformative three years.

Lastly, I extend immense thanks to my family – my father, Rev. Manase, my mother, Rev. Jenifa, and my cherished younger sisters, M.D. Raisa, Carina, and Nadine. Their nurturing love, unwavering motivation, and steadfast support have been my constant companions on this journey.

Last but certainly not least, I want to express my deep appreciation to my pillar of strength, Emeric, for consistently being my anchor, a comforting presence, and an unwavering source of support whenever I needed it.

COLLEGE MATHS, TELECOMS
DOCTORAL INFORMATIQUE, SIGNAL
BRETAGNE SYSTEMES, ELECTRONIQUE

Université de Rennes

Titre : Techniques de haute résolution pour l'imagerie GPR en champ proche et à large bande

Mot clés : *Géoradar, Techniques d'analyse spectrale, GPR techniques de focalisation, Synthetic Aperture.*

Résumé : Un géoradar est un système d'imagerie non destructif capable de détecter des cibles dans un milieu diélectrique hétérogène. La réponse 2D de la cible mesurée par le géoradar pendant l'acquisition du B-scan a la forme d'une hyperbole en raison des différents trajets d'onde qui sont fonction du déplacement. Par conséquent, des techniques de focalisation sont nécessaires pour localiser la position réelle de la cible. La résolution des méthodes de focalisation géoradar conventionnelles est limitée par la largeur de bande du signal ainsi que par l'ouverture synthétique du réseau. Par conséquent, lorsque les cibles sont séparées par une distance inferieure a la résolution de Fourier, celles-ci ont tendance à être interprétées comme une seule cible en raison de la faible résolution spatiale des méthodes de focalisation géoradar conventionnelles. Dans ce travail, des techniques d'analyse spectrale adaptées à l'origine a des applicatifs champ lointain a bande étroite sont proposées pour surmonter la limitation de résolution des méthodes d'imagerie géoradar conventionnelles. L'utilisation de techniques d'analyse spectrale avec des données bande en champ proche nécessite des ajustements significatifs qui seront couverts dans cette étude. Les résultats obtenus montrent que les méthodes d'analyse spectrale ont permis d'augmenter de manière significative la résolution dans les directions de l'élévation et de l'azimut. Ceci a été démontré par leur capacite à séparer des cibles dont la distance de séparation des cibles était inferieure a la résolution de Fourier. En outre, nous avons montré que grâce à la capacite de résolution de focalisation élevée des méthodes spectrales, il était possible d'estimer les cibles avec précision malgré une taille réduite du réseau d'antennes ainsi que de la bande passante (jusqu'à une demi-bande) respectivement. De plus, les performances de précision d'estimation entre les méthodes classiques de focalisation géoradar (qui dépendent de la résolution de Fourier) et les techniques d'analyse spectrale (qui dépendent de l'estimation de précision des données de la matrice de covariance) ont été comparées et analysées. Enfin, les algorithmes proposes ont été testes dans un scenario réel en les appliquant aux données expérimentales de mesure géoradar.

COLLEGE MATHS, TELECOMS
DOCTORAL INFORMATIQUE, SIGNAL
BRETAGNE SYSTEMES, ELECTRONIQUE

Université de Rennes

Title: Near Field Wide Band High Resolution Techniques for GPR Imaging

Keywords: *Ground Penetration Radar, Spectral analysis techniques, GPR focusing techniques, Synthetic Aperture.*

Abstract: Ground Penetrating Radar (GPR) is a non-destructive imaging system that is able to detect targets in heterogeneous dielectric medium. The 2D response of target measured by GPR during B-scan acquisition is in form of hyperbola shape due to the different wave paths as a function of displacement. Hence, focusing techniques are required to localize the true position of the target. Resolution of conventional GPR focusing methods are limited by signal bandwidth and array synthetic aperture. As a consequence, when the targets are separated by a distance which is less than Fourier resolution, they tend to be interpreted as a single target due to poor spatial resolution of the conventional GPR focusing methods. In this work, spectral analysis techniques that are originally adapted to narrow band far field are proposed to overcome resolution limitation of conventional GPR imaging methods. The use of spectral analysis techniques with GPR data that are acquired in near field wide band configuration requires significant adjustments which will be covered in this study. The obtained results exhibit that, spectral analysis methods were able to increase significantly the resolution along range and azimuth directions. This was demonstrated by their ability to separate targets with offset distance that was less than Fourier resolution. Furthermore, we showed that thanks to high focusing resolution capability of spectral methods, it was possible to estimate targets accurately with a reduced size of azimuth sampling positions and bandwidth respectively. In addition to this, estimation accuracy performances between classical focusing GPR methods (which depend on Fourier resolution) and spectral analysis techniques (which depend on accuracy estimation of covariance matrix data) were compared and analysed. Finally, our proposed algorithms were tested in real life scenario by applying them on GPR measurement data.

Contents

List of Figures

List of Tables

Acronyms

GPR Ground Penetrating Radar
SISO Single Input Single Output
SIMO Single Input Multiple Outputs
MISO Multiple Inputs Single Output
MIMO Multiple Inputs Multiple Outputs
SCR Signal-to-ClutterRatio
RCS Radar Cross Section
FDTD Finite-Difference Time-Domain
MUSIC Multiple Signal Classification
FT Fourier Transform
FFT Fast Fourier Transform
IFT Inverse Fourier Transform
IFFT Inverse Fast Fourier Transform
HS Hyperbolic Summation
PSM Phase Shift Migration
F-k Frequency-wavenumber
BP Back Projection
ESM Explosive Source Model
CTF Channel Transfer Function
Specan Spectral Analysis

Introduction

Remote sensing techniques can non-destructively detect object inside visually opaque media, such as environments located underneath the ground surface or inside a human body. Among the applications of remote sensing techniques is object detection in heterogeneous medium by using Ground Penetration Radar (GPR). GPR works by emitting an electromagnetic signal into the ground and the electromagnetic wave propagates through the opaque medium and when impinges a buried target a back-scattered electromagnetic field arises (Fig. 1).

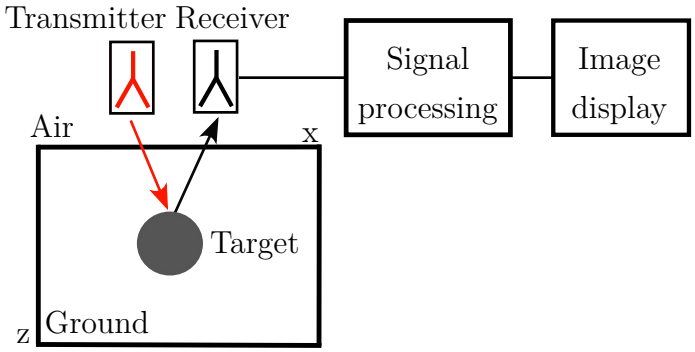

Figure 1: GPR measuring principle

GPR has gained its fame thanks to its high resolution capability and applicability for detecting mines and unexploded ordinances, finding water leakages, investigating archaeological substances, spotting asphalt/concrete cracks in highways, searching buried victims after an earthquake or an avalanche, and imaging behind the wall for security applications. Depending on the application, different scanning schemes, namely, A-scan, B-scan, and C-scan, can be employed (Fig. 2).

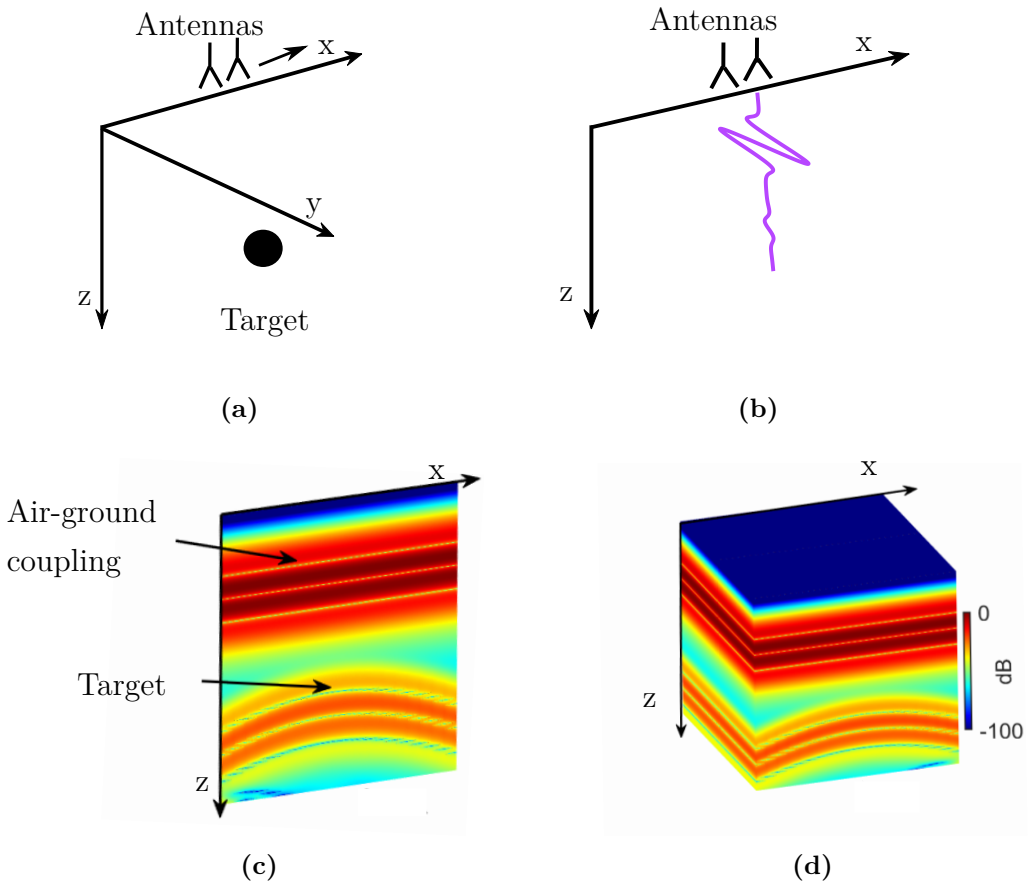

Figure 2: GPR operating modes: (a) Geometry configuration, (b) A-scan, (c) B-scan, and (d) C-scan.

In the B-scan measurement situation, a downward looking GPR antenna is moved along a straight path on the top of the surface while the GPR sensor is collecting and recording the scattered field at different spatial positions. This static measured data collected at single point is called an A-scan.

The GPR back-scattered field during B-scan acquisition shows up as a hyperbola due to the different paths of the waves as a function of displacement. Hence, focusing techniques such as back-projection (BP) or migration ω-k are necessary to estimate the real position and the real shape of the target. However, the performance of these focusing methods in terms of spatial resolution is limited by the spectral bandwidth and the dimensions of the synthetic aperture of the GPR. To overcome this problem, imaging techniques based on inverse scattering or high-

resolution spectral analysis (Specan) techniques can be used to improve spatial resolution. The use of these techniques with non-planar, i.e. in the near-field (region that is close to an antenna based on Fraunhofer distance) waves modulated by wide band signals, requires significant adjustment. When GPR data are acquired over a large physical aperture, and use wide-band signals, the variation in range between the radar and a measured object evolves in a non-linear manner (i.e hyperbola shape in space time GPR image) and can exceed the range resolution value, creating migrations corresponding to a two-dimensional spread of the measured signal. Since the Specan methods studied use the covariance matrix of a restricted range cell or azimuth cell of the GPR data, the selected vector will provide only a portion of the phase history of the target response. This leads to artefacts and reduced performances, including a noticeable decrease of the discrimination capacity.

In this study, we focus on improving both range and azimuth resolution. To do this, compensation of near field and wide band effects has to be done first using a GPR focusing algorithm before applying focusing solutions using Specan methods. In addition to that, we increase number of looks along azimuth direction by using 2D spectral smoothing.

This thesis is arranged as follows. Imaging of object embedded in dielectric medium introduced in Chapter 1. Chapter 2 presents high resolution 2D GPR imaging using spectral analysis techniques. Then in Chapter 3, implementation of spectral analysis technique on GPR measured data. Finally, The conclusion and perspective are introduced in Chapter 4.

Résumé détaillé

Contents

0.1 Introduction

Dans ce travail, nous présentons une analyse des techniques d'analyse spectrale combinées aux méthodes de migration dans les systèmes de géoradar. Nous nous concentrons sur l'amélioration de la détection des cibles proches, qui est limitée par la bande-passante du signal ainsi que la longueur de l'ouverture synthétique pour les techniques d'imagerie conventionnelles. L'augmentation de la résolution azimutale est illustrée par la capacité à distinguer des cibles séparées par une distance inférieure à la résolution azimutale de Fourier dans des configurations à large bande en champ proche, tant pour les résultats simulés que pour les données mesurées.

0.2 Techniques d'imagerie classiques

Dans une image géoradar à B-scan spatio-temporel typique, tout diffuseur situé dans la région de l'image apparaît sous la forme d'une hyperbole. L'objectif des techniques d'imagerie classiques (techniques de migration) est de ramener les échos présents dans les données enregistrées à la position réelle et à la forme physique de la cible. Les techniques de migration étudiées sont la migration par sommation hyperbolique (diffraction), la migration par déphasage, la migration par nombre de fréquences et l'algorithme de rétroprojection (BP). Un bon aperçu de ces techniques est donné dans [Özd+14].

Les résultats de simulation des techniques d'imagerie classiques pour les scénarios azimutal et en distance permettent de tirer les conclusions suivantes. Tout d'abord, l'algorithme de focalisation BP a été en mesure de distinguer les cibles séparées par un décalage supérieur à la résolution en distance ou azimutale (Fig. 3a).

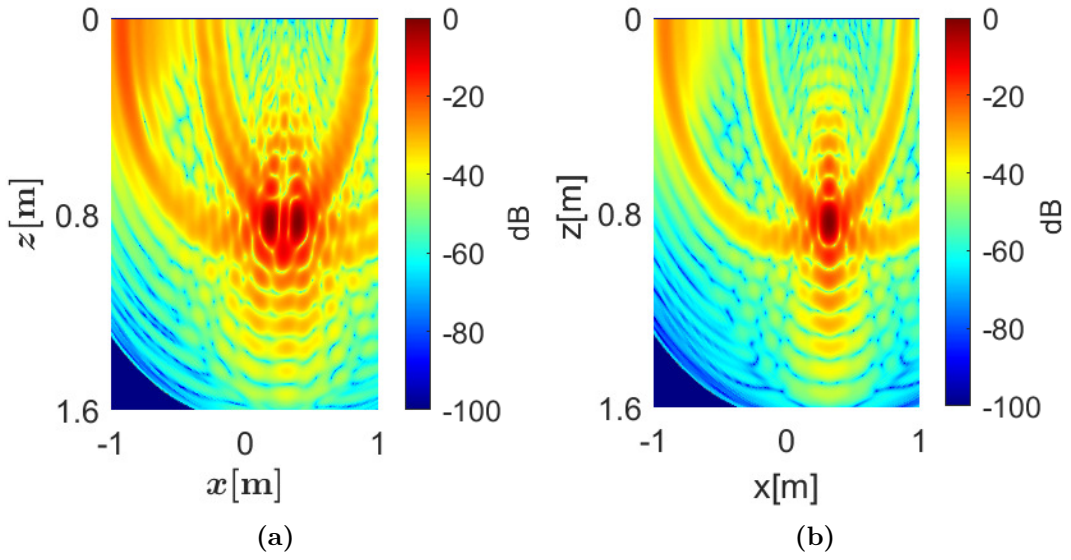

Figure 3: Scénario avec 2 cibles localisées au centre du réseau et 20 positions d'échantillonnage azimutales : (a) résultats focalisés BP pour $dx = 20$ cm et (b) résultats focalisés BP pour $dx = 4.75$ cm.

Lorsque la séparation est réduite, c'est-à-dire inférieure à la résolution en distance ou azimutale, l'algorithme de focalisation BP ne parvient pas à distinguer les cibles et les interprète comme une seule cible. En effet, les performances de résolution de la méthode géoradar classique sont limitées par la bande-passante

du signal et la taille de l'ouverture synthétique (nombre d'éléments d'antenne), comme le montre la Fig. 3b dans le cas de la résolution en azimut.

Afin de surmonter la limitation en résolution des méthodes conventionnelles de mise au point du géoradar, la littérature propose plusieurs solutions qui incluent l'application de la configuration MIMO et les techniques d'analyse spectrale. Bien que la configuration MIMO puisse améliorer la résolution, des ressources matérielles supplémentaires sont nécessaires, y compris l'adaptation des méthodes de traitement des signaux pour pouvoir traiter les données acquises avec la configuration MIMO. Les techniques d'analyse spectrale sont connues pour leurs capacités d'estimation à haute résolution. Les méthodes Specan étudiées sont des algorithmes basés sur les données de la matrice de covariance, comme indiqué dans le Tab. 1 et détaillé dans l'annexe A.

Table 1: Liste des acronymes des méthodes de Specan

Acronyme	**Méthode Specan**
BF	Beamforming [SM+05] [CGY10] [KV96]
CP	Capon beamforming method [SM+05] [CGY10] [KV96]
MUSIC	MUltiple SIgnal Classification [SM+05] [KV96] [WKL14]
OPM	Orthogonal Projector Method [Sun+19] [Mar+98]
MUroot	Root-MUSIC [SM+05] [KV96] [WKL14]
OPMroot	Root-OPM [Mar+98]
ESPRIT	Estimation of Signal Parameters via Rotational Invariant Techniques [SM+05] [KV96] [WKL14]
DML	Deterministic Maximum Likelihood [SM+05] [KV96]
SSF	Signal Subspace Fitting [SM+05] [KV96]

Les méthodes Specan sont choisies dans ce travail pour améliorer la résolution car ce sont des techniques de traitement du signal qui peuvent être utilisées pour améliorer les ressouces matérielles existantes. Toutefois l'utilisation des techniques Specan avec une configuration d'ondes non planes, c'est-à-dire à champ proche et à large bande-passante, nécessite une réadaptation significative des données géoradar.

Les principaux défis liés à la mise en œuvre de Specan sur les données géoradar dans la direction azimutale sont les suivants. Tout d'abord, les données géoradar sont acquises dans un champ proche à large bande-passante. Les effets

large-bande en champ proche font que les données se comportent de manière non linéaire, c'est-à-dire qu'elles prennent la forme d'une hyperbole. Par conséquent, étant donné que les méthodes Specan étudiées utilisent une cellule à portée ou cellule azimutale restreintes, l'utilisation des méthodes Specan directement sur les données géoradar peut entraîner une diminution de la capacité de discrimination. Il est donc nécessaire d'adapter les données géoradar obtenues dans un champ proche à large bande-passante afin d'améliorer la capacité de résolution des méthodes de Specan. Deuxièmement, les méthodes de Specan exigent que les données soient non ou partiellement décorrélées. Dans ce travail de recherche, nous avons utilisé une méthode de lissage spectral 2D qui permet de conserver un réseau de longueur inchangée.

0.3 Imagerie géoradar 2D à haute résolution par des techniques d'analyse spectrale

La modélisation de la propagation des scénarios géoradar est ici présentée. La modélisation de scénarios permet de comprendre l'interaction complexe entre les ondes électromagnétiques et la cible. La méthode de modélisation FDTD est choisie dans ce travail et elle est mise en œuvre à l'aide d'un logiciel open-source, gprMax. En outre, dans ce travail, une solution est proposée pour traiter le cas complexe des signaux en champ proche et à large bande-passante en utilisant une combinaison de techniques classiques d'imagerie de migration et d'analyse spectrale à haute résolution. Ce schéma permet également d'estimer la matrice de covariance et de s'assurer que l'on utilise un processus de décorrélation qui est essentiel pour le bon conditionnement de l'analyse.

0.3.1 Compensation des effets de large bande-passante en champ proche

Les données géoradar sont obtenues dans une configuration de champ proche par rapport à la distance de Fraunhofer. Les effets de champ proche font que l'historique de la cible n'est plus une fonction linéaire. D'autre part, dans les configurations à large bande, la réponse de la cible tend à s'étendre sur plusieurs cellules azimutales. La combinaison des effets de champ proche et des effets de large bande entraîne des migrations non linéaires des cellules de portée. Étant donné que les méthodes Specan étudiées utilisent la matrice de covariance de

la cellule azimutale restreinte pour améliorer la résolution de la portée ou encore la cellule de portée restreinte pour améliorer la résolution de l'azimut, alors si l'hypothèse d'ondes planes est prise en compte dans la configuration à large bande du champ proche, la cellule sélectionnée ne fournira qu'une partie des informations sur l'historique de la phase, ce qui entraînera une réduction de la capacité d'estimation des techniques de Specan. Pour compenser les effets du champ proche à large bande, les méthodes de Specan seront appliquées aux images focalisées du géoradar, c'est-à-dire aux résultats focalisés du BP. Ainsi, le vecteur sélectionné contiendra plus d'informations sur l'historique de la phase, ce qui améliorera la capacité d'estimation des méthodes de Specan.

0.3.2 Estimation de la matrice de covariance

Les acquisition obtenues dans le cadre du géoradar présentent une réponse de la cible à partir de différentes positions d'antennes qui sont fortement corrélées en raison de la présence d'un signal à trajets multiples. D'autre part, les méthodes de Specan exigent que les données soient partiellement ou non corrélées afin d'estimer avec succès les paramètres [KV96].

Dans la littérature [Jou+17; KV96; Mar+98] le lissage spatial est utilisé pour décorréler les données. Il s'agit simplement d'une fenêtre glissante dans le domaine spatial à travers une seule direction. Dans ce travail, au lieu de glisser dans le domaine spatial, la fenêtre glissante sera appliquée au sein du domaine des fréquences dans une direction donnée (soit le long de la portée, soit le long de l'azimut) de l'image focalisée du géoradar, d'où le terme de lissage spectral 1D. Le glissement est effectué dans une seule direction, c'est-à-dire le long de la portée pour améliorer la résolution en distance ou le long de l'azimut pour améliorer la résolution de l'azimut. La matrice de covariance des données est ensuite obtenue en faisant la moyenne des matrices de covariance des données obtenues pour chaque fenêtre. Il s'agit d'un cas particulier du lissage spectral 2D, détaillé dans le cas de l'imagerie SAR dans [DeG98; LS96]

Pour la résolution en azimut, la longueur de l'ouverture synthétique disponible est généralement faible, de sorte que la réduction de la longueur totale du réseau à une petite longueur de fenêtre glissante entrave la capacité de résolution de la méthode Specan. C'est pourquoi dans ce travail nous utilisons un lissage spectral

2D [DeG98; LS96] afin d'augmenter le nombre de vues. Le lissage spectral 2D implique un glissement dans le domaine des fréquences dans les deux dimensions, c'est-à-dire le long de l'azimut et de la portée. Plusieurs réalisations de données géoradar décorrélées seront obtenues avec une acquisition réduite soit en azimut, soit en distance. Par conséquent, le choix de la taille de la fenêtre dans une direction donnée dépend de la configuration.

Les résultats suivants sont obtenus à partir des données de simulation obtenues par gprMax. Deux cibles séparées par une distance inférieure à la résolution en azimut et à la résolution en distance sont correctement distinguées en appliquant les techniques de Specan aux données focalisées où les effets de large bande en champ proche sont compensés (Fig. 4).

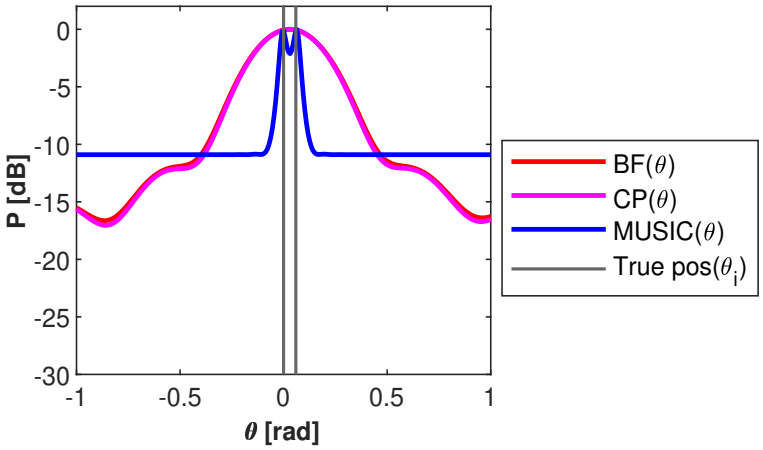

Figure 4: Fonction objective de Specan avec 2 cibles sur le côté du réseau séparées à $dx = 4.75$ cm avec 4 positions d'échantillonnage azimutales..

Nous avons également montré que pour les cibles hétérogènes, les méthodes conventionnelles ont une faible résolution, mais que grâce à la capacité de focalisation à haute résolution des méthodes de Specan, il est possible de séparer deux cibles hétérogènes avec un faible décalage azimutal. En outre, la détection d'une cible dans un environnement avec fouillis de particules ayant des propriétés diélectriques différentes et des tailles différentes est étudiée. Il est possible d'estimer la position azimutale correcte de la cible par les techniques Specan lorsque la cellule de portée correcte est sélectionnée. Enfin, l'imagerie géoradar utilisant les méthodes de Specan est appliquée à un milieu dispersif et à un milieu avec

pertes. Nous avons observé que BP ne pouvait pas séparer deux cibles dont le décalage est inférieur à la résolution en azimut, mais que les méthodes Specan, à l'exception de BP, CP et OPM, pouvaient distinguer les deux cibles présentes dans un environnement dispersif.

0.4 Techniques d'analyse spectrale sur les données de mesure géoradar

Après avoir analysé les performances des algorithmes d'analyse spectrale développés dans ce travail à l'aide de résultats de simulation, ces algorithmes sont appliqués à des scénarios réels issus de données de mesure géoradar.

Tout d'abord, les points forts et les limites des techniques de migration conventionnelles sont illustrés sur différents scénarios en tenant compte de plusieurs nombres de positions d'antennes. Le potentiel des techniques d'analyse spectrale pour surmonter ces limitations est ensuite démontré.

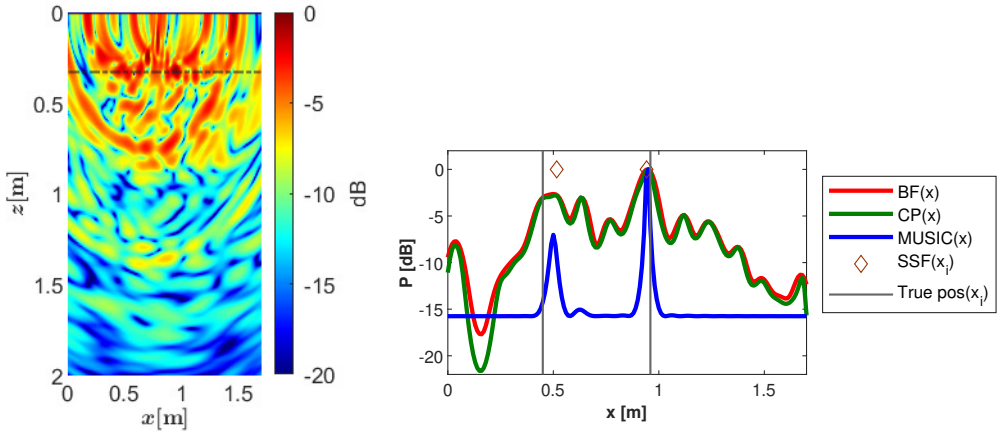

(a) **(b)**

Figure 5: Scénario avec une ouverture synthétique de 0,55 m : (a) résultats BP des données échantillonnées irrégulièrement avec 4 positions d'échantillonnage en azimut, (b) fonction objective Specan pour les données échantillonnées irrégulièrement avec 4 positions d'échantillonnage en azimut.

Deuxièmement, nous avons montré que, pour une ouverture synthétique de taille fixe donnée, lorsque les données sont collectées avec des échantillons d'azimut irréguliers, les performances des techniques de migration classiques se dégradent progressivement (Fig. 5a). Les images focalisées ont une faible résolution et il est donc difficile de séparer les cibles disponibles dans la scène. Pour améliorer

la résolution, des techniques d'analyse spectrale sont utilisées et permettent de distinguer les cibles dans les données échantillonnées en azimut irrégulier, et ce même dans le cas où le nombre de positions d'échantillonnage en azimut est faible (Fig. 5b).

Enfin, nous avons montré que les méthodes Specan peuvent être utilisées pour estimer la position de la cible dans un environnement avec fouillis, à la fois en azimut et en distance.

0.5 Conclusion et perspectives

La résolution de la technique de migration classique est limitée par la largeur de bande du signal et la longueur de l'ouverture synthétique pour les techniques d'imagerie conventionnelles. C'est pourquoi cette recherche s'est concentrée sur l'amélioration de la résolution azimutale en appliquant des techniques d'analyse spectrale 1D. Les techniques Specan étant basées sur des hypothèses d'ondes à bande-passante étroite, une compensation du champ proche à large bande a été effectuée par des méthodes de migration projetées sur une grille polaire. Un cas particulier de lissage spectral 2D a été utilisé, ce qui a permis de distinguer correctement deux cibles séparées par une distance inférieure à la résolution en azimut.

Les algorithmes proposés ont été validés en les appliquant à des scénarios réels, c'est-à-dire à des données de mesure où les méthodes Specan ont montré une capacité de résolution élevée pour distinguer les données avec : un nombre réduit d'antennes, des échantillons d'azimut irréguliers, un environnement avec fouillis et un environnement avec un milieu dispersif.

Une approche alternative comprenant l'implémentation en techniques 2D des techniques 1D déjà mises en oeuvre est proposée. L'algorithme proposé peut également être étendu et appliqué au domaine médical, par exemple pour la détection des vaisseaux sanguins proches. Enfin, les techniques Specan peuvent être appliquées à la détection de cibles enfouies dans un environnement multicouches (couches ayant une permittivité différente).

Chapter 1

Imaging of objects embedded in a dielectric medium

Contents

1.1 Introduction

This chapter presents an overview of remote sensing techniques that are capable of imaging both metallic and non-metallic targets embedded in a dielectric medium.

1.2 Ground Penetrating Radar

GPR emits and receives electromagnetic signals echoed by an underground medium. Electromagnetic waves propagating through the host medium are par-

tially reflected by buried targets, and as shown in Fig. 1.1 the backscattered field is collected by a receiving antenna and undergoes signal processing steps in order to obtain a GPR image [SS10].

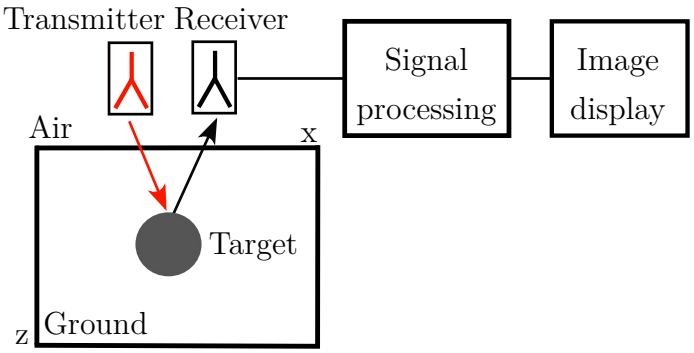

Figure 1.1: GPR measuring principle

1.2.1 Types of GPR waveforms

A GPR may use a pulsed waveform, defined in the temporal domain or continuous waveform specified in the spectral domain.

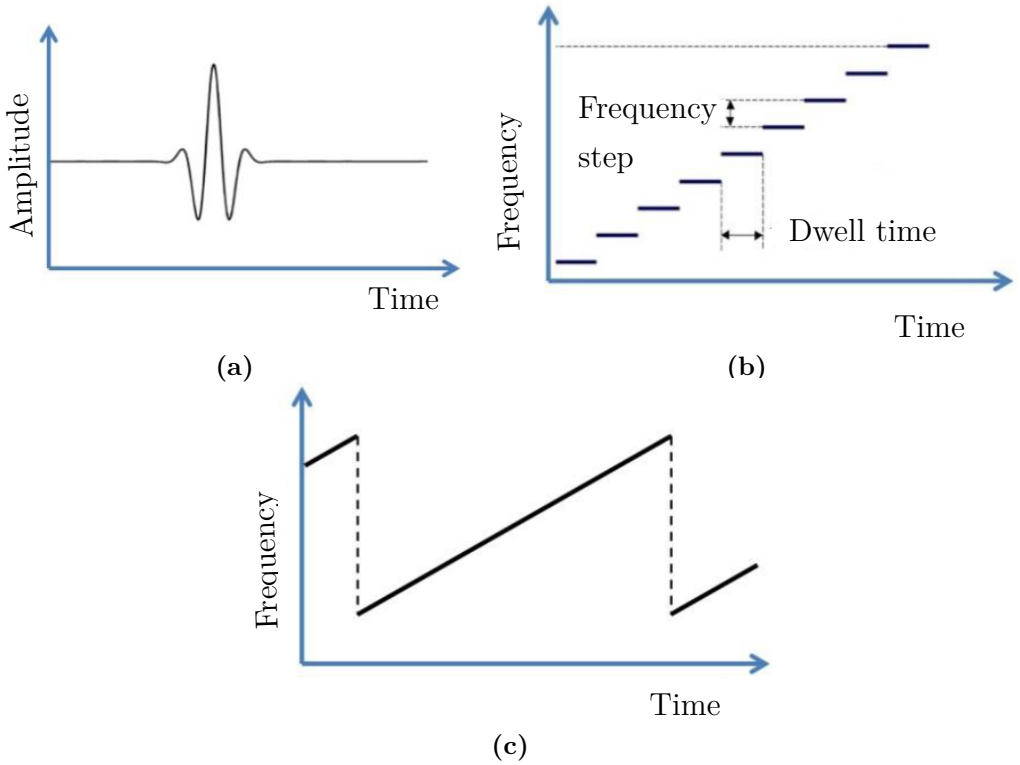

Figure 1.2: GPR waveforms: (a) Pulse, (b) SFCW scan, and (c) FMCW scan [Mar17].

Most GPRs in the commercial market use pulsed signals. They emit a time limited signal and measure the two way distance travelled by the waveform between the radar and the object [Jol08], as illustrated in Fig. 1.2a.

Several types of pulses may be encountered including the Ricker wave, the Gaussian waveform set, i.e., Gaussian and its derivatives [Mar17], Hermite polynomials [HB05] and Gegenbauer waveform [Elb+05].

Continuous Wave (CW) based GPR radars measure the response of the observed scene at different frequency values. In the stepped frequency continuous wave (SFCW) mode, the frequency of monochromatic signal is varied in a discrete way (Fig. 1.2b) whereas in frequency-modulated continuous wave (FMCW) mode (Fig. 1.2c) the transition is continuous and linear in time [Jol08] [Mar17]. An equivalent time limited waveform can be recovered using an inverse Fourier transform.

1.2.2 Classical GPR operating modes

The two dimensional response of target located coordinate (x_0, z_0) is represented in Fig. 1.3

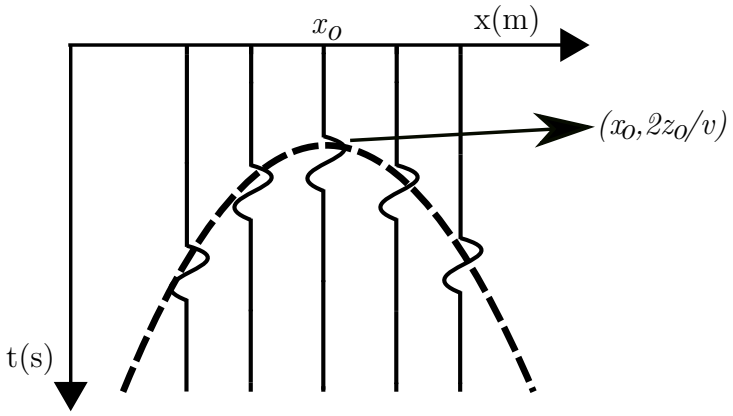

Figure 1.3: Pictorial description of the GPR response of a target

Let x_0 denote the position of Tx/Rx system along scanning line, the two way travel time is given by [SS10]:

$$t = \frac{2\sqrt{(x - x_0)^2 + z_0^2}}{v} \tag{1.1}$$

Where v is the velocity of the electromagnetic field in the soil. Therefore, the recorded data is represented as a hyperbola with an apex at $(x_0, 2z_0/v)$ as illustrated in Fig. 1.3. Due to this signal migration, imaging methods are required to focus the GPR image in order to estimate the true locations and size of the targets as detailed in section 1.4.

The usual GPR data acquisition modes are A-scan, B-scan, and C-scan as illustrated in Fig. 1.4. An A-scan is a is single radar trace along the depth axis. A B-scan is a two dimensional data set formed by a set of A-scans acquired from different positions along the scanning axis. In B-scan GPR images, the response of an isolated scatterer shows up as a hyperbola and finally a series of B-scan measurements form a C-scan which may be used for 3D imaging purposes.

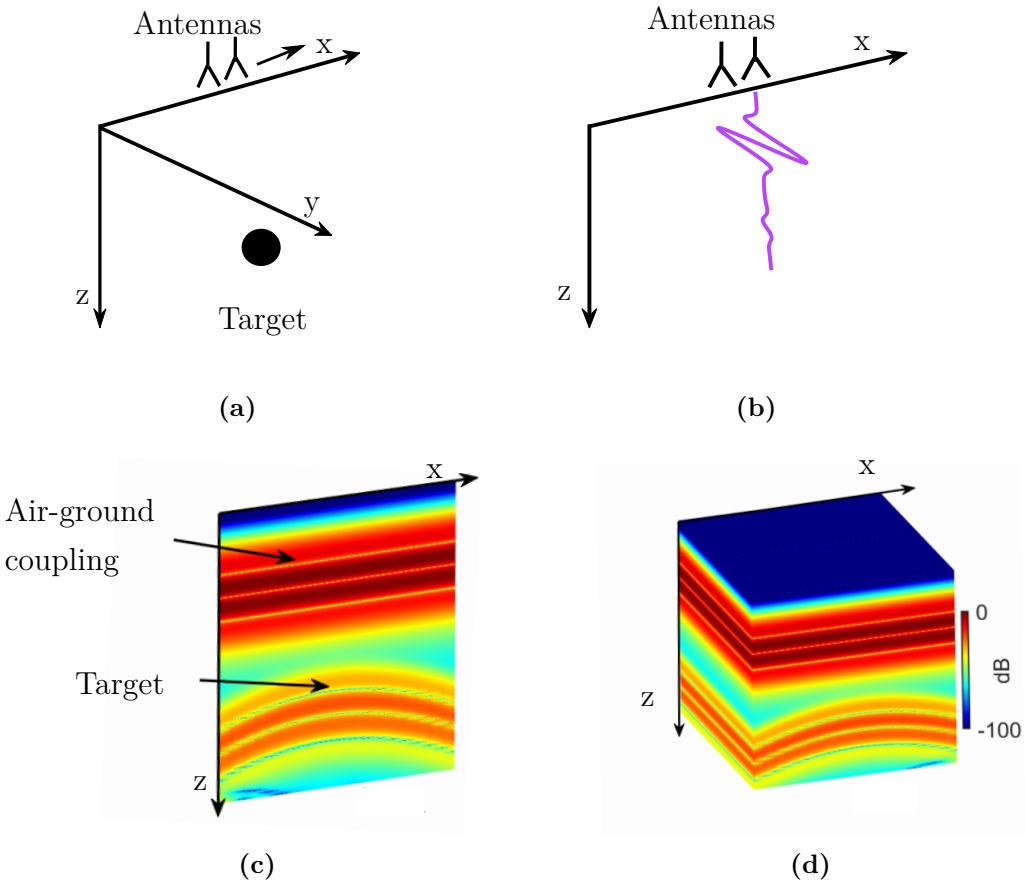

Figure 1.4: GPR operating modes: (a) Geometrical configuration, (b) A-scan, (c) B-scan, and (d) C-scan.

1.2.3 Multiple Antenna Configurations for GPR

Several antenna configurations illustrated in Fig. 1.5 may be used to perform GPR imaging. The most typical linear array configuration is single-input single-output SISO, where several pairs of translated transmitters and receivers work independently and collect the data sequentially at different time instances [HE00].

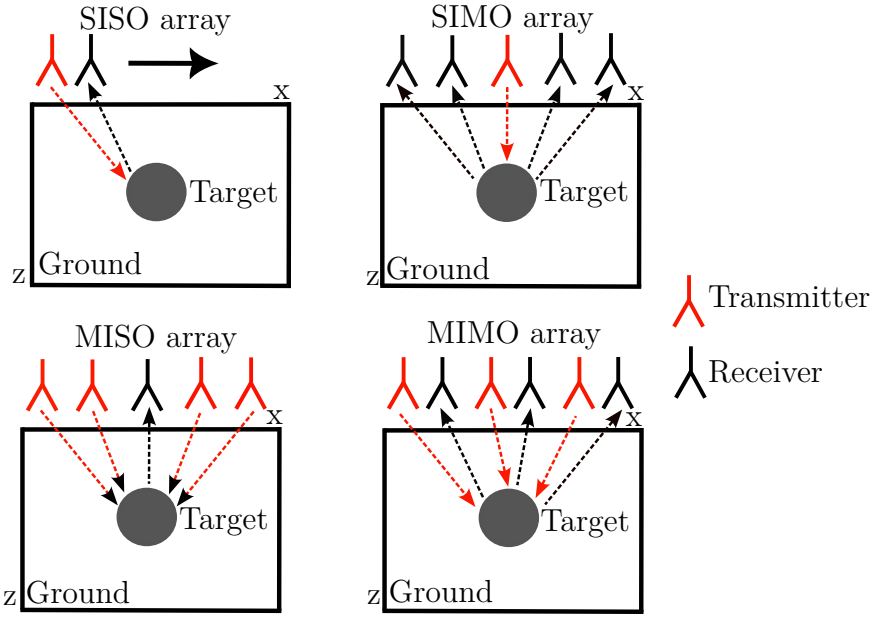

Figure 1.5: Multi-antenna GPR setup configurations

Another configuration is single-input multi-outputs SIMO. This configuration employs one transmitter and an array of receivers. SIMO configuration can sample signals along a profile with a smaller acquisition time. In [Yar+07], SIMO configuration was tested for landmine detection application.

An inverted version of such configuration is multi-inputs single-output MISO, which consists of several transmitters and one receiver. Although MISO configuration is not common in GPR sensing, they have been used for some radar and seismic imaging systems [Mar17].

Recently, a more flexible configurations namely MIMO have been studied. MIMO configuration can be used to artificially extend or populate a virtual array.

In this work SISO configuration is used since we aim to reduce hardware complexity.

1.2.4 Applications of GPR

There are many applications of GPR, to mention few, within the field of archaeology [Per14] [Con13], GPR can allow to identify areas with alleged interesting buried remains, and to avoid an exhaustive and expensive (sometimes too expensive) excavation. Another application of interest is the field of preventive archaeology that is, the preventive prospecting of areas where something is going to be built (a road, a building, an underground station, etc.). This mitigates the risk of destroying archaeological sites and also mitigates the economic risk that the works will be stopped by some Cultural Heritage Institution

Monitoring of monuments as historical buildings, statues [Per14] [Sam+11], ancient fountains, historical bridges, ... [Per14] [Sol+11] is another subject of interest. In particular, GPR monitoring (possibly integrated with other geophysical investigations) can be used to evaluate the state of preservation of the monuments and can provide useful information in order to address a restoration project properly. In some cases, information of historical interest can also be extracted for example, about the presence of walled rooms, crypts, hypogeum rooms, tombs, hidden frescoes, and so on [Per14] [Pie+06], [Gra+11].

GPR prospecting is also exploited in civil engineering [Per14] [GGB00]. In particular, it can be used to identify structural damages and to investigate hidden structures like sewers or water and gas pipes, whose presence is in many cases not precisely documented

Demining is another important application. In particular, modern mines are customarily built with plastic materials with only little or even no metallic parts. Therefore, they are often hardly visible or completely invisible to a metal detector. Moreover, a metal detector is not able to provide all the details possibly available from a GPR system, namely the position (in particular the depth), the size, and (among certain limits) the shape of the buried target. Demining has been dealt with for years within the GPR community [Per14] [GY02], and it has also been successfully performed many times [Per14], [ST09].

Last but not least, let also mention the subject of the GPR investigation on Mars, where unmanned vehicles are gathering data, mainly looking for water and, consequently, the possible (current or past) presence of life [Per14].

1.3 Propagation Modelling

1.3.1 Overview

Modelling of electromagnetic scattering by a buried object has a wide interest in the field of GPR [Dan04]. The analytical and numerical modelling of GPR scenarios can improve understanding of complex interactions occurring between electromagnetic field radiated by a antenna and buried target. The obtained simulated data may be used to test new algorithms and data processing techniques.

The main elements to consider during modelling include the target, source field radiated by antenna and background medium as illustrated in Fig. 1.6.

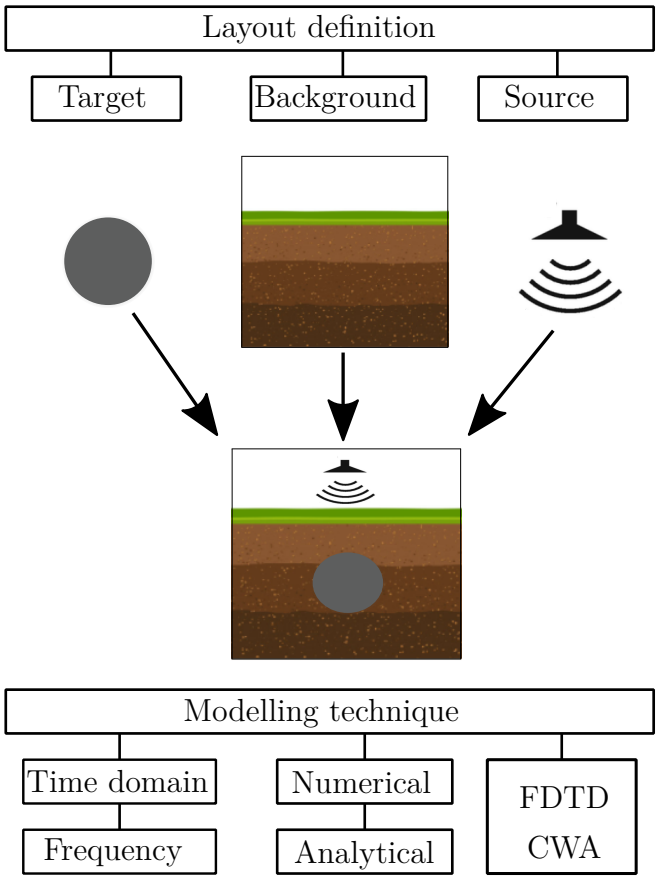

Figure 1.6: Propagation modelling of GPR scenarios

Incorporation of all key features is necessary to make the modelled scenario as close to reality as possible. The choice of a modelling technique can be made on the basis of time versus frequency analysis, or on the other hand numerical methods (model general scenario) versus analytical ones (approximate problem using canonical geometries) [BP15].

1.3.2 Finite-Difference Time-Domain method

Time-domain techniques are well suited to GPR applications dealing with the scattering of a pulsed signal [Taf95]. FDTD is a well established numerical approach which uses vector components of electromagnetic fields that represent differential and integral forms of Maxwell equations [Taf95]. The electric field can be evaluated at any point in space and any time from the knowledge of the magnetic field in four neighbouring points and vice versa. As a general purpose electromagnetic simulation technique, FDTD handles dielectric materials as well as highly complex scenarios. The main limitations of FDTD concerns its instability [Taf95]. In this work, FDTD modelling is employed through the gprMax software [War21], an open source software that simulates electromagnetic wave propagation.

1.3.3 Exploding source model

Most of the migration methods are based on the concept of exploding source model (ESM) [Cla85]. Two way distances are replaced by one way distance with a wave propagation at a half way velocity [Özd+14].

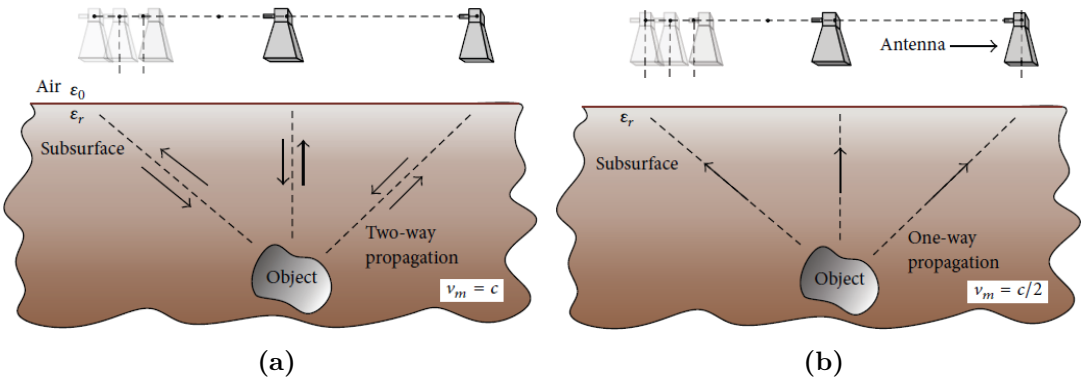

Figure 1.7: Geometry for (a) B-scan GPR data collection scheme and (b) utilising "exploding source model." [Özd+14]

1.4 Migration Techniques

1.4.1 Overview

Ground Penetrating Radar (GPR) is a non-destructive imaging system able to provide high-resolution images of the subsurface. From a theoretical point of view, it requires to solve an inverse scattering problem, where a set of parameters describing the underground scenario must be retrieved starting from samples of the measured electromagnetic field [BP15].

In a typical space-time B-scan GPR image, any scatterer within the image region shows up as a hyperbola as previously discussed in section 1.2.2. The aim of migration techniques is to focus the recorded echoes back into the true position of their corresponding scattering centres. Among the existing range of migrations techniques one may cite Hyperbolic (Diffraction) summation (HS) migration, Phase Shift migration (PSM), Frequency-wavenumber (F-k) migration and Back Projection (BP) algorithm. A good overview of these techniques is given in [Özd+14].

1.4.2 Hyperbolic (Diffraction) Summation

In Hyperbolic summation (HS), each point in migrated image is result of a summation of the recorded amplitudes along a diffraction hyperbola, whose curvature is governed by the medium velocity and the depth of the point to be migrated. The true location of the object is at the apex of hyperbola [Özd+14]. If there is an object in the apex of the diffraction hyperbola, the amplitudes will add, If not,the summation of the non-coherent data along the diffraction hyperbola tends to zero [Sch01].

To derive HS [Sch01] let the 3D data $d(x, y, t)$ is recorded with monostatic GPR by moving an antenna on the ground in the xy-plane. Measurement taken are $d(x_j, y_k, t)$ at position (x_j, y_k, t), with $j = 1, 2, ..., J$ and $k = 1, 2, ..., K$. Migrated image $\widehat{D}$ is calculated as:

$$\widehat{D}(x, y, z) = \sum_{i=1}^{k} \sum_{j=1}^{l} d(x_j, y_k, \frac{2R_{j,k}}{v}) \tag{1.2}$$

where: $R_{j,k}$ is the distance between measuring position $(x_j, y_k, 0)$ and the point

(x, y, z) that is to be migrated. v is the propagation velocity of the medium. The time $(\frac{2R_{j,k}}{v})$ represents the total travelling time from the transmitting antenna to the point (x, y, z) and back.

In GPR data, using the antennas off-ground, the two-way travelling time has to be modified to take into account the different velocities of the two media (air and ground) and the diffraction on the air-ground interface [Sch01].

1.4.3 Phase-shift

Phase shift migration (PSM) was introduced by Gadzag [Gaz78] and utilise ESM. Derivation of PSM [Zha+13], starts with electromagnetic scalar wave equation. Let $d(x, z, t)$ be the electromagnetic field.

$$[\frac{\partial^2}{\partial x^2} + \frac{\partial^2}{\partial z^2} - \frac{1}{v_m^2}\frac{\partial^2}{\partial t^2}]d(x, z, t) = 0 \tag{1.3}$$

Where v_m is the propagation velocity of the medium, t is time, x is radar moving direction and z is the radar range dimension. The first step is to apply a FT on the measured data over x and t. The second step is to calculate electromagnetic field at a new range location $z_1 = z_0 + \Delta z$.

$$d(k_x, z_1, \omega) = d(k_x, z_0 = 0, \omega)exp(j\sqrt{\frac{4\omega^2}{v_m^2} - k_x^2} \triangle z) \tag{1.4}$$

In the equation above:

$$\triangle z = v_m \triangle t \tag{1.5}$$

Lastly, by using an IFT along k_x and ω direction and choose "$t = 0$", focused data $\widehat{D}(x, z = z_1, t = 0)$ are obtained as:

$$\widehat{D}(x, z = z_1, t = 0) = \frac{1}{2\pi}\int d(x, z = z_1, \omega)e^{w\times(t=0)}d\omega \tag{1.6}$$

In conclusion we can say, PSM is a recursive algorithm that iteratively puts a phase shift to migrate wave field to exploding time of $t = 0$, such that all scattered waves are drawn back to a focused image.

1.4.4 Frequency-Wavenumber (Stolt) migration

F-k (Stolt) migration was introduced by Gazdag and Stolt in 1978 [Sto78] [Gaz78] and also uses ESM. The measured signal can be written as summation of an infinite number of plane waves as:

$$d(x,y,z=0,t)=\left(\frac{1}{2\pi}\right)^{3/2}\iiint_{\infty}^{\infty}D(k_x,k_y,\omega)\times e^{-j(k_xx+k_yy-\omega t)}dk_xdk_yd\omega \quad (1.7)$$

Setting "$t=0$" in equation 1.7 and using $D(k_x,k_y,\omega)=e^{jk_zz}D(k_x,k_y,\omega,z=0)$ we get:

$$d(x,y,z=0,t)=(\frac{1}{2\pi})^{3/2}\iiint_{\infty}^{\infty}D(k_x,k_y,\omega)\times e^{-j(k_xx+k_yy+k_zz)}dk_xdk_yd\omega \quad (1.8)$$

However, the data in (k_x,k_y,ω) domain should be transformed to (k_x,k_y,k_z) to be able to use the FT. The relationship between ω and k_z and $d\omega$ and dk_z can be obtained from spatial wave-number and frequency relation as:

$$k_x^2+k_y^2+k_z^2=\frac{\omega^2}{v_m^2},\quad \omega=v_m(k_x^2+k_y^2+k_z^2)^{1/2},\quad d\omega=\frac{v_m^2k_z}{\omega}dk_z \quad (1.9)$$

Substituting these equations into (1.8), the following is obtained:

$$\begin{aligned}\widehat{D}(x,y,z) &= d(x,y,z,t=0) \quad (1.10)\\ &= (\frac{1}{2\pi})^{3/2}\iiint_{\infty}^{\infty}\frac{v_m^2k_z}{\omega}D^m(k_x,k_y,k_z)\times e^{-j(k_xx+k_yy+k_zz)}dk_xdk_ydk_z\end{aligned}$$

The above image represent a focused image where, $D^m(k_x,k_y,k_z)$ is the mapped version of the original data $D(k_x,k_y,\omega)$. After this mapping, new data set does not lie on the uniform grid due to non-linear feature of the transformation [Sto78]. So interpolation should be done to permit the use of an FFT for fast processing of data.

1.4.5 Back Projection focusing

Back-projection (BP) [Sou99] is a focusing technique which is a dual of F-k technique but operate in time domain. Compare to F-k, it takes a longer time

but it is best more agile as it can be used for any acquisition geometry. Whereas the formal techniques requires to have a linearly spaced rectilinear acquisition.

Considering the case where the position of transmitter and receiver is at (x_t, y_t, z_t) and (x_a, y_a, z_a) respectively with receiving synthetic aperture array length L_{syn} such that $x_a \in [-L_{syn}/2 \quad L_{syn}/2]$. N_s point scatterers are identified with their Cartesian coordinates x_i, y_i, z_i. The index i is for the ith point scatterer P_i. The equivalent distance from the radar to the i-th point scatterer is given by [Jou+17]:

$$\begin{aligned} d_i(x_a) &= (dTx_i + dRx_i)/2 \\ &= (\sqrt{(x_t - x_i)^2 + (y_t - y_i)^2 + (z_t - z_i)^2} + \sqrt{(x_a - x_i)^2 + (y_a - y_i)^2 + (z_a - z_i)^2})/2 \end{aligned} \tag{1.11}$$

In spatial domain, the range focused received signals by the radar may be expressed as:

$$s(x_a, d) = \sum_{i=1}^{N_s} s_i h(d - d_i(x_a)) e^{-j\phi_x(x_a)} \tag{1.12}$$

where by; s_i represents the received signal which include all the attenuations that occur during the round trip propagation and the reflectivity of the i-th point-like target, $h(d)$ is the range ambiguity function in the spatial domain, and $\phi_x(x_a) = k_c d_i(x_a)$ is the phase variation along the aperture while k_c is the round-trip carrier wavenumber given as $k_c = 4\pi f_c/c$.

The focusing is performed as follows: for one particular range cell BP takes the received signal from a given position along the aperture x_a and back-projects it over a spherical arc corresponding to all the possible contributing image pixels. Once the back-projection is performed on the remainder received signals from other ranges and other positions along the aperture, then accumulated, the focused GPR image $\widehat{D}(x_i, y_i, z_i = z_0)$ is obtained, where by z_0 is a constant. One particular pixel p_i of the focused GPR image spanning the Cartesian grid is constructed as [Jou+17]:

$$\widehat{D}(x_i, y_i, z_i = z_0) = \int_{x_a=-Lsyn/2}^{Lsyn/2} s(x_a, d_i(x_a)) e^{jk_c d_i(x_a)} dx_a \tag{1.13}$$

1.4.6 Resolution

Resolution indicates the limit of certainty in determining the position and the geometrical attributes of a target (such as the size, shape, and thickness) [Jol08]. Ground penetrating radar resolution consists of two components, namely the longitudinal (range or depth) resolution length and the lateral (azimuth or angular or sideways displacement) resolution length.

1.4.6.1 Range Resolution

Range resolution (δ_{range}) is defined as the minimum distance by which two targets of equal strength can be discriminated. This discrimination may be achieved through the transmitted signal frequency diversity. In GPR depth resolution is related to the bandwidth B of the system and to propagation the velocity in the medium v by [Per14]:

$$\delta_{range} = \frac{v}{2B}, \quad v = c/\sqrt{\varepsilon_r} \tag{1.14}$$

where by ε_r is the medium permittivity and c is the propagation speed in free space .

1.4.6.2 Azimuth Resolution

Azimuth resolution ($\delta_{azimuth}$) is the resolution along scanning direction, and it depends on the length of antenna array L_{syn} and the effective wavelength lambda λ_{eff} that takes into account the medium permittivity as illustrated in Fig. 1.8.

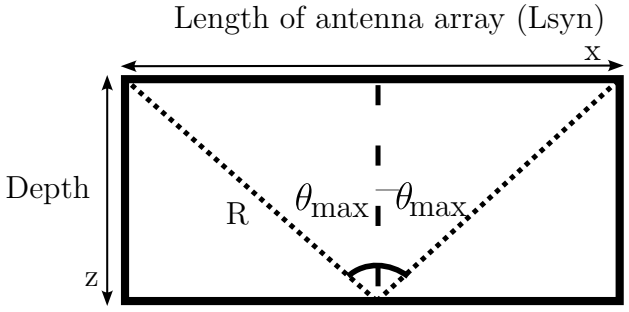

Figure 1.8: Illustration of the azimuth scan for scatterer located at central azimuth position.

Azimuth resolution is given as[Per14]:

$$\delta_{azimuth} = \frac{\lambda_{eff}}{2\sin(\theta_{max})}, \quad \lambda_{eff} = v/f_c, \quad \sin(\theta_{max}) = L_{syn}/2\sqrt{(L_{syn}/2)^2 + z^2} \tag{1.15}$$

where by R is the distance antenna-target, f_c is the central frequency and z is the depth.

1.4.7 Example of Migration in GPR application

In this section, the studied migration techniques are implemented and the obtained results will be compared and analysed.

1.4.7.1 Problem statement and acquisition configuration

GPR data were simulated by using FDTD tool [War21] using isotropic antennas uniformly distributed along the x-axis with a spacing of $\lambda_{eff}/4$, with permittivity $\varepsilon_r = 5$.

The medium is assumed to be homogeneous, non-magnetic and lossless. A Ricker waveform with a centre frequency of 0.5 GHz and a bandwidth of 2 GHz was used. Targets are perfect electric conductor spheres with 2 mm radius and are located around the coordinates x_0, z_0 with an array of N_a elements

The Fourier resolution based on our configuration is given in Table 1.1.

Table 1.1: Fourier resolution values at $z = 0.8$ m

Azimuth resolution (δ_x)	18 cm
Range resolution (δ_z)	3.35 cm

The following configuration cases were considered:

- Case 1 : Range resolution analysis scenarios given in Table 1.2 with their respective setup configurations in Fig. 1.9a
- Case 2 : Azimuth resolution analysis scenarios given in Table 1.3and their corresponding setup configurations in Fig. 1.9b

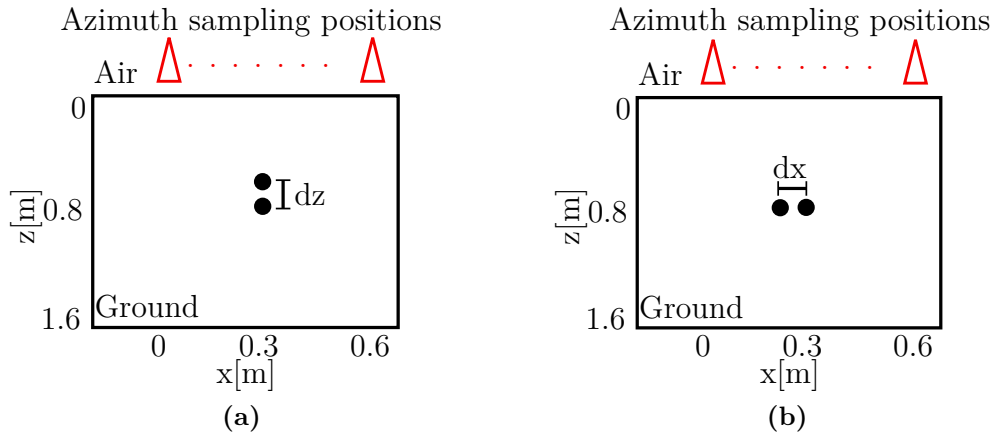

Figure 1.9: Setup configuration for scenario with 2 targets at the centre of array and 20 azimuth sampling positions.

Table 1.2: GPR scenario for range resolution analysis

Scenario	Target position	N_a	Position on array
1 (2 targets)	$x_0 = 0.3$ m, $z_0 = 0.8$ m, $dz = 20$ cm	20	Centre
2 (2 targets)	$x_0 = 0.3$ m, $z_0 = 0.8$ m, $dz = 2$ cm	20	Centre

Table 1.3: GPR scenario for azimuth resolution analysis

Scenario	Target position	N_a	Position on array
3 (2 targets)	$x_0 = 0.3$ m $z_0 = 0.8$ m $dx = 20$ cm	20	Centre
4 (2 targets)	$x_0 = 0.3$ m, $z_0 = 0.8$ m, $dx = 4.75$ cm	20	Centre

Scenario 1 considers two targets at the same azimuth position, located at the centre of the array with a range spacing $dz = 20\ cm$ which is larger than δ_z, ($\delta_z = 3.35\ cm$). Scenario 2 reduces this offset distance to $dz = 2\ cm$ that is smaller than δ_z. Scenario 3 and 4 represent similar approach in azimuth direction.

1.4.7.2 Classical Imaging results

The images in Fig. 1.10 clearly show the presence of hyperbolas. When the spacing is sufficient (i.e higher than range resolution) we can observe the hyperbolas with different shapes, whereas when the spacing is smaller than range resolution we can not discriminate the hyperbolas.

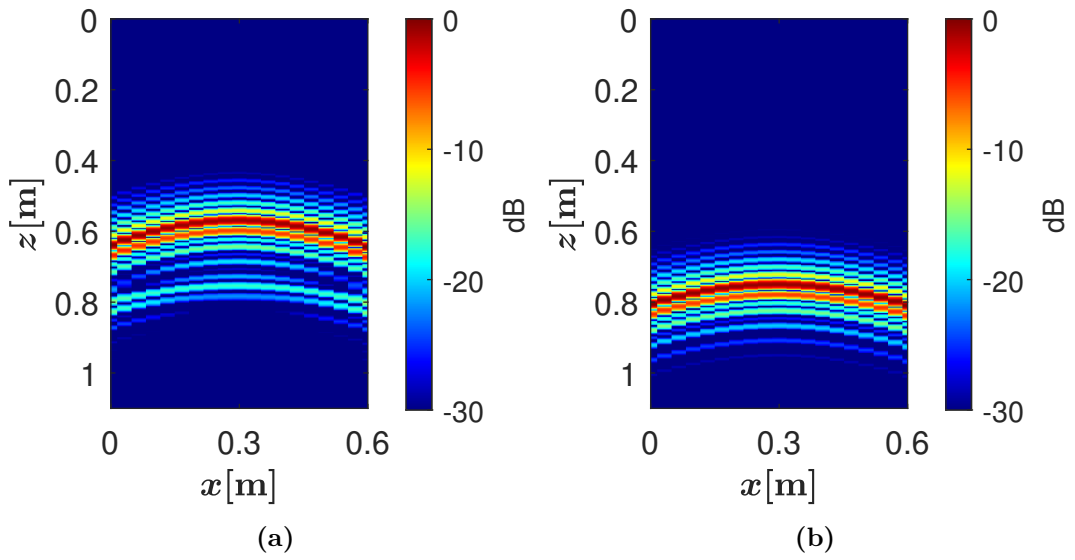

Figure 1.10: Range focused GPR image for: (a) Scenario 1 with $dz = 20\ cm$ and (b) Scenario 2 with $dz = 2\ cm$.

So, Migration techniques were applied to GPR range focused data and the results are given in Fig. 1.11 and Fig. 1.12.

To begin with scenario 1, results show that all migration techniques were able to locate the two target at their true position (Table 1.2) as shown in Fig. 1.11 when the offset is larger than δ_z ($dz = 20\ cm$).

HS is simple and therefore it is very easy to implement. But its focusing ability is not good compared to other algorithms. PSM is much faster than HS as it use advantage of FFT. Its performance in terms of computation time, focusing, and image quality is MODEST when compared to the rest of algorithms.

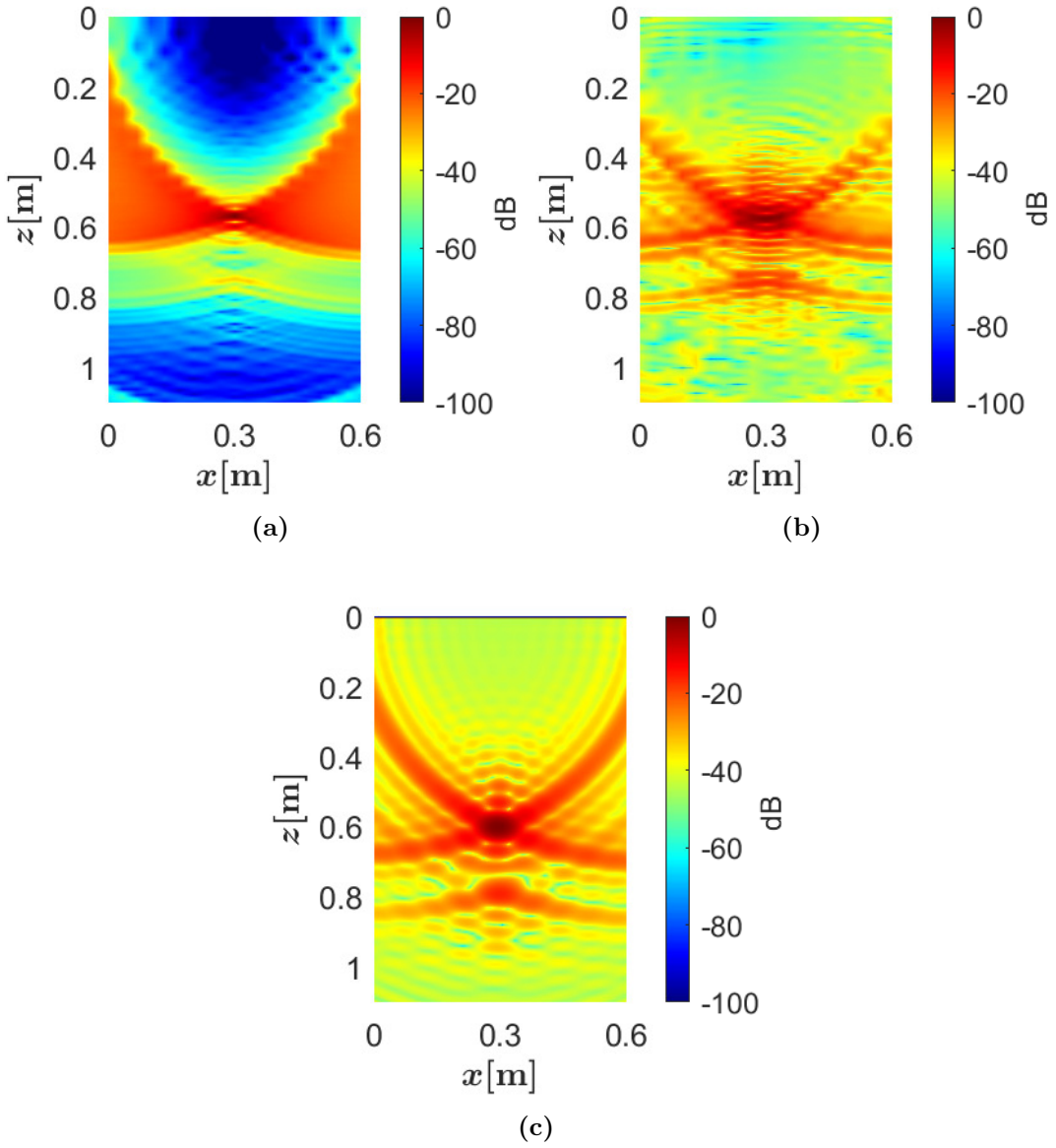

Figure 1.11: Migration focused results for $dz = 20\ cm$ (scenario 1): (a) Hyperbolic Summation, (b) Phase-shift migration, (c) Back-projection focusing or F-k migration

F-k and BP migration are said in literature to be equivalently the same method. The image quality of BP migration is the best compared to all other algorithm. BP is not simple as HS or other algorithm as implementation of algorithm is more complex.

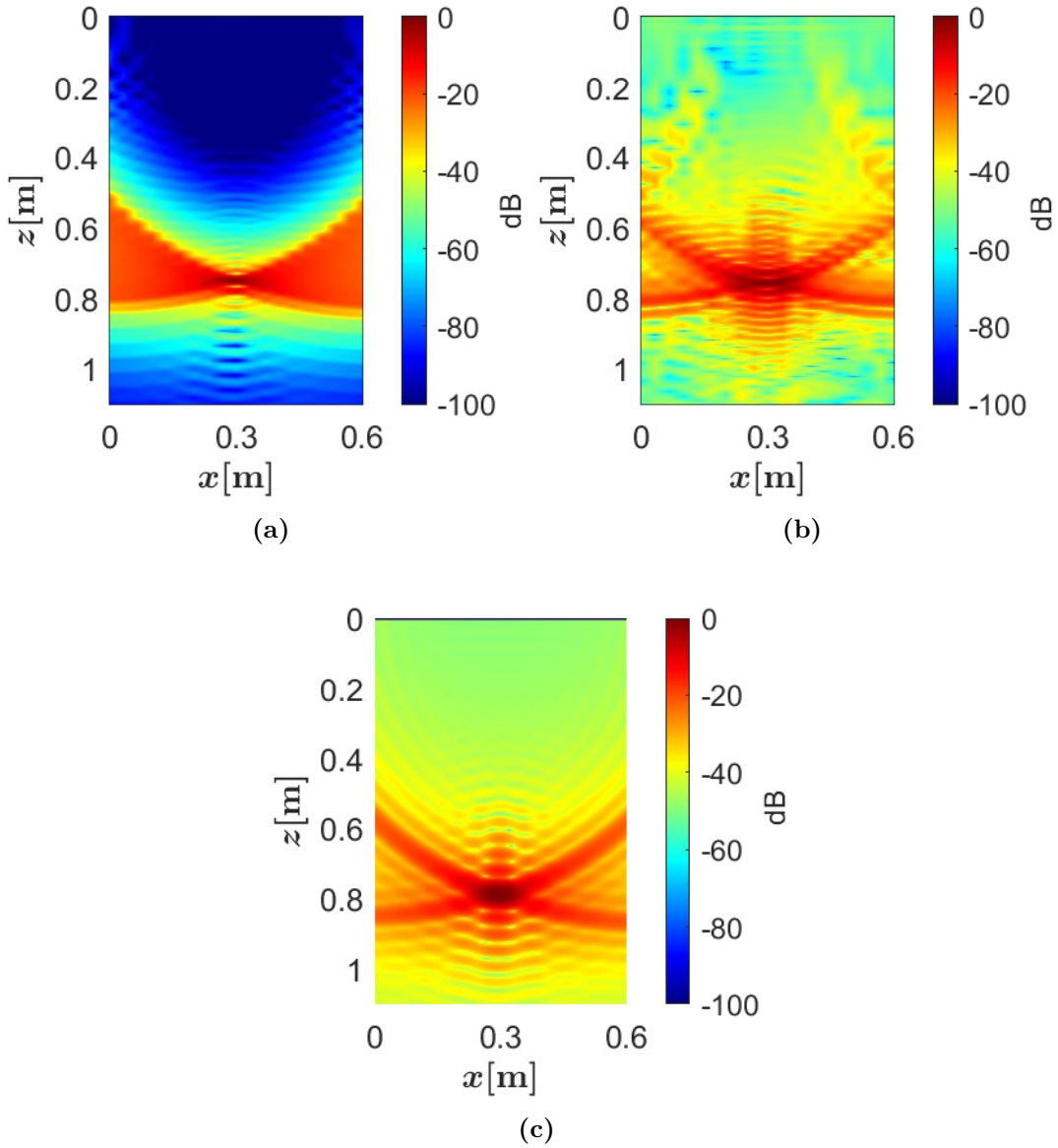

Figure 1.12: Migration focused results for $dz = 2\ cm$ (scenario 2): (a) Hyperbolic Summation, (b) Phase-shift migration, (c)Back-projection focusing or F-k migration

On the other hand, when the offset is reduced to a distance less than δ_z i.e $dz = 2\ cm$ (scenario 2), all the migration techniques fail completely to distinguish the two targets as indicated in Fig. 1.12 but instead the two targets were interpreted as a single target.

Similar to range resolution scenarios, in azimuth resolution scenarios we observe BP was able to distinguish two targets separated by offset larger than δ_x ($dx = 20$

cm) in Fig. 1.13a (scenario 3). When the offset was reduced to offset which was less than azimuth resolution ($dx = 4.75\ cm$), BP interpreted two targets as single targets as presented in Fig. 1.13b (scenario 4).

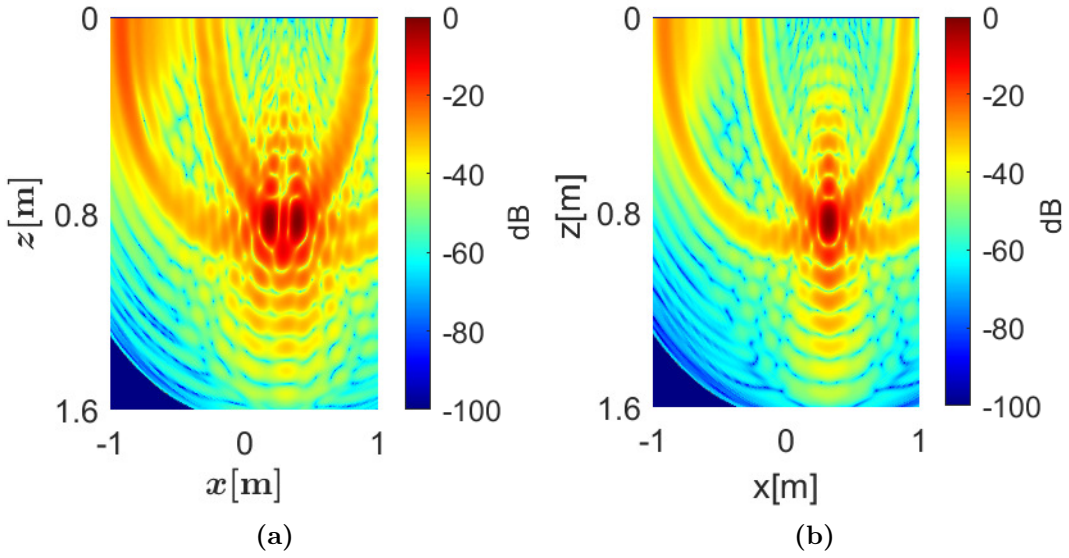

Figure 1.13: BP focused results for: (a) Scenario 3 with $dx = 20\ cm$ and (b) Scenario 4 with $dx = 4.75\ cm$.

The following conclusion may be drawn from the above BP focusing results for both azimuth and range scenarios:

- BP focusing algorithm was able to distinguish targets separated with offset that was larger than range resolution or azimuth resolution
- When the offset is reduced i.e inferior to range or azimuth resolution, BP focusing algorithm failed to distinguish targets and instead showed them as single target. This is because, resolution performance of classical GPR method is limited by signal bandwidth and the size of synthetic aperture (number of antenna elements).

In order to overcome resolution limitation of conventional GPR focusing methods, the literature proposes several solutions which include:

- MIMO configurations
- Spectral analysis techniques

The next sections explores the main principles of the mentioned solutions and discusses their pros and cons.

1.5 MIMO Configurations

Multiple-Input Multiple-Output (MIMO) based radar systems has been widely employed in civilian and military applications, as they can synthesize larger virtual arrays which increase resolution and the number of targets that can be detected [Góm14].

1.5.1 Types of MIMO configurations

There are several configuration of MIMO radar depending on the location of the transmitting and receiving elements.

1.5.1.1 Statistical MIMO radar

As shown in Fig. 1.14 the transmit and receive array elements are broadly spaced, providing independent scattering responses for each antenna pairing. The diversity provided by the multiplicity in transmit and receive angles can be exploited to improve the detection performance [Góm14].

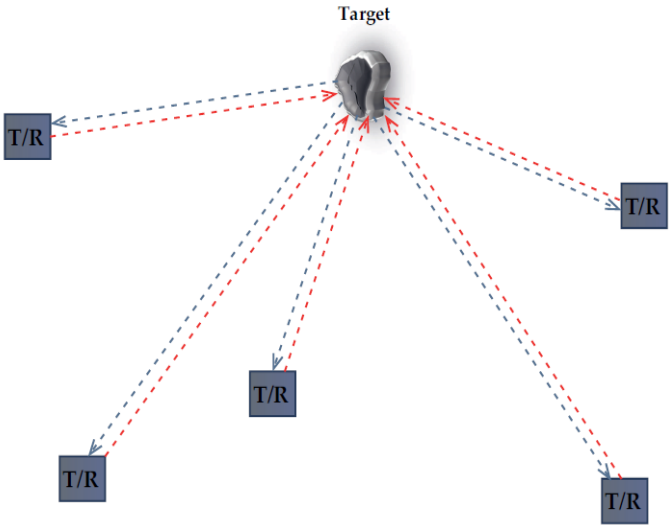

Figure 1.14: Statistical MIMO radar configuration [Góm14]

1.5.1.2 Coherent MIMO radar

In coherent MIMO radar, the transmit array elements and receive array elements are closely spaced. Further classification may be done into monostatic

MIMO radar if transmit and receive arrays are closely spaced (Fig. 1.15a) and bistatic MIMO radar (Fig. 1.15b) if transmitter array is widely separated from receiver array [Góm14]. In a coherent MIMO configuration, it is assumed that the target's scattering response is identical or strongly correlated for each antenna pair, up to some small delay [Cat15].

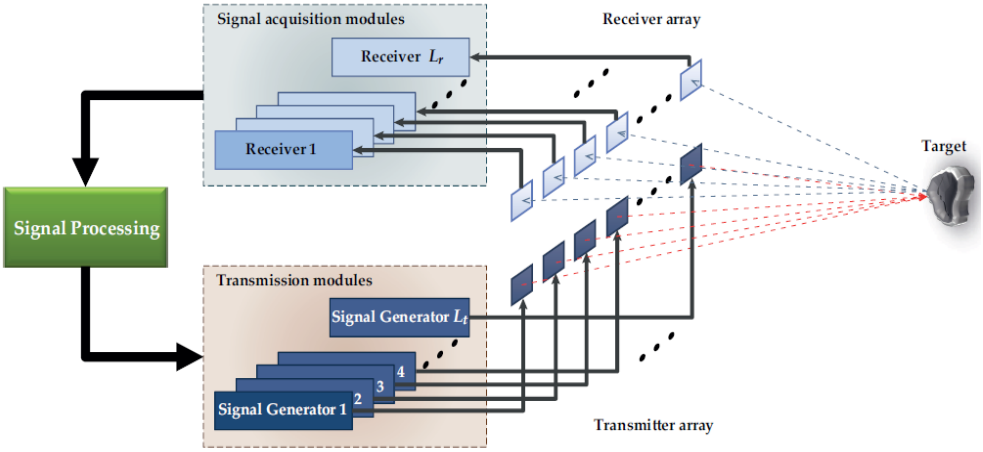

(a) Monostatic MIMO radar [Góm14]

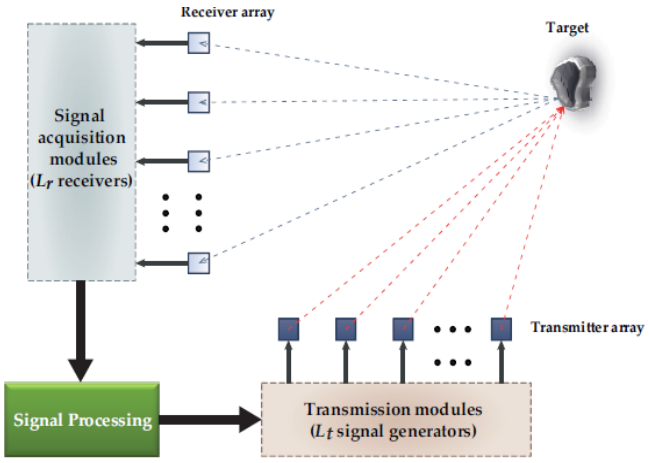

(b) Bistatic MIMO radar [Góm14]

Figure 1.15: Coherent MIMO radar configurations.

1.5.2 Virtual arrays, resolution and sampling

The performance of the MIMO systems can be characterised by a virtual array constructed by the convolution of the locations of the transmit and receive

antenna locations. One of the major objectives of such sampling strategies is to generate additional measurements and increase the data spectral diversity. In principle, with the same number of antenna elements, this virtual array can be much larger than the array of an equivalent traditional system. Thus, with comparison with the equivalent physical array, the MIMO system will have much better intrinsic spatial resolution at a small cost [Cat15].

Main applications of virtual array are found in resolution and sampling purposes. Among the various virtual array configurations, one may identify two widely used structures:

- **Augmented arrays:** The resulting virtual array is wider than the original one, leading to an improved resolution.
- **Populated arrays:** In this case, very often array elements have dimensions that are greater than the required spacing for unambiguous sampling (ex. $\lambda/2$).

Compared to SAR-like sampling (M-SISO), MIMO configurations provide:

- A gain of acquisition time and infrastructure deployment (scan).
- An increased hardware complexity. MIMO systems simultaneously augment an array populated and provide a substantial gain of acquisition time [Har+20].

1.5.3 MIMO GPR

1.5.3.1 Overview

Ground penetrating radar (GPR) cannot be yet considered a reliable and practical method for the following reasons:

- First, to improve the resolution for classical GPR, a large bandwidth is used and it often requires high frequencies. Due to loss media, higher frequencies experience higher attenuation, and the increased frequency bandwidth affects the signal-to-clutter ratio (SCR) and intensifies dispersion effects. [Zen+15].
- Second, systems using lower frequencies [Cui+01], [Le +08] require an electrically small wideband antenna. However, the system may not provide

adequate resolution to determine the geometry of the targets.

- Third, due to the influence of the antenna radiation direction and target radar cross sections (**RCSs!**), the detection accuracy is seriously limited in a complex environment [Fis+06], [BT06].
- Finally, the interpretation of the raw data is affected by the operator's expertise, and a priori information is necessary to obtain reliable results [Dan04].

New method is needed to improve the detection capability of a GPR system or data processing methods since the target properties and the detection environment can not be changed. Expanding the signal bandwidth and increasing the transmitting power for a narrow signal pulse bandwidth seems like the right way in theory. However, it has a high requirement for the electron device, and the hardware system cost is high. Improving the detection mode and the data processing method may be one way to overcome the aforementioned shortcomings[Zen+15].

1.5.3.2 Multiple Antenna GPR

GPR system with a (MIMO) array antenna is an effective approach of space-time configuration in wireless network and communication that shows great potential for application in radar, sonar, speech recognition, seismic exploration, etc.

In recent research on GPR, a more flexible array which is well-known as multi-input multi-output (MIMO) or multi-static configuration was proposed [Sat+14; Cou+07; JLZ12; Pag+14]. In this configuration, the array comprises several transmitters and receivers that work together.

Some works in narrow-band radar system [HBC07; LS07; ZY11] show that MIMO can improve the number of target that can be identified, allow direct applicability of adaptive technique, and improve the flexibility of transmit beam-pattern design.

Other research in imaging radar [ZY11; ZY10] show that MIMO configuration can reduce the number of transmitters and receivers while maintaining the same

performance to synthetic aperture array. In [Cou+07] and [JLZ12], an array that consists of 2 transmitters and several receivers was proposed for GPR system and it was shown that such configuration can reduce the clutter and improve target detection performance. Another work in [Sat+14] allows all transmitters and receivers to work together in collecting data on archaeological site and demonstrates that this configuration can improve the imaging capability.

1.5.4 Discussion and conclusion on MIMO GPR

These results indicate that MIMO configuration has some advantages compared to the conventional sensor configuration. However, some issues must be considered before practically apply MIMO configuration [Mar17]. Firstly, MIMO configuration yields higher complexity in hardware and measurement process. Although the complexity can be reduced by utilising smaller number of transmitters or receivers, the imaging performance will also degrade. Thus, it is necessary to obtain analytical formulation of MIMO array performance in order to control the trade-off between array complexity and imaging performance. Secondly, the signal processing algorithms must be modified to deal with such configuration.

1.6 Spectral Analysis Techniques

This section introduce the Spectral analysis techniques (Specan) which are known for their high resolution estimation capabilities. The studied (Specan) techniques in this work are covariance matrix based algorithms.

1.6.1 Signal source model

Signal model of $\boldsymbol{y}$ in plane wave approximation may be considered as sum of M exponentials:

$$\boldsymbol{y} = \sum_{m=1}^{M} \boldsymbol{a}(\omega_m) s_m \tag{1.16}$$

By taking noise into consideration, signal source mode in equation (1.16) can be written in vector form as:

$$\boldsymbol{y} = \boldsymbol{A}\boldsymbol{s} + \boldsymbol{n} \tag{1.17}$$

Where by $\boldsymbol{y}$ is data column vector given as $\boldsymbol{y} = \begin{bmatrix} y_1 & y_2 & \cdots & y_L \end{bmatrix}^T$. Where $l = 1, ..., L$ is a antenna index and M is the number of sources. Then $\boldsymbol{s}$ is the

signal column vector generated by the sources: $\boldsymbol{s} = \begin{bmatrix} s_1 & s_2 & \cdots & s_M \end{bmatrix}^T$. And $\boldsymbol{n}$ is a zero-mean spatially uncorrelated additive noises with spatial covariance matrix equal to $\sigma^2 I_L$: $\boldsymbol{n} = \begin{bmatrix} n_1 & n_2 & \cdots & n_L \end{bmatrix}^T$

$\boldsymbol{A}$ is a steering matrix whose columns are functions of unknown spatial frequencies ω_m . The array steering column vector $\boldsymbol{a}(\boldsymbol{\omega}_m)$ is defined as:

$$\boldsymbol{a}(\boldsymbol{\omega}_m) = \begin{bmatrix} 1 & e^{-j\omega_m} & e^{-j2\omega_m} & \cdots & e^{-j(L-1)\omega_m} \end{bmatrix}^T \tag{1.18}$$

Therefore, matrix $\mathbf{A}$ with $L \times M$ dimension is given as:

$$\begin{aligned} \boldsymbol{A} &= \begin{bmatrix} \boldsymbol{a}(\boldsymbol{\omega}_1) & \boldsymbol{a}(\boldsymbol{\omega}_2) & \cdots & \boldsymbol{a}(\boldsymbol{\omega}_M) \end{bmatrix} \\ &= \begin{bmatrix} 1 & 1 & \cdots & 1 \\ e^{-j\omega_1} & e^{-j\omega_2} & \cdots & e^{-j\omega_K} \\ e^{-j2\omega_1} & e^{-j2\omega_2} & \cdots & e^{-j2\omega_K} \\ \cdots & \cdots & \cdots & \cdots \\ e^{-j(N-1)\omega_1} & e^{-j(N-1)\omega_2} & \cdots & e^{-j(N-1)\omega_K} \end{bmatrix} \end{aligned} \tag{1.19}$$

Where ω_m is the normalised frequency of M sources in radian/sample. The objective is to estimate all the ω_m. This general model can be given as the expressions of the signals corresponding to range focusing (a sampled frequency ramp) and azimuth focusing (with an array).

Limitation of signal model to GPR data

1. The signal model assume the amplitude $\boldsymbol{a}(\omega_m)$ is constant for all frequencies. In GPR this is not true because the response vary on different frequencies.

2. Response of the model can be expressed as sum of M contributions. In range focusing it implies if there are M targets then will have M response. This is a simplification of the model which is not verified in reality in presence of clutter. Clutter mitigation will be discussed in Chapter 2 on section 2.8.

3. The signal model assume the plane wave (far field) assumptions while our

GPR data are acquired in near field (region that is close to an antenna based on Fraunhofer distance).

Therefore it is necessary to adapt GPR data in order to use the Specan techniques which are derived based on this data model. This will be further discussed in Chapter 2.

1.6.2 Covariance matrix

The data covariance matrix $\boldsymbol{R}$ may be computed as follows, where $\mathbb{E}\{\}$ denote statistical expectation:

$$\begin{aligned} \boldsymbol{R} &= \mathbb{E}\{\boldsymbol{y}\boldsymbol{y}^H\} \\ &= \mathbb{E}\{(\boldsymbol{A}\boldsymbol{s}+\boldsymbol{n})\,(\boldsymbol{A}\boldsymbol{s}+\boldsymbol{n})^H\} \\ &= \mathbb{E}\{(\boldsymbol{A}\boldsymbol{s}+\boldsymbol{n})\,(\boldsymbol{A}^H\boldsymbol{s}^H+\boldsymbol{n}^H)\} \\ &= \boldsymbol{A}\mathbb{E}\{\boldsymbol{s}\boldsymbol{s}^H\}\boldsymbol{A}^H\} + \boldsymbol{A}\mathbb{E}\{\boldsymbol{s}\boldsymbol{n}^H\} + \boldsymbol{A}\mathbb{E}\{\boldsymbol{n}\boldsymbol{s}^H\} + \mathbb{E}\{\boldsymbol{n}\boldsymbol{n}^H\} \end{aligned} \tag{1.20}$$

Assumptions:
i) Noise and signals are uncorrelated:

$$\mathbb{E}\{(\boldsymbol{s}\boldsymbol{n}^{\boldsymbol{H}}\} = 0 \tag{1.21}$$

ii) Noise are having a common variance σ^2 at all sensors and uncorrelated among all sensors:

$$\mathbb{E}\{\boldsymbol{n}\boldsymbol{n}^{\boldsymbol{H}}\} = \sigma^2\boldsymbol{I} \tag{1.22}$$

Therefore equation (1.20) becomes:

$$\boldsymbol{R} = \boldsymbol{A}\boldsymbol{R}_{\boldsymbol{ss}}\boldsymbol{A}^H + \sigma^2\boldsymbol{I}_{\boldsymbol{L}} \tag{1.23}$$

where: $\boldsymbol{R}_{\boldsymbol{ss}} = E\{\boldsymbol{s}\boldsymbol{s}^H\}$ is the signal covariance matrix and σ^2 is the common covariance of the noises.

In order to estimate the covariance matrix in the most convenient situation, independent realisations are preferred as they bring the maximum information. On the contrary, when data are correlated (which is the case with GPR data due

to presence of multipath signals) only less information can be obtained. Therefore, for GPR implementations the following question may be taken into account: How to adequately estimate covariance matrix ? the response to this question will be detailed in chapter 2.

1.6.3 Eigenvalue decomposition

It is a tool used to decompose the range space of the data covariance matrix into two complimentary subspaces [KV96]. The $L \times L$ data covariance matrix may be written as $\mathbf{R}$

$$\begin{aligned} \mathbf{R} &= \mathbf{A}\mathbf{R}_{\mathbf{ss}}\mathbf{A}^H + \sigma^2\mathbf{I}_L \\ &= \mathbf{U}\mathbf{\Lambda}\mathbf{U}^H \\ &= \mathbf{U}\widetilde{\mathbf{\Lambda}}\mathbf{U}^H + \sigma^2\mathbf{U}\mathbf{U}^H = \mathbf{U}(\widetilde{\mathbf{\Lambda}} + \sigma^2)\mathbf{U}^H \end{aligned} \tag{1.24}$$

where $\boldsymbol{R_{ss}}$ is $L \times L$ covariance matrix of the source signals, $\widetilde{\mathbf{\Lambda}}$ is a diagonal matrix containing the eigenvalues of $\boldsymbol{R_{ss}}$, ordered in following manner:

$$\widetilde{\lambda_1} \geq \widetilde{\lambda}_2 \geq \cdots \widetilde{\lambda}_L > \widetilde{\lambda}_{M+1} = \ldots = \widetilde{\lambda}_M = 0 \tag{1.25}$$

where the source covariance matrix rank, M, indicates the number of separable signals. The first M elements of the eigenvector matrix $\mathbf{U}$ span **signal subspace**, and the remaining $L - M$ ones correspond to the so-called **noise subspace**.

Equation (1.24) can be written as:

$$\boldsymbol{R} = \boldsymbol{u} \left[\begin{array}{cccc|c} \widetilde{\lambda}_1 + \sigma^2 = \lambda_1 & & & & 0 \\ & \widetilde{\lambda}_2 + \sigma^2 = \lambda_2 & & & \\ & & \ddots & & \\ & & & \widetilde{\lambda}_M + \sigma^2 = \lambda_M & \\ \hline & & & & \sigma^2 \\ & & & & \ddots \\ 0 & & & & \sigma^2 \end{array}\right] \boldsymbol{u}^H \tag{1.26}$$

where the eigenvalues of $\mathbf{R}$ verify

$$\lambda_1 \geq \lambda_2 \geq \lambda_3 \geq \ldots \geq \lambda_M > \sigma^2 = \sigma^2 = \ldots = \sigma^2 \tag{1.27}$$

1.6.4 Estimation of number of signals

Total number of eigenvalues are known since there are L eigenvalues. From equation (1.26), the multiplicity of smallest eigenvalues K can be determined. and estimate of number of signals M can be obtained from relation:

$$M = L - K \tag{1.28}$$

This can be done by plotting L versus eigenvalues, where by a shift will be observed as eigenvalues move from signal subspace to noise subspace. Illustration has been done in figure (1.16) where by $\boldsymbol{R}$ is $L \times L$ matrix with $L = 10$, number of estimated source signals is M=2.

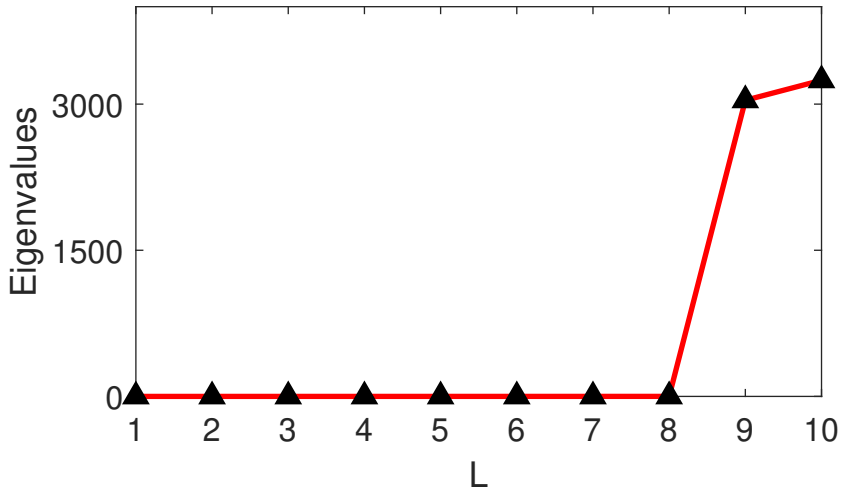

Figure 1.16: L versus eigenvalues plot to estimate the number of signal M

Therefore, number of source signal M can be estimated. This estimation is possible only if $M < L$.

1.6.5 Spectral Analysis Techniques

The Specan methods studied are algorithms based on the covariance matrix data $\boldsymbol{R}$ as listed in Tab. 1.4 and detailed in Appendix A.

Table 1.4: List of acronyms of Specan methods

Acronym	**Specan method**
BF	Beamforming [SM+05] [CGY10] [KV96]
CP	Capon beamforming method [SM+05] [CGY10] [KV96]
MUSIC	MUltiple SIgnal Classification [SM+05] [KV96] [WKL14]
OPM	Orthogonal Projector Method [Sun+19] [Mar+98]
MUroot	Root-MUSIC [SM+05] [KV96] [WKL14]
OPMroot	Root-OPM [Mar+98]
ESPRIT	Estimation of Signal Parameters via Rotational Invariant Techniques [SM+05] [KV96] [WKL14]
DML	Deterministic Maximum Likelihood [SM+05] [KV96]
SSF	Signal Subspace Fitting [SM+05] [KV96]

The Specan methods may be categorised based on how they manipulate the covariance matrix to estimate the parameters as:

- Peak-search approaches
- Root methods approaches
- Multidimensional approaches

1.6.5.1 Peak search methods

These methods estimate parameter as coordinates of local maxima of continuous objective function. In this category we have Beamforming, Capon's method, MUSIC and Orthogonal Projector method (OPM).

1.6.5.2 Roots methods

These methods do not involve an exhaustive search through all possible steering vectors to estimate parameter positions. Instead they perform estimation by

finding the roots of a polynomial of the objective function, thus they provide direct parameter estimation. This reduces the computation load and storage requirements in large extent compared to Peak-search approaches. Example of Root methods include Root-MUSIC, Root-OPM and ESPRIT method.

1.6.5.3 Multi-dimensional methods

These methods perform estimation of parameters through the optimisation of concentrated criterion. They have improved accuracy of estimated parameters with exchange of heavy computational cost. Studied techniques in this group include Deterministic Maximum Likelihood (DML) and Signal Subspace Fitting (SSF).

1.6.6 How Spectral methods may be used in GPR ?

Spectral analysis methods have been widely used in aerial classical radar to resolve closely spaced scatterers [HF20]. In GPR, Specan methods have been used mostly in in Civil engineering to improve GPR time resolution and the detection of healthy and damaged zones [Le 07]. In Civil engineering, the main data processing difficulty lies in the detection of close backscattered echoes due to the limited time resolution [Sun+19]. In practical environments, the backscattered echoes come from the signal emitted by the transmitter, though usually along different paths. Therefore, these backscattered echoes are highly correlated or even coherent. Consequently, there will be a rank loss of the data covariance matrix. Signal processing methods, such as high-resolution approaches based on the data covariance matrix, suffer greatly from performance degradation due to a mix of signal and noise subspaces [Sun+19]. To handle the correlated echoes, the data covariance matrix should be processed with a decorrelation technique, such as Spatial smoothing, which allows the obtaining of a new covariance matrix with a restored rank [Le 07].

The existing works in literature have focused on improving the range resolution of GPR data. But in most GPR applications, range resolution is better compared to azimuth resolution. So this research will focus on implementation of Specan techniques to improve the azimuth resolution.

The following are the main challenge of implementing Specan on GPR data on

azimuth direction:

- GPR data are acquired in near field wide band width. Near field wide band effects causes the data to behave in a non-linear manner i.e result to hyperbola shape. Therefore, as the Specan studied use a restricted range cell or azimuth cell, the use of Specan methods directly on GPR data may lead to decrease of discrimination ability [Jou+17]. So adaptation of GPR data obtained in near field wide bandwidth is required in order to improve resolution ability of Specan methods. This will be discussed in detail in Chapter 2.
- Moreover, Specan methods requires that the data are non or partially decorrelated. In State of the art 1D spectral smoothing has been proposed. But this technique reduces resolution from full array to sub array. In this research, we have proposed a method that can reserve the full length of the array and this will be discussed in detail in Chapter 2.

1.7 Conclusion

Specan methods will be applied in this work to improve resolution since they are signal processing techniques that may be used to improve the existing hardware. While MIMO configuration may be able to improve resolution, hardware resources are required including adaptation of signal processing methods to be able to process the data acquired with MIMO configuration. But the use of Specan techniques with non-planar i.e near field wide bandwidth waves configuration requires a significant adaptation of GPR data. Therefore the next chapter will discuss the adaptation done to GPR and analyse the results obtained after implementation of Specan methods on GPR data.

1.8 Contribution of this thesis

This thesis aimed to propose co-located multi-antenna solutions and their corresponding signal processing methods. The main contribution made by this thesis involves implementation of high resolution focusing methods i.e Spectral analysis (Specan) techniques to GPR data along azimuth direction. To do this successfully, significant adaptation had to be made to GPR data in order to take advantage of high resolution capacity of Specan methods. In consequence, the following results

were achieved in this work:

- Improvement of location accuracy and data acquisition speed by using multi-antenna system i.e N-SISO configuration.
- Overcoming resolution limit of conventional migration methods which depend on bandwidth and available size of synthetic aperture.
- Reduced system complexity of GPR systems by reducing the number of azimuth sampling positions required while maintaining high resolution and accuracy estimation of targets.
- Reduced the bandwidth required during GPR object detection while maintaining high resolution and estimation accuracy of targets.
- Imaging of the target in a heterogeneous medium i.e cluttered medium environment as well as imaging of heterogeneous targets.

Chapter 2

High Resolution 2D GPR Imaging using Spectral Analysis Techniques

Contents

2.1 Introduction

This chapter discusses the main contribution of this thesis which is to overcome the resolution limitation of classical GPR imaging techniques. These improvements are based on the use of spectral analysis techniques with GPR data acquired in near field and wide bandwidth configurations. Such specific processing requires significant adjustments.

Propagation modelling of GPR scenarios is introduced in order to understand the complex interaction between electromagnetic waves and targets. The section details why FDTD modelling method is opted for in this work and how it is implemented using the free software gprMax.

Furthermore, in this work a solution is implemented in order to handle near field and wide bandwidth signals using a pre-processing step based on classical imaging prior to the application of high resolution spectral analysis techniques. A specific scheme is adopted to adequately estimate the data covariance matrix.

Different scenarios including a homogeneous host medium, complex targets, dispersive and lossy host media are simulated and studied. The performance of different processing configuration are evaluated and compared.

2.2 Propagation modelling

2.2.1 FDTD modelling using gprMax

GprMax [War21] is an open source software that simulates electromagnetic wave propagation by solving Maxwell's equations in 3D using a Finite-Difference Time-Domain FDTD method.

GprMax involves advanced modelling features such as multilayer simulations, an unsplit implementation of higher order Perfectly Matched Layers (PMLs) using a recursive integration approach, diagonally anisotropic materials and dispersive media using multi-pole Debye, Drude or Lorenz expressions, soil modelling using a semi-empirical formulation for dielectric properties and fractals for geometric characteristics, rough surface generation and the ability to embed complex transducers and targets.

2.2.2 Quantitative comparison of gprMax with a CEA Grenoble hybrid model

GprMax simulations are compared with those derived from a hybrid tool developed at CEA Grenoble which has been created for simulating a communication channels for GPR applications based on polarimetry radar [Mot06].

2.2.2.1 CEA hybrid model

This model characterises the backscattered response of the target when illuminated by an electromagnetic wave and takes into account the effects of polarisation, the electromagnetic characteristics of the ground as well as couplings taking place between the antennas and the ground. The validation of the model with measurements and full-wave simulations (i.e. through the CST MWS® tool) was done at CEA Grenoble

When polarisation effects are included in the radar equation, the transfer function is expressed as follows:

$$H_s(f,n,m) = \frac{-j\lambda_g}{\sqrt{4\pi}} \frac{e^{-jk(R_{Tx}+R_{Rx})}}{4\pi R_{Tx} R_{Rx}} \begin{bmatrix} H_{Tx}^x(f,\theta_{AoD},\phi_{AoD}) \\ H_{Tx}^y(f,\theta_{AoD},\phi_{AoD}) \\ H_{Tx}^z(f,\theta_{AoD},\phi_{AoD}) \end{bmatrix}^T \begin{bmatrix} S_s^{xx} & S_s^{yx} & S_s^{zx} \\ S^{xy} & S_s^{yy} & S_s^{zy} \\ S_s^{xz} & S_s^{yz} & S_s^{zz} \end{bmatrix} \begin{bmatrix} H_{Rx}^x(f,\theta_{AoA},\phi_{AoA}) \\ H_{Rx}^y(f,\theta_{AoA},\phi_{AoA}) \\ H_{Rx}^z(f,\theta_{AoA},\phi_{AoA}) \end{bmatrix} \tag{2.1}$$

Where λ_g is the wavelength in the propagation medium, k is the wavenumber, R_Tx and R_Rx are the relative distances between transmitter n (Tx), receiver m (Rx) and the target respectively. H_{Tx}^x, H_{Tx}^y, H_{Tx}^z, H_{Rx}^x, H_{Rx}^y, H_{Rx}^z are the transfer functions of the antennas in the x, y and z axis directions (Fig. 2.1). They depend on the transmit frequency f, the departure angles θ_{AoD},ϕ_{AoD} and arrival angles θ_{AoA},ϕ_{AoA}, in elevation and azimuth, respectively.

The backscattering matrix, $\boldsymbol{S_s}$ can be noted as follows:

$$\boldsymbol{S_s}(\phi_i,\theta_i,\phi_s,\theta_s,f) = \begin{bmatrix} S_s^{xx} & S_s^{yx} & S_s^{zx} \\ S^{xy} & S_s^{yy} & S_s^{zy} \\ S_s^{xz} & S_s^{yz} & S_s^{zz} \end{bmatrix} \tag{2.2}$$

Where $\phi_i,\theta_i,\phi_s,\theta_s$ represent the incidence and backscatter angles in azimuth and elevation, respectively. Each element of the scattering matrix, $|S_{\xi\zeta}|^2 = \sigma_{\xi\zeta}$,

represents the radar cross-ection (RCS) for the incident wave of polarisation $\boldsymbol{\zeta}$ and the backscattered wave of polarisation $\boldsymbol{\xi}$.

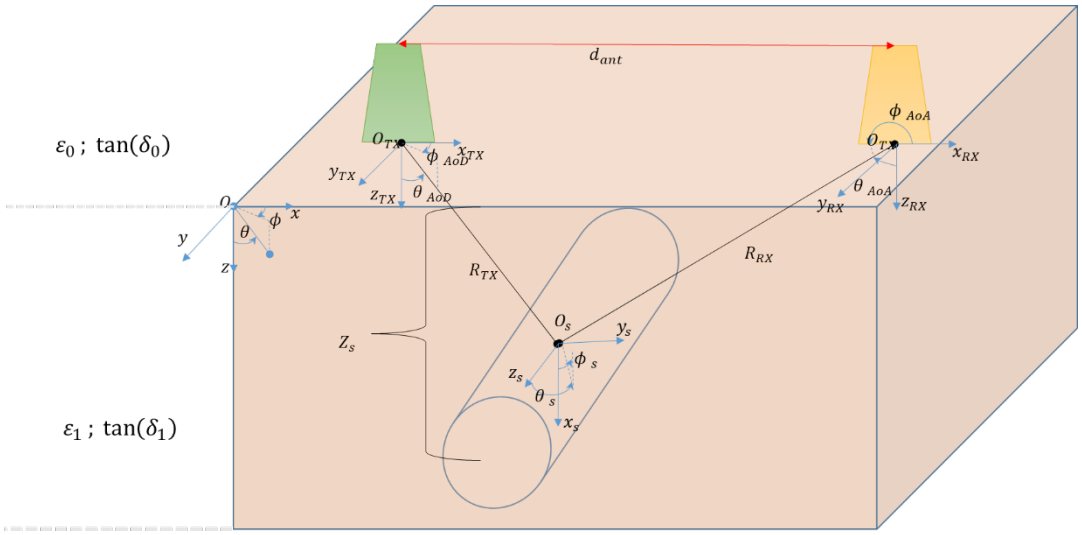

Figure 2.1: Geometrical configuration of a bistatic GPR measurement for homogeneous soil

The wave number is calculated as follows:

$$k = \omega\sqrt{\mu\varepsilon} = k_0\sqrt{\mu_r\varepsilon_r} = \beta - j\alpha, \quad \text{where} \quad k_0 = \omega\sqrt{\mu_0\varepsilon_0} \tag{2.3}$$

Where μ_0, ε_0 are the permeability and permittivity in vacuum, respectively and μ_r, ε_r represent the relative permeability and permittivity of propagation medium, respectively. Subsequently, the attenuation constant α, is calculated according to the following equation:

$$\alpha = \omega\sqrt{\frac{\mu\varepsilon'}{2}\left(\sqrt{1+\tan^2\delta}-1\right)}^{1/2} \tag{2.4}$$

And the phase constant β is determined as follows:

$$\beta = \omega\sqrt{\frac{\mu\varepsilon'}{2}\left(\sqrt{1-\tan^2\delta}-1\right)}^{1/2} \tag{2.5}$$

Where ε' and δ represent the dielectric constant and loss tangent of the propagation medium, respectively.

The antenna patterns were simulated using the CST MWS® tool in order to

account for potential coupling terms and simulation results are then integrated into the analytical formulation.

A fundamental point in the calculation of the channel transfer function is the determination of the target backscatter matrix. The backscatter matrix is calculated theoretically from the RCS using existing canonical formulations or by full-wave simulation.

Moreover, the canonical models are given considering an electric field polarisation parallel or perpendicular to the cylinder axis (Fig. 2.2). However, in most cases, the cylinder axis will not be parallel or perpendicular to the electric fields of the antennas and the full-wave simulation of all possible scenarios (incidence angle and backscatter angle) requires a considerable computational time.

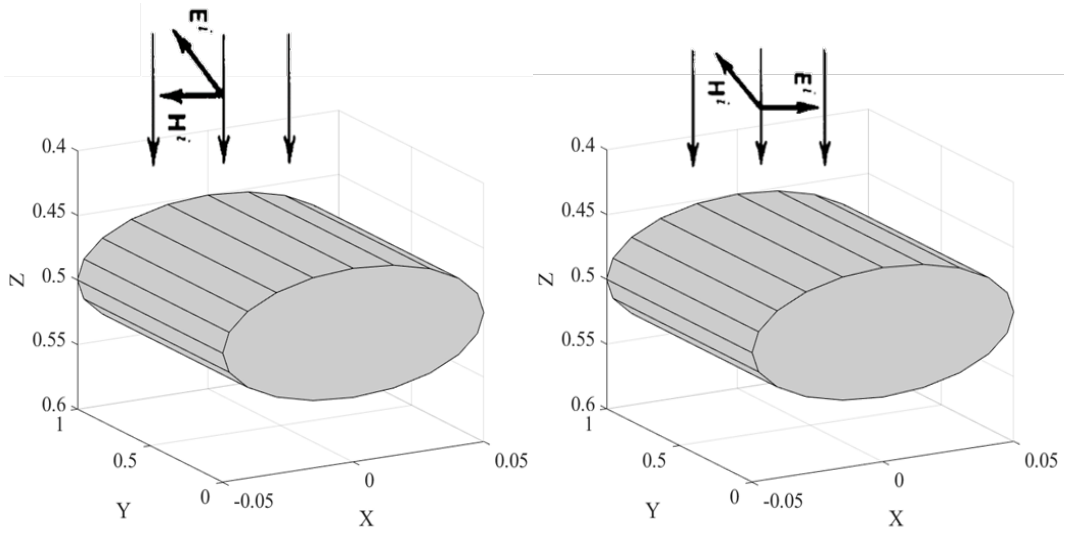

Figure 2.2: Definition of polarisation (a) Linear polarisation parallel (fields oriented along y) and (b) Perpendicular (fields oriented along x) to the cylinder axis polarisation.

In order to take into account the orientation of the pipe (Fig. 2.3) the RCS of the cylinder is first calculated in its reference frame (Fig. 2.1) for both polarisations using an existing canonical formulation for infinite length cylinders or from full-wave simulation.

The path of the channel seen by the antenna, named the effective length of the cylinder $L_{eff,p}(f)$ is calculated from the knowledge of the target position and the

lobe width (red line in Fig. 2.4) by projection. This effective length is used as an input for the calculation of canonical RCS, or as a normalisation element for a RCS obtained from the full-wave simulation.

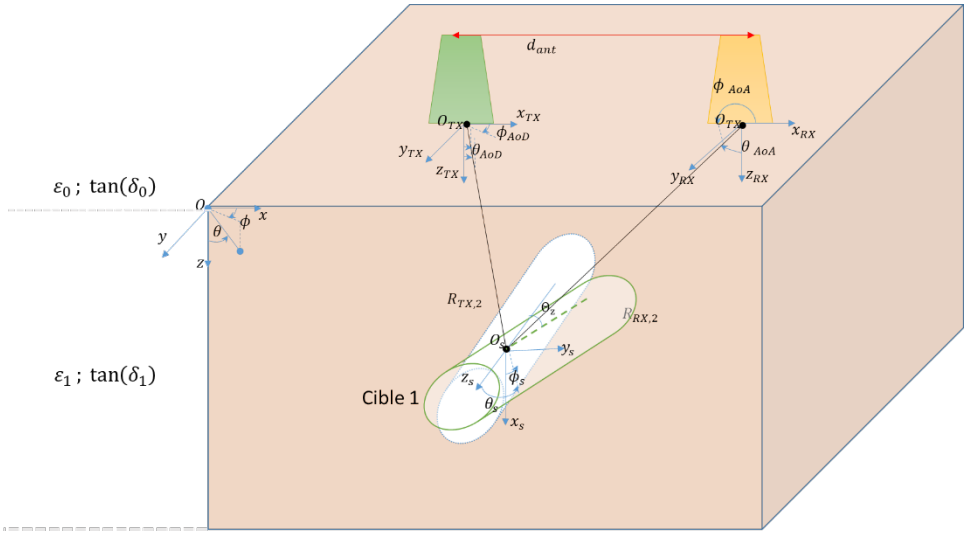

Figure 2.3: Geometrical configuration of a bistatic GPR measurement with a cylinder having an angle Θ_z in the horizontal reference frame.

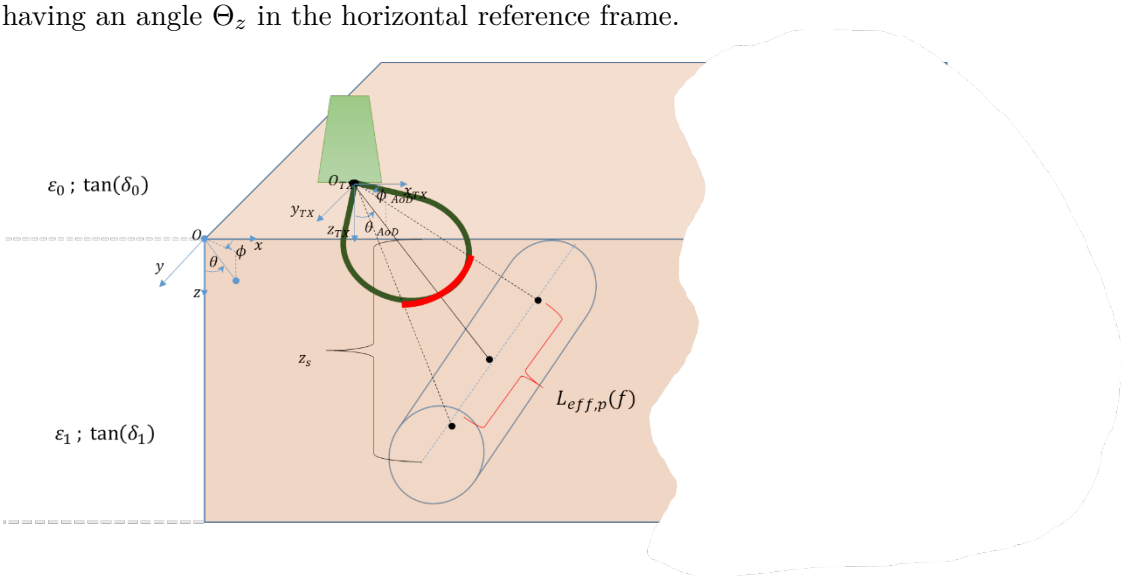

Figure 2.4: Principle of determination of the effective length of a cylindrical target seen by the GPR antenna

Then, from the orientation angle of the cylinder Θ_z with respect to the electric fields in the xy reference frame (Fig. 2.3), the backscatter amplitude matrix is obtained as follows:

$$\boldsymbol{S_{so}}(\phi_i, \theta_i, \phi_s, \theta_s, \Theta_z, f) = \begin{bmatrix} \cos\Theta_z & \sin\Theta_z & 0 \\ -\sin\Theta_z & \cos\Theta_z & 0 \\ 0 & 0 & 1 \end{bmatrix} \begin{bmatrix} S_s^{xx} & S_s^{yx} & S_s^{zx} \\ S_s^{xy} & S_s^{yy} & S_s^{zy} \\ S_s^{xz} & S_s^{yz} & S_s^{zz} \end{bmatrix} \begin{bmatrix} \cos\Theta_z & \sin\Theta_z & 0 \\ -\sin\Theta_z & \cos\Theta_z & 0 \\ 0 & 0 & 1 \end{bmatrix} \tag{2.6}$$

The coupling, including the direct link between the transmitting (Tx) and receiving (Rx) antennas and the multipath due to the presence of the ground near the antenna, is modelled using CST MWS®. Different relative distances between antennas and heights from the ground interface and different combinations of polarisation can be considered.

Equation (2.1) presents the backscattered response from a target buried in a homogeneous medium and illuminated by an electromagnetic field. This equation is used in the calculation of the complete GPR transfer function as follows:

$$H(f, m, n) = \sum_{s=1}^{Ns} H_s(f, m, n) + H_{co}(f, m, n) \tag{2.7}$$

Where s is the target index and N_s is the number of targets, $H_s(f, m, n)$ is the polarimetric radar equation of the s-th target (see Equation (2.1)) obtained with the m and n index antennas for Rx and Tx, respectively. The coupling of the ground antennas is represented by the transfer function H_{co} which is given by the CST MWS® simulator.

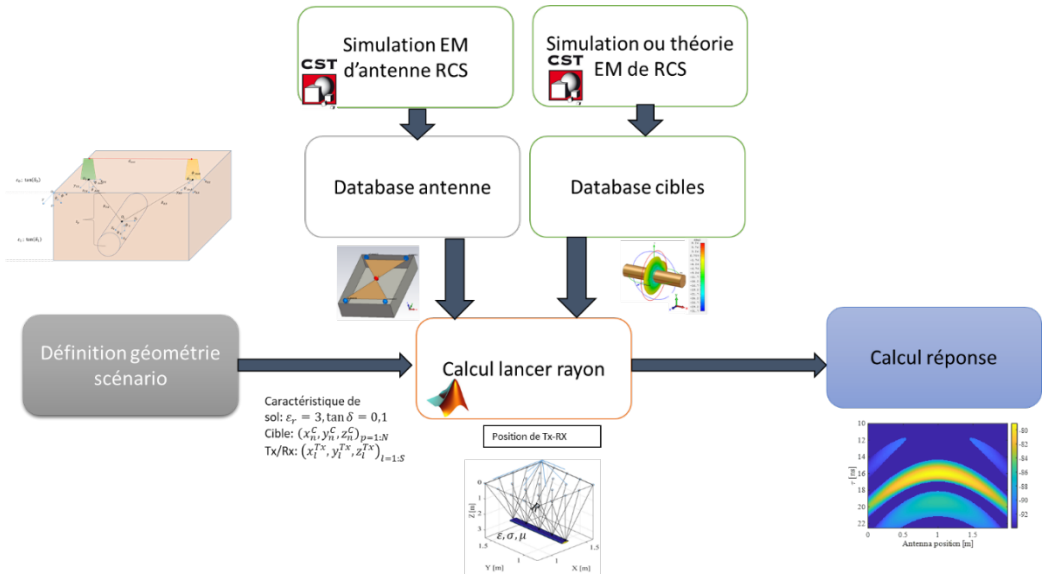

Figure 2.5: Implementation of the Matlab based model and CST MWS® hybridisation workflow with Matlab®.

The particularity of the model and its implementation (Fig. 2.5) is its ability to represent all kinds of polarisation combinations on a horizontal plane, to include the antenna impact (gains and polarisation) as well as the homogeneous ground characteristics for the radio channel simulation. This implementation allows to easily simulate MIMO configurations that would otherwise require significant computational resources.

As an example, the simulation of a GPR scenario, with a target at 4 m depth, the model requires less than 1 minute with a 1.6 GHz processor and 8 GB of RAM. The full-wave electromagnetic simulation represents a problem with 300 million unknowns that requires about 6 hours of computation with 30 cores 2.3 GHz and 130 GB of RAM.

2.2.2.2 Problem statement and acquisition configurations

To perform quantitative analysis, the same simulation parameters are used on both models. Both simulation are done using isotropic antennas along the x-axis spaced by $\lambda_{eff}/4$ which is the effective electrical length in a dielectric medium with permittivity $\varepsilon_r = 5$. The medium is assumed to be homogeneous, non-magnetic and lossless. Targets are perfect electric conductor spheres with 2 mm radius. The position of the target is at $x = 0.3$ m and $z = 0.8$ m with an array of $N_a = 20$ elements as illustrated in Fig. 2.6.

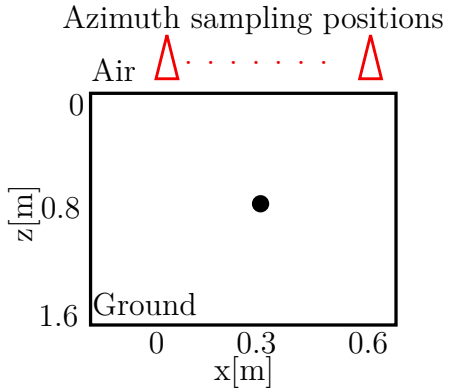

Figure 2.6: Setup configuration for scenario with 1 target at the centre of the array and $N_a = 20$.

GprMax simulates the response of the scene to a Ricker waveform with a centre frequency of 0.5 GHz and a bandwidth of 2 GHz, as shown in Fig. 2.7. In order

to obtain the channel transfer function, the Ricker waveform is compensated by using a deconvolution process.

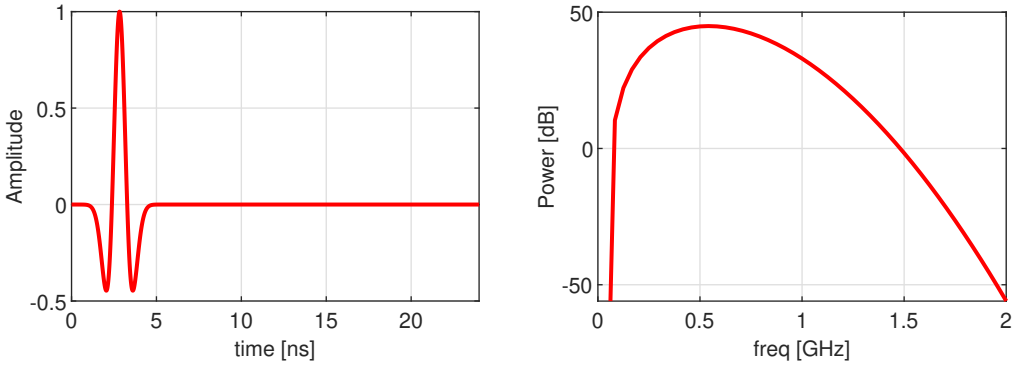

Figure 2.7: Ricker wave (a) Time domain and (b) Spectral domain.

2.2.2.3 Deconvolution

Deconvolution is an important pre-processing step made necessary by the fact that the focusing migration technique expect flat spectrum. The aim of deconvolution is to compensate the spectral pattern of the employed Ricker wave.

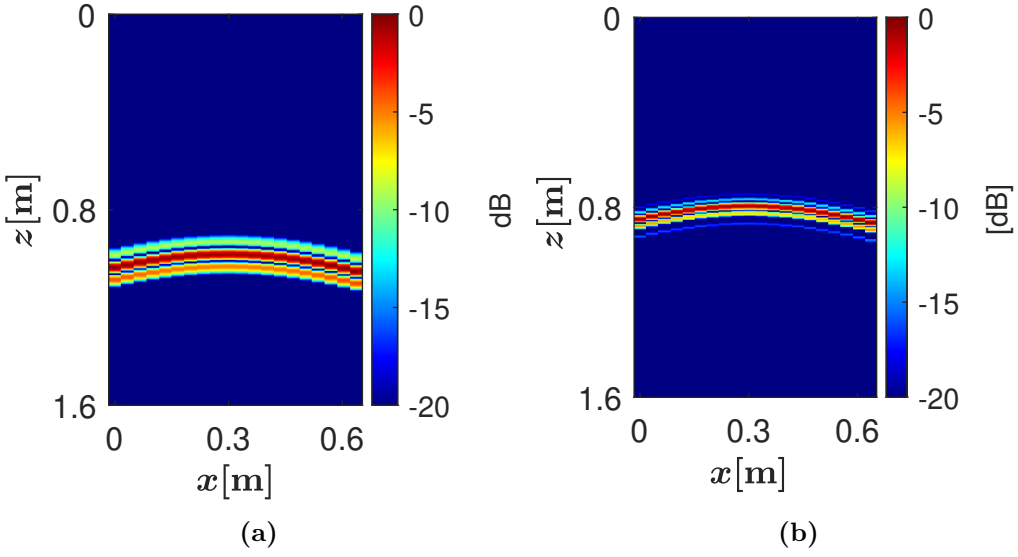

Figure 2.8: Scenario 1: Range focused GPR image results (a) without deconvolution and (b) with deconvolution.

The results in Fig. 2.8 presents range focused GPR image before deconvolution

(Fig. 2.8a) and after deconvolution (Fig. 2.8b).

To compensate the transmitted pulse, a deconvolution is performed using a Wiener filter [Yil01], which relies on the assumption that GPR data $\boldsymbol{y}(t)$ can be modelled as a convolution between the transmitted waveform $\boldsymbol{r}(t)$ and the scene impulse response $\boldsymbol{h}(t)$.

In the frequency domain the convolution can be represented as:

$$\boldsymbol{Y}(f) = \boldsymbol{H}(f) \cdot \boldsymbol{R}(f) \tag{2.8}$$

Where $\boldsymbol{Y}(f)$ is the Fourier transform of $\boldsymbol{y}(t)$.

Wiener filter aims to limit the amount of noise at the output of deconvolution and uses ε, the dumping factor (small number) as:

$$\boldsymbol{H}(f) \approx \boldsymbol{Y}(f) \cdot \frac{\overline{\boldsymbol{R}(f)}}{\overline{\boldsymbol{R}(f)}\boldsymbol{R}(f) + \varepsilon} \tag{2.9}$$

2.2.2.4 Quantitative Comparison Results

Simulation results for both gprMax and CEA GPR hybrid propagation channel models are shown in Fig. 2.9 and Fig. 2.10 respectively.

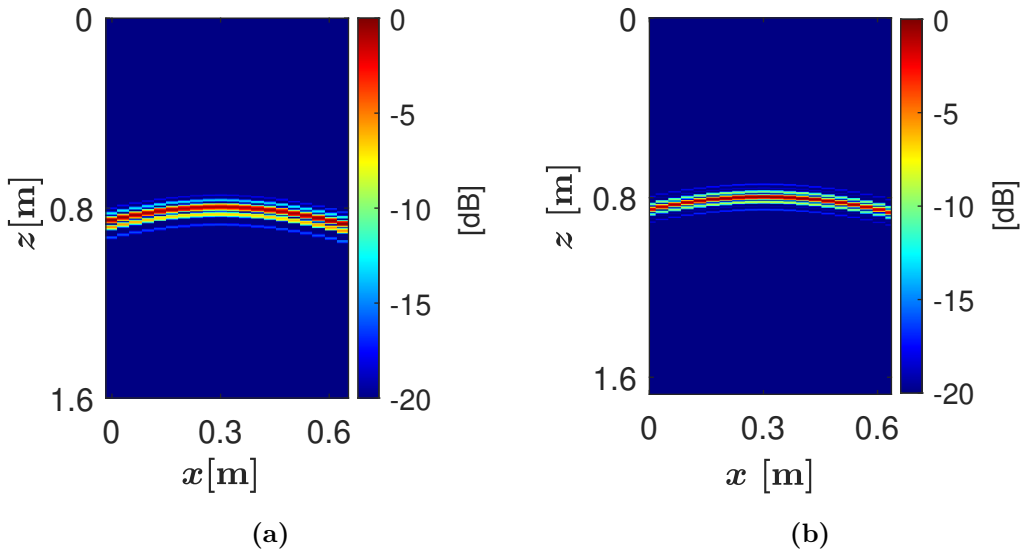

Figure 2.9: Range focused GPR image results (a) gprMax and (b) CEA GPR hybrid model.

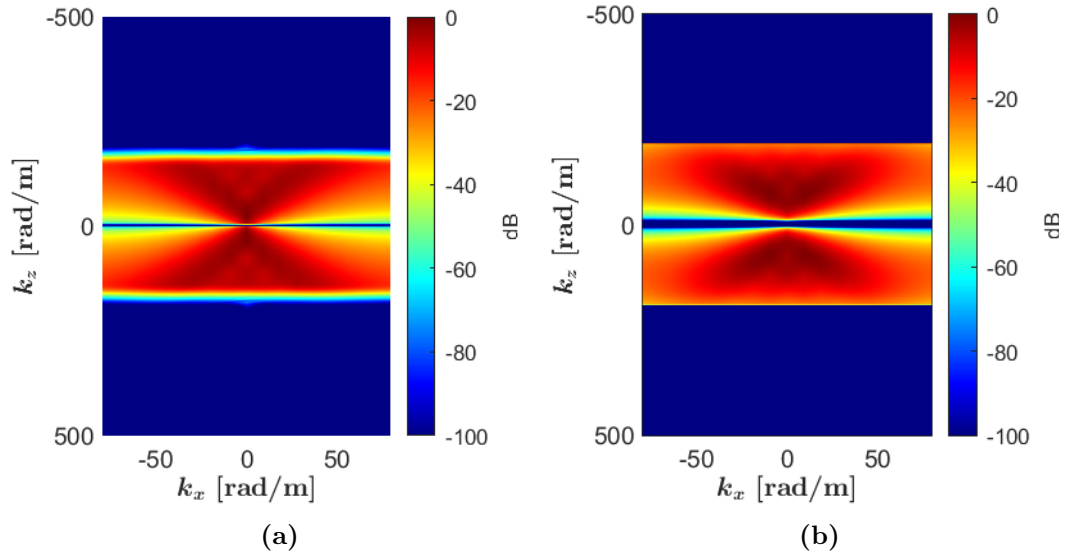

Figure 2.10: Range focused GPR 2D FT image results (a) gprMax and (b) CEA GPR hybrid model.

Both simulations had similar hyperbolas showing the target true position is at the apex of hyperbola located at correct depth and azimuth position. Also similar spectrum are observed between the two simulations hence this validate the gprMax modelling and the deconvolution process with respect to the CEA based model.

2.3 Problem statement and acquisition configurations

In this section, GPR configuration scenarios are introduced to study the spatial resolution limitation of conventional GPR focusing methods along range and azimuth directions.

GPR data were simulated by using gprMax tool [War21] using isotropic antennas along the x-axis spaced by $\lambda_{eff}/4$ which is the effective electrical wavelength in a dielectric medium with permittivity $\varepsilon_r = 5$. The medium is assumed to be homogeneous, non-magnetic and lossless.

A Ricker waveform with a centre frequency of 0.5 GHz and a bandwidth of 2 GHz is used as presented in Fig. 2.7. Targets are perfect electric conducting cylinder (a cylinder will be a surface in 2D simulations) with a 2 mm radius.

The Fourier resolution derived at 0.8 m using Eqn 1.14 and Eqn 1.15 are shown in Table 2.1.

Table 2.1: Fourier resolution analysis at $z = 0.8\ m$

Azimuth resolution (δ_x)	18 cm
Range resolution (δ_z)	3.35 cm

2.3.1 Case 1 : Range resolution analysis scenarios

2.3.1.1 Geometrical Configuration

Table 2.2 presents the GPR acquisition parameters for range resolution analysis (δ_z) for targets located around the coordinates x_0, z_0 with an array of N_a elements. Scenario 1 considers a single target whereas scenario 2 deals with two targets separated by a spacing of dz in the range direction. Scenario 3 considers the case of targets with azimuth position which is not centred with respect to the array coordinates. This kind of acquisition is often qualified as squinted.

Table 2.2: GPR scenario Case 1: Range resolution analysis

Scenario	x_0	z_0	dz	N_a
1 (1 target)	0.3 m	0.8 m	–	20
2.a (2 targets)	0.3 m	0.8 m	50 cm	20
2.b (2 targets)	0.3 m	0.8 m	2 cm	20
3 (2 targets)	0.05 m	0.8 m	2 cm	20
3.b (2 targets)	0.05 m	0.8 m	2 cm	4

2.3.1.2 Classical Imaging Results

GPR range focused data shows up in form of hyperbola due to the range migration induced by change of radar target distance when moving from one element of the equivalent azimuth array to the other as indicated in Fig. 2.11b.

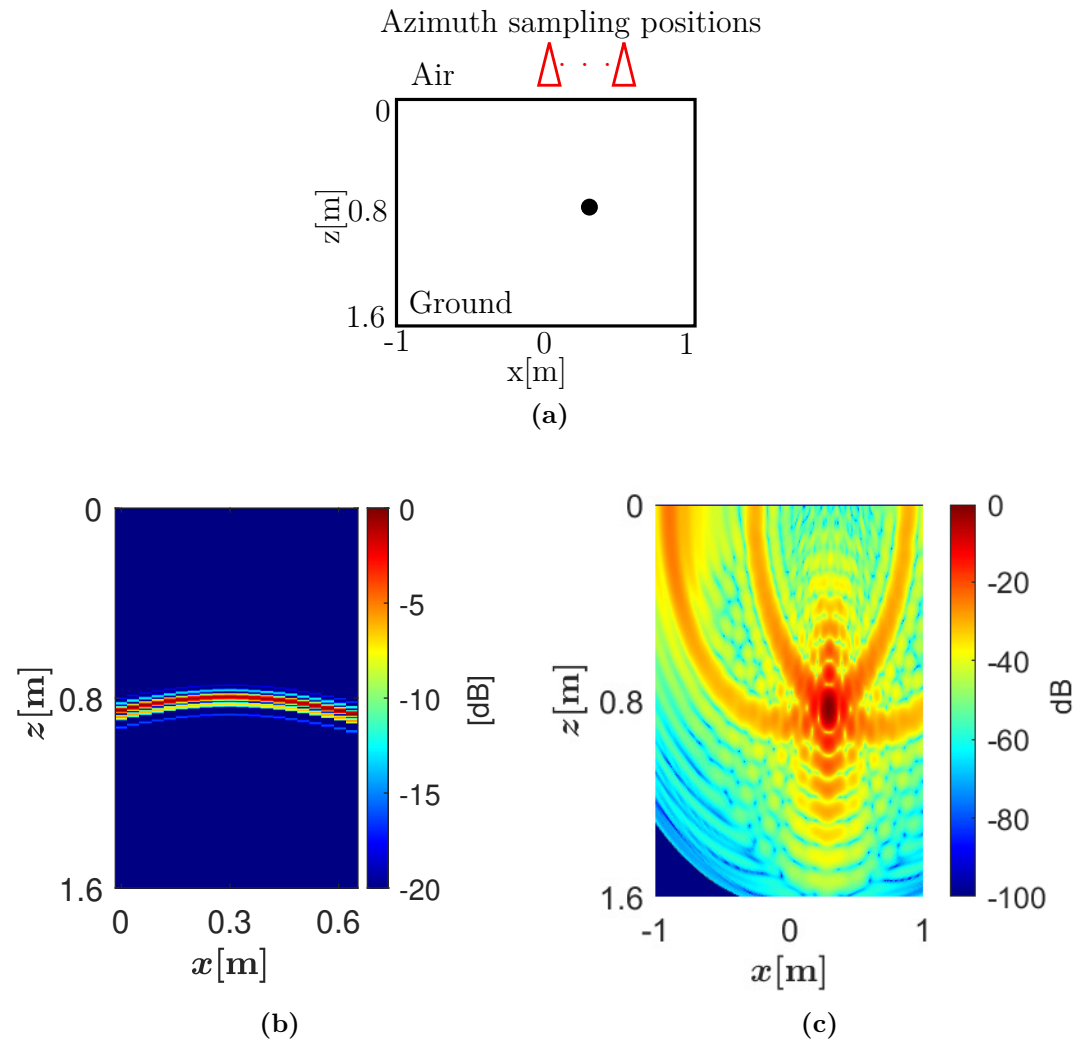

Figure 2.11: Scenario 1 with a 1 target at the centre of the array and $N_a = 20$: (a) Setup configuration, (b) Range focused image and (c) 2D BP focused image.

2D focusing results using the back propagation algorithm leads to the results shown in Fig. 2.11c and correctly locates the target. BP results for scenario 2.a are given in Fig. 2.12b.

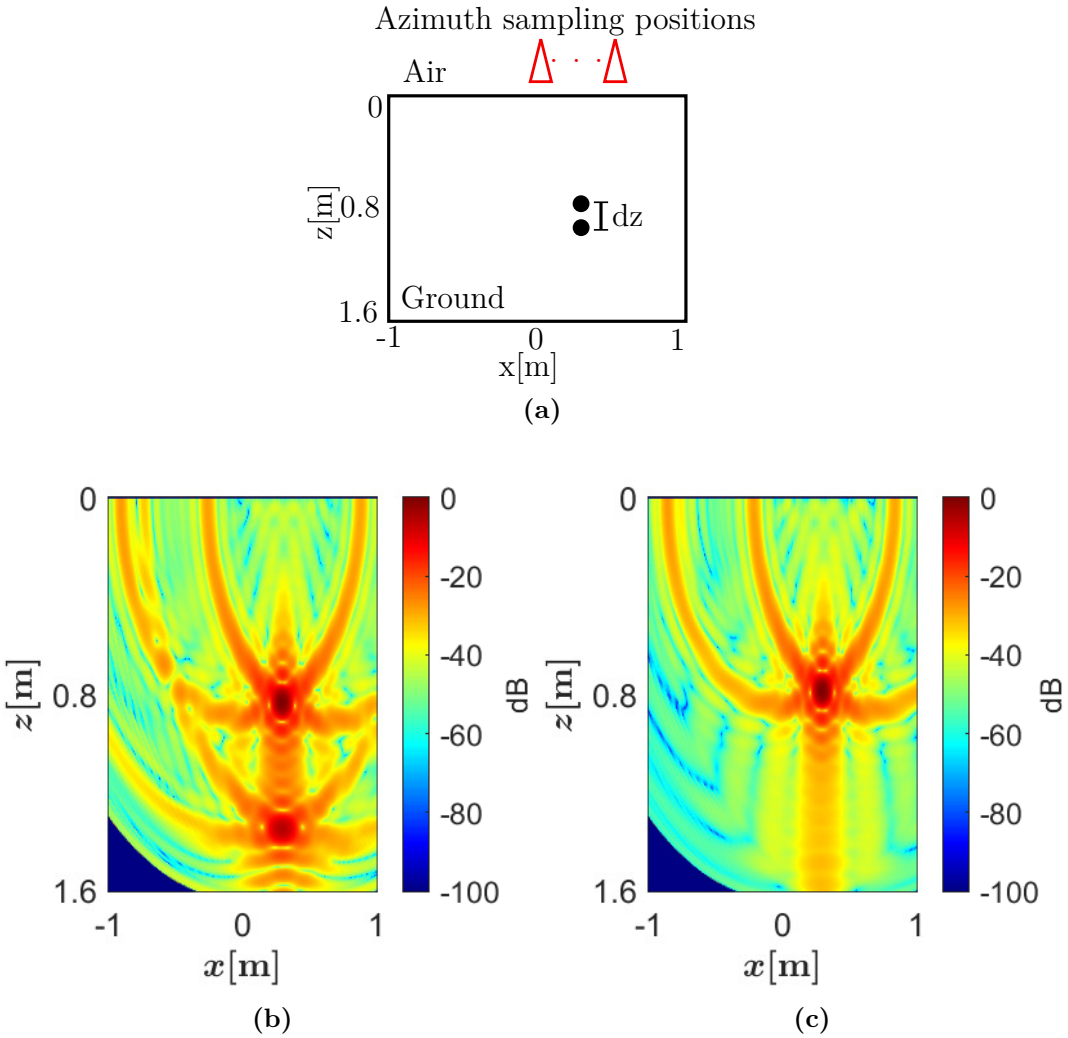

Figure 2.12: Scenario 2 with 2 targets at the centre of the array and $N_a = 20$: (a) Setup configuration, (b) BP focused results for $dz = 50$ cm (scenario 2.a) and (c) BP focused results for $dz = 2$ cm (scenario 2.b).

When the spacing dz is larger than the range resolution both targets can be discriminated whereas in the case where the spacing is smaller than the range resolution, it was not possible to separate the two targets as indicated in Fig. 2.12c.

The same conclusion can be observed with scenario 3 (i.e squinted configuration) with two targets that are located on the side of the illuminating array that are separated by short range spacing ($dz = 2\ cm$).

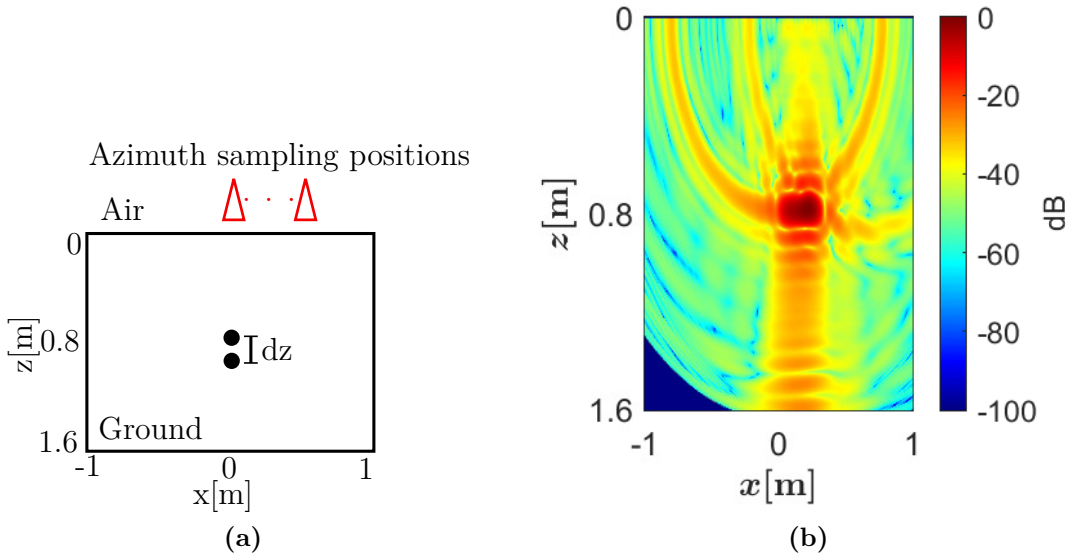

Figure 2.13: Scenario 3 with $N_a = 20$ and 2 targets at the side of the array separated at $dz = 2$ cm: (a)Setup configuration and (b) BP focused results.

2.3.2 Case 2 : Azimuth resolution analysis scenarios

2.3.2.1 Geometrical Configuration

The same configurations that were done previously along range direction are implemented along azimuth direction as presented in Table 2.3. These scenarios considers two targets with different azimuth spacing (δ_x) and investigate the case of squinted acquisition when the targets are located away from the centre of the array in the azimuth direction.

Table 2.3: GPR scenario Case 2: Azimuth resolution analysis

Scenario	x_0	z_0	dx	N_a
4.a (2 targets)	0.3 m	0.8 m	20 cm	20
4.b (2 targets)	0.3 m	0.8 m	4.75 cm	20
5.a (2 targets)	0.05 m	0.8 m	4.75 cm	20
5.b (2 targets)	0.05 m	0.8 m	4.75 cm	4

2.3.2.2 Classical Imaging Results

Similarly to range resolution analysis scenarios, we observe that BP is able to discriminate two targets separated by offset larger than δ_x ($dx = 20\ cm$) in Fig. 2.14b (scenario 4.a). When the offset was reduced to offset which was less than azimuth resolution, $dx < \delta_x$ ($dx = 4.75\ cm$), BP focused two targets as single targets as presented in Fig. 2.14c (scenario 4.b).

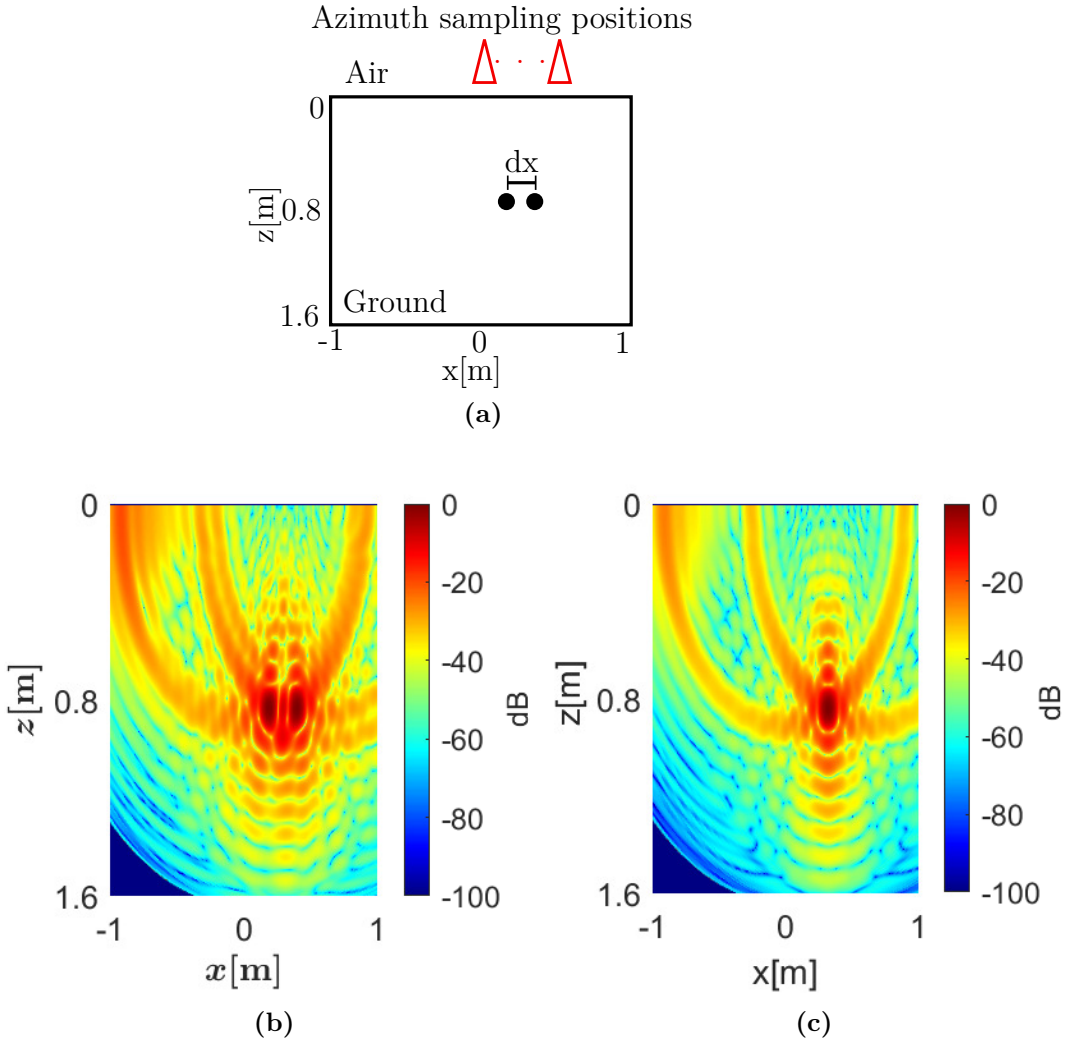

Figure 2.14: Scenario 4 with 2 targets at the centre of the array and $N_a = 20$: (a) Setup configuration, (b) BP focused results for $dx = 20$ cm (scenario 4.a) and (c) BP focused results for $dx = 4.75$ cm (scenario 4.b).

When the targets were observed with a squint configuration (scenario 5.a) BP

fails to separate them. on the side of the array, BP still failed to separate the two targets. Additionally, we notice that focused results of targets at the side of the array starts to spread in multiple range cell (Fig. 2.15b) compared to focused targets at the centre of the array in Fig. 2.14c.

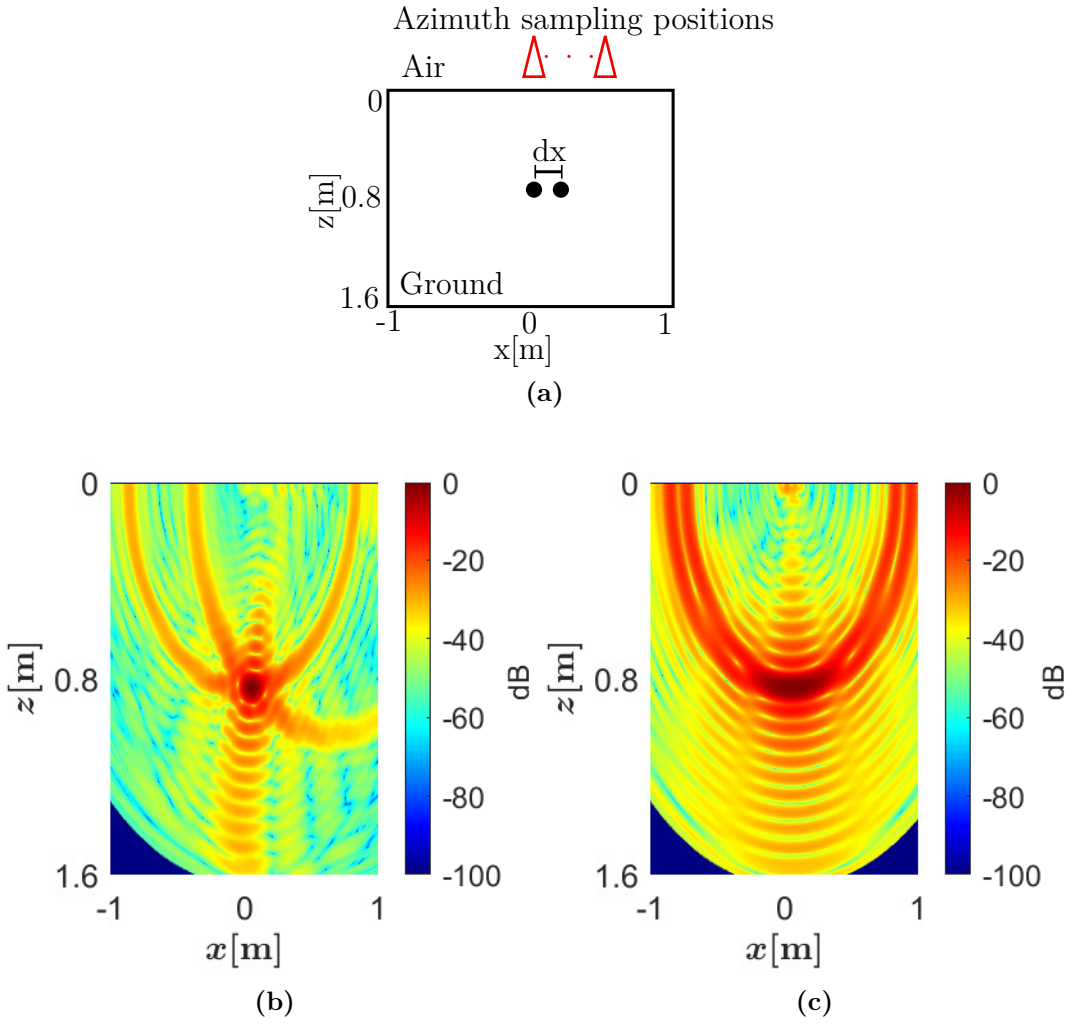

Figure 2.15: Scenario 5 with 2 targets at the side of the array and $dx = 4.75$ cm: (a) Setup configuration, (b) BP focused results for $N_a = 20$ (scenario 5.a) and (c) BP focused results $N_a = 4$ (scenario 5.b).

When the number of number of azimuth sampling positions are reduced to 4 (5 times smaller the original 20 azimuth sampling positions), BP has poor focused results as indicated in Fig. 2.15c (scenario 5.b).

In conclusion, this analysis shows very typical situation in GPR characterisation where the spacing between two targets is smaller than azimuth or range resolution and for given length of the azimuth array, one may not be able to separate the response of such scatterer. So in this case the use of spectral analysis techniques is expected to improve resolution, focusing and performance.

2.4 Compensation of near-field wide bandwidth effects

According to the geometrical configurations, the proposed scenarios correspond to near field configuration with respect to the Fraunhofer distance d_F in (2.10). This implies that, the configuration is in near field when z_0 is smaller than d_F. Given that L is synthetic aperture and λ_{eff} is the effective lambda, d_F is expressed as:

$$d_F = 2L^2/\lambda_{eff} \tag{2.10}$$

For instance, for 20 number of azimuth sampling positions, $L = 0.64\ m$ and $\lambda_{eff} = 0.134\ m$, hence $d_F = 6\ m$. Therefore since $z_0 = 0.8\ m$, this configuration is in near field.

The evolution of phase delays from one element to the other along the azimuth direction is not linear. This means that still Specan techniques may be used but modification of the expression of steering vector is required based on the depth

In addition, in wide band configurations the propagations delay measured for different azimuth positions became comparably larger to the range resolution. In consequence the response of target stretch over different range cell as presented in Fig. 2.16.

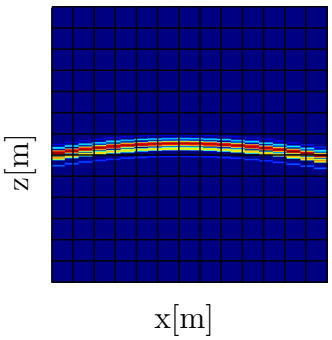

Figure 2.16: Range focused data showing non-linear range cell migrations

The application of Specan techniques to near field and wide band configurations requires some modifications [Mar+98]. One of the most convenient solution consist in correcting for the curvature for these effects using a classical BP technique which has limited resolution but it is exact in terms of focusing accuracy, and then apply Specan techniques on the focused results. By doing this, the estimation capability of Specan methods will be enhanced [LS96; DeG98].

As shown in Fig. 2.17, the range migration may cause the response of a target to spread over several range positions and making the compensation on the analysis of the phase history difficult. For this reason we focus on a 2D polar grid as proposed in [Jou+17]

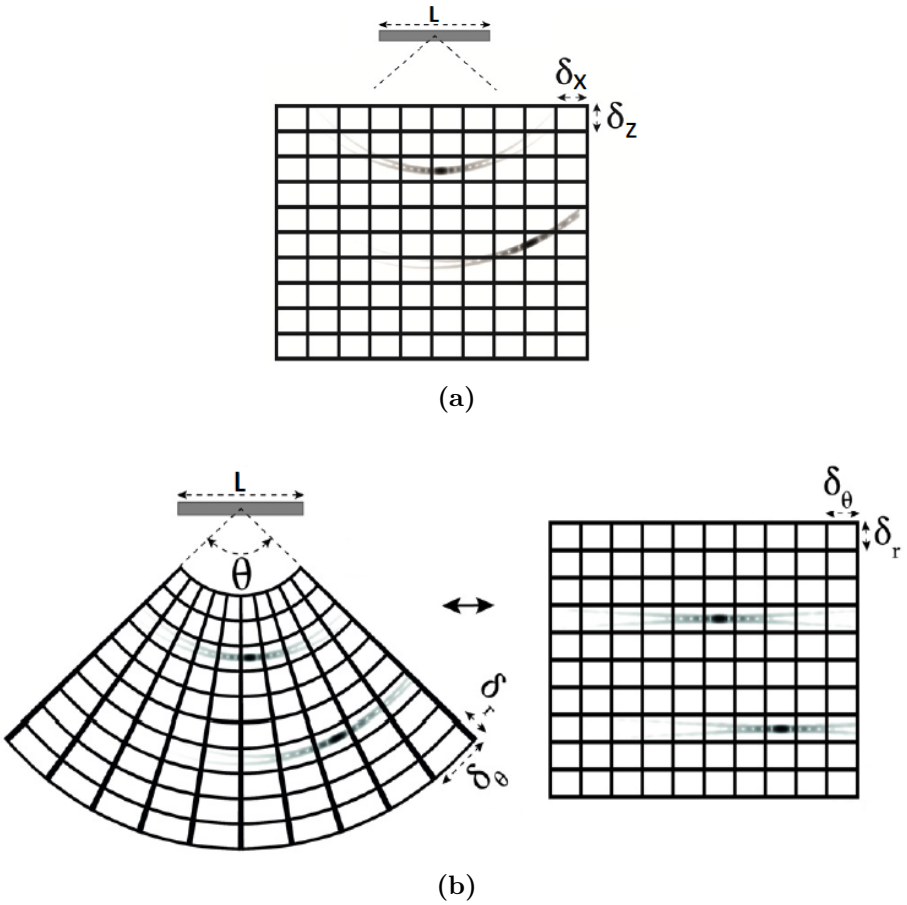

Figure 2.17: Imaging geometry for BP focused data on: (a) a 2D Cartesian grid and (b) a 2D polar grid [Jou+17].

As observed in Fig. 2.18 focusing in polar grid tends to concentrate the spectrum on to a trapezoidal and quasi-rectangular domain which is well adopted to the Specan analysis formalism mentioned earlier in this manuscript.

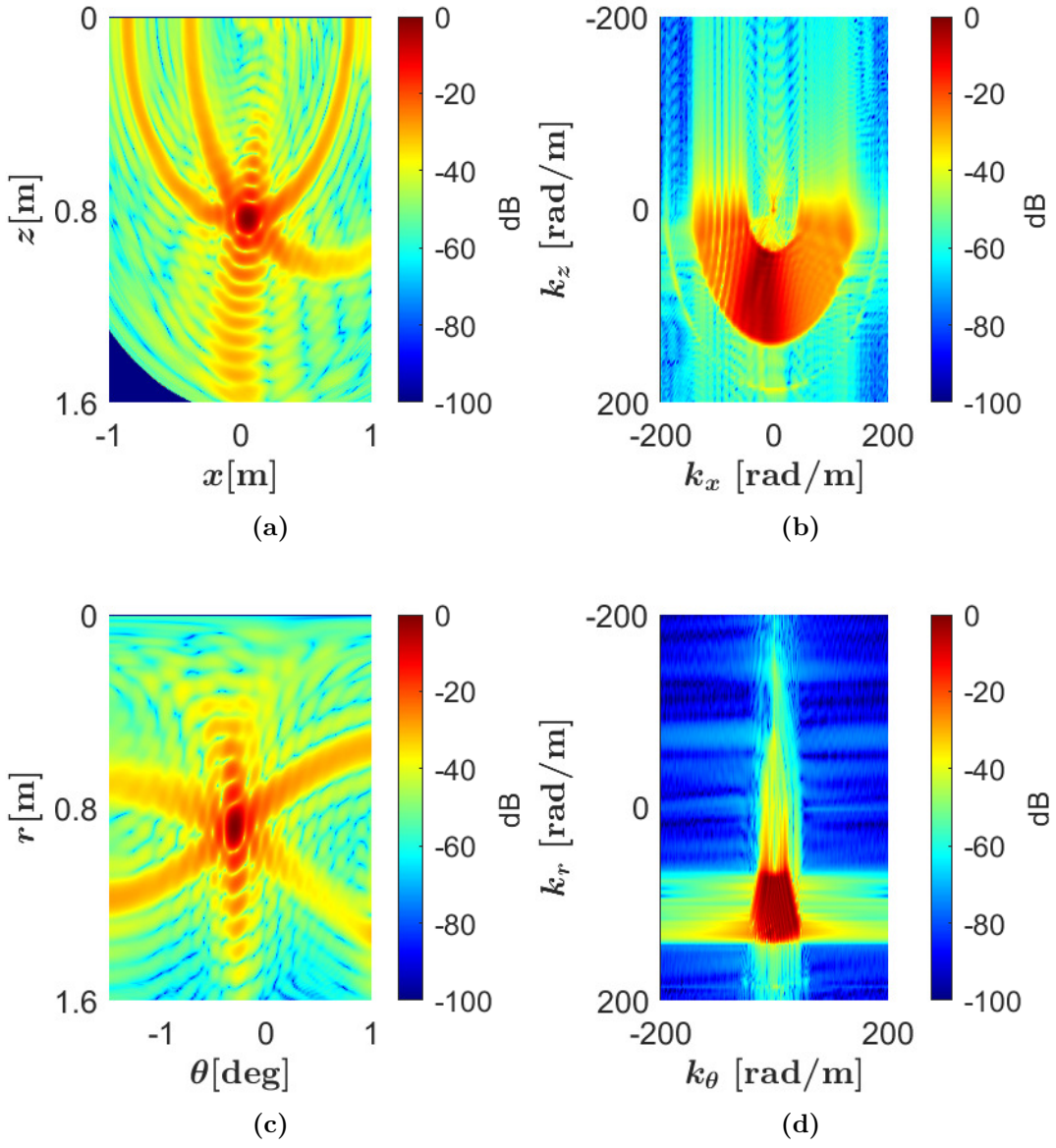

Figure 2.18: Case 2 (Azimuth resolution) : Scenario 5.a (a) Cartesian BP image, (b) Cartesian BP spectrum, (c) Polar BP image, (d) Polar BP spectrum.

2.5 Covariance matrix estimation

It is necessary to adequately estimate the covariance data matrix in order to enhance estimation capability of Specan methods. Estimation of covariance matrix is very application dependent. Basically N realisations are required (i.e number of frequency points of selected azimuth cell vector or number of azimuth samples for selected range cell vector for range resolution and azimuth resolution respectively). In the most convenient situation independent realisations are preferred as they bring the maximum information. On the contrary, when data are correlated only less information can be obtained. Classical estimation of covariance matrix is given as Maximum likelihood estimation in Gaussian case [KV96]. This is done by replacing expectation in (1.20) with sum of N realisations as shown below:

$$\hat{\boldsymbol{R}} = \frac{1}{N} \sum_{n=1}^{N} \boldsymbol{y}\boldsymbol{y}^{H} \tag{2.11}$$

2.5.1 1D spectral smoothing

In the literature [Jou+17; KV96; Mar+98] spatial smoothing is used to decorrelate the data which is simply a sliding window in spatial domain in only one direction. In this work, instead of sliding in spatial domain this sliding window will be applied in frequency domain of a given direction (either along range or along azimuth) of GPR focused image hence the term 1D spectral smoothing is used instead.

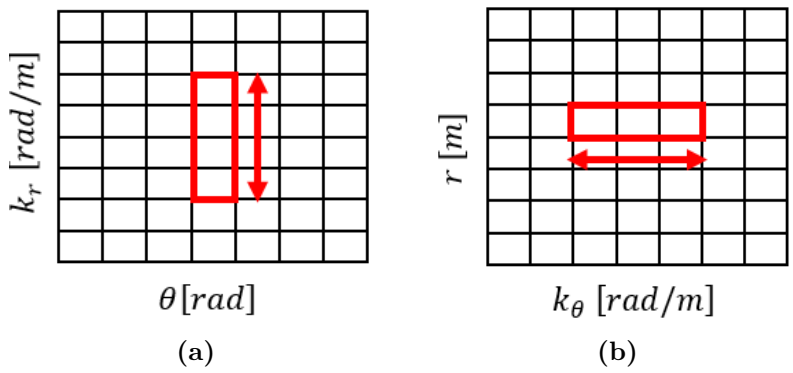

Figure 2.19: 1D Spectral smoothing along : (a) range (b) azimuth.

As presented in Fig. 2.19, the sliding is done in only one direction i.e along range (Fig. 2.19a) or along azimuth (Fig. 2.19b) directions, depending on the application.

Then the data covariance matrix is obtain by averaging the data covariance matrices obtained from each window. In the end this option reduce resolution from full length $1/N$ full to length of the sliding window $1/N_{wind}$. In configuration considered here, range resolution is better i.e 3.35 $cm = \lambda_{eff}/4$ compared to azimuth resolution i.e 18 $cm = 1.3\lambda_{eff}$. So in spite of reduction of resolution resulted from the length of sliding window, we have shown that Specan methods still able to improve significantly range resolution thanks to estimation of covariance matrix by 1D spectral smoothing.

2.5.2 2D spectral smoothing

But as for azimuth resolution, the length of the available synthetic aperture is usually already small i.e for the scenario with only 4 antenna (case), therefore reducing the full length of array to small length of sliding window hinder resolution ability of Specan method. So instead in this work we use 2D Spectral smoothing, described in [LS96; DeG98], in order to increase the number of looks along azimuth direction i.e keep full array elements N which will maximise the azimuth resolution.

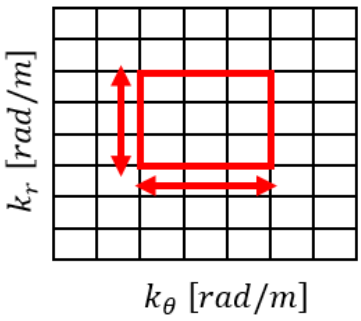

Figure 2.20: 2D Spectral smoothing along both range and azimuth.

2D spectral smoothing involves sliding in frequency domain in both dimensions i.e along azimuth and along range as shown in Fig. 2.20. Several realisation of decorrelated GPR data will be obtained with reduced realisation either in azimuth or in range. Therefore choosing the size of the window in a given direction depends

on the configuration as mostly the resolution in range is better than in azimuth so for instance in our case we have 3.35 cm resolution along range and only 18 cm resolution along azimuth. On that account, little resolution in range may be spent to increase the number of looks along azimuth and in our case we increased this number up to N. This imply that, full antenna array length was maintained for covariance matrix estimation. As a result, high estimation capability of Specan methods was facilitated.

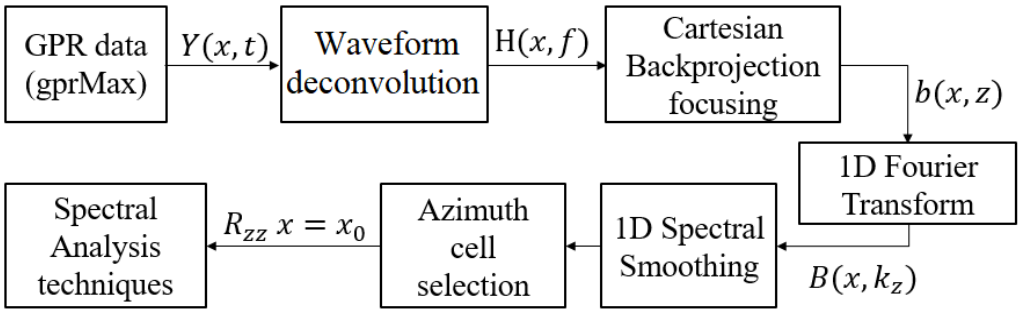

Figure 2.21: Schematic diagram of algorithm developed for range resolution improvement.

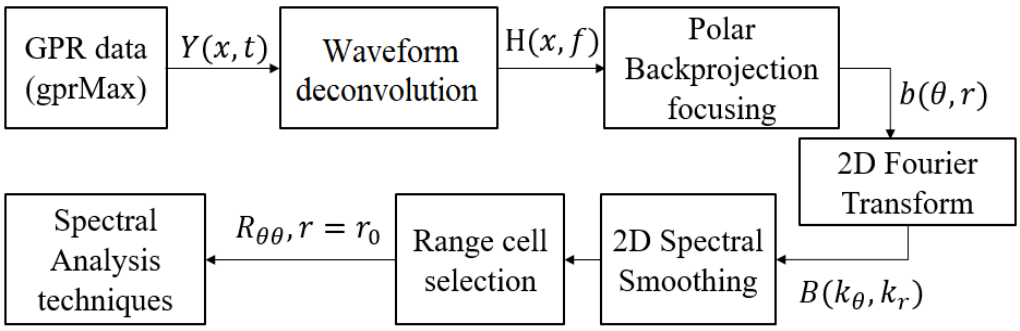

Figure 2.22: Schematic diagram of algorithm developed for azimuth resolution improvement.

The algorithms developed in this work to improve range resolution and azimuth resolution are summarised in the following steps as presented in Fig. 2.21 and Fig. 2.22 respectively:

- The GPR data $Y(x,t)$ are deconvolved by a Wiener filter to compensate the used waveform then by 1D FT to obtain $H(x,f)$.
- $H(x,f)$ is focused by Cartesian BP focusing algorithm to obtain $b(x,z)$ then 1D FT to get $B(x,k_z)$.
- 1D spectral smoothing is done on $B(x,k_z)$ and covariance matrix $\hat{R}_{zz}, x = x_0$ will be estimated from a selected azimuth cell $(x = x_0)$.
- Finally, Specan methods are applied for position estimation through $(P(z_i))$, the focusing criteria of Specan techniques.

And respectively for azimuth resolution :

- The GPR data $Y(x,t)$ are deconvoluted by a Wiener filter then 1D FT is done to get $H(x,f)$.
- $H(x,f)$ is focused by Polar BP focusing algorithm to obtain $b(\theta,r)$ followed by 2D FT to obtain $B(k_\theta,k_r)$.
- 2D spectral smoothing is done on $B(k_\theta,k_r)$ and covariance matrix $\hat{R}_{\theta\theta}, r = r_0$ will be estimated from a selected range cell $(r = r_0)$.
- Finally, Specan methods are applied for position estimation through $(P(\theta_i))$, the focusing criteria of Specan techniques.

2.6 GPR Imaging using Specan

For simulated GPR data, SNR of 20 dB was considered with 200 realisations.

2.6.1 Range resolution results : Case 1

Specan methods aiming to improve the range resolution are applied to GPR focused data presented in Fig. 2.13 (scenario 3) and results are shown in Fig. 2.23.

In both processing configurations, non-parametric methods such as BF and CP can not separate the two targets responses despite the better resolution of CP with respect to BF as their width of the beam associated with their peaks was relatively large.

On the other hand, the rest of the methods were able to distinguish the two targets. High resolution parametric methods (MUSIC, OPM, Root-MUSIC,

Root-OPM, and ESPRIT) leads to better resolution results compared to non-parametric methods (BF and CP) as their estimate does not depend on the signal bandwidth but rather on the quality of the estimate of covariance matrix, $\hat{R}$. OPM-based methods do not use an eigenvalue decomposition to estimate the noise subspace but instead use the propagator estimator which is computational efficient. But since the propagator is developed in ideal conditions its performance may degrade on extreme conditions.

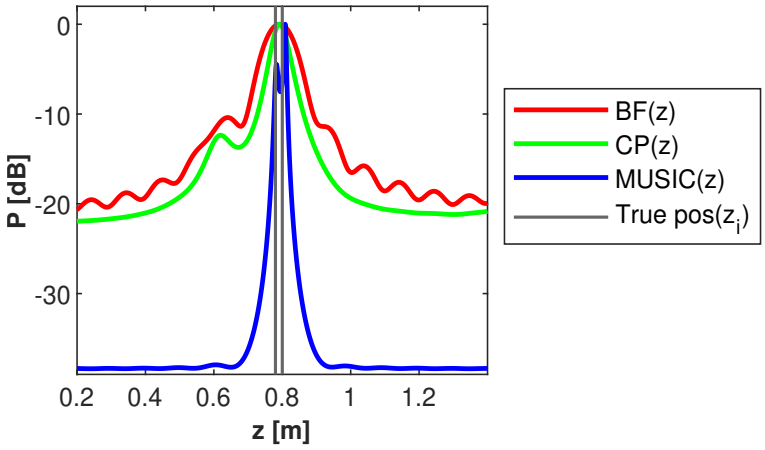

(a)

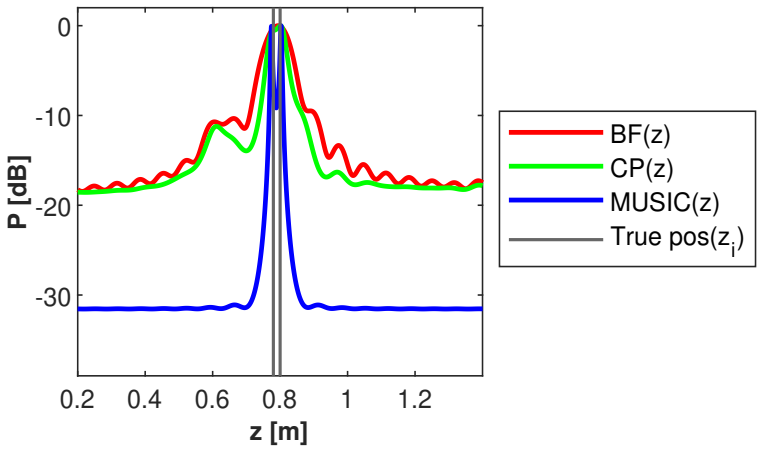

(b)

Figure 2.23: Specan objective functions for scenario 3 with $N_a = 20$ and 2 targets at the side of array separated by $dz = 2$ cm: (a) Approximately quarter bandwidth (number of frequency samples=16 out of 48 samples) results (b) Approximately half bandwidth (number of frequency samples=24 out of 48 samples) results.

SSF and DML are parametric methods that estimate the position by optimising a multidimensional criteria. They are more robust and have a high overall accuracy despite a high computational cost.

Furthermore, in order to estimate the actual reflectivity of the image observed using parametric techniques, additional step is required which is typically implementing a Least square estimation [Mar+98] [SM+05].

Finally, in Fig. 2.23 we observe that, resolution improve with increase of number of frequency samples as illustrated with the shape of Specan objective function of Fig. 2.23b (number of frequency samples=24 out of 48 samples) which are narrower than Specan objective function of Fig. 2.23a (number of frequency samples=16 out of 48 samples).

2.6.2 Azimuth resolution results : Case 2

Similarly, Specan methods were also applied along azimuth to improve azimuth resolution. As aforementioned, BP focusing algorithm was implemented in Polar grid for case 2. In addition to that, the implementation of 2D spectral smoothing described before was used in order to increase number of looks while keeping the full array length .

First, Specan method were applied to GPR polar focused data in scenario 5.a (Fig. 2.18c) and scenario 5.b respectively.

The obtained results are presented in Fig. 2.24. The results shows that except for BF and CP, the rest of the Specan methods were able to distinguish two targets for configuration with 4 azimuth sampling positions (scenario 5.b) and 20 azimuth sampling positions (scenario 5.a) respectively. For the case with 4 azimuth position, it was possible to discriminate the two targets since 4 azimuth positions is larger than the available number of 2 targets. Therefore, it is possible to go down to shorter arrays as long as number of elements is larger than the number of targets observed.

In addition to that, we observe that the resolution improve with increase of number of azimuth sampling positions i.e the beamwidth of Specan objective function for the case of 20 azimuth sampling positions i.e Fig. 2.24b is narrower than the case with only four number of azimuth sampling positions i.e Fig. 2.24a.

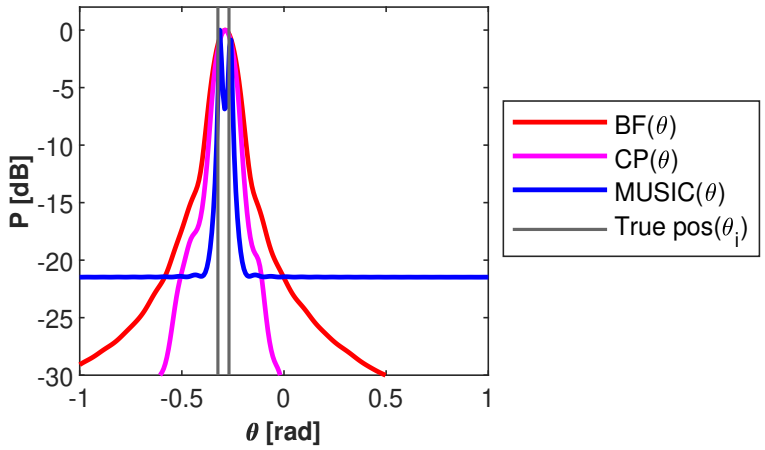

(a)

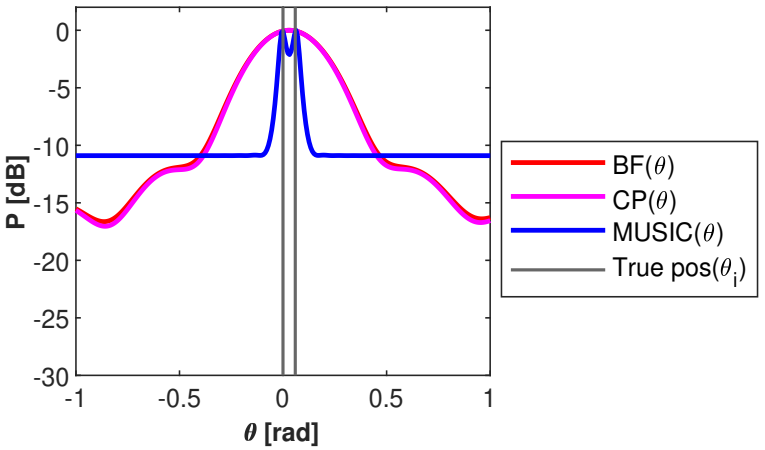

(b)

Figure 2.24: Specan objective function for scenario 5 with 2 targets at the side of the array separated at $dx = 4.75$ cm: (a) $N_a = 20$ (scenario 5.a) results and (b) $N_a = 4$ (scenario 5.b) results.

On the other hand, Specan techniques $RMSE$ was analysed in presence of noise by taking into account SNR of -10 dB to 20 dB as shown in Fig. 2.25. The results shows that $RMSE$ increases as the level of noise decreases. The estimation accuracy of OPM-based methods (OPM and Root-OPM) degrade significantly as noise increases.

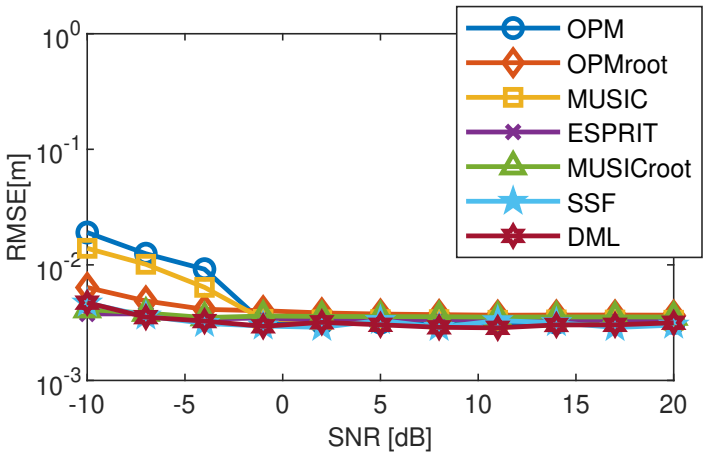

Figure 2.25: RMSE of Specan methods with respect to noise levels for scenario 3 with $N_a = 20$ and 2 targets at the side of array separated at $dz = 2$ cm (number of frequency samples=48).

Finally, Specan methods $RMSE$ was analysed with respect to number of frequency samples as presented in Fig. 2.26.

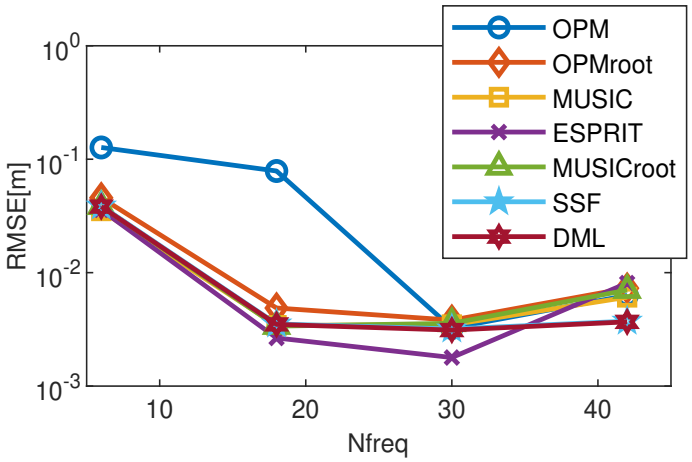

Figure 2.26: RMSE of Specan methods with respect to number of frequency samples for scenario 3 with $N_a = 20$ and 2 targets at the side of array separated at $dz = 2$ cm (SNR = 20 dB).

In this case it is clearly seen that $RMSE$ increases with increase of number of frequency points. Furthermore, at approximately half bandwidth the Specan methods reach their maximum accuracy and after the estimation degrade due to the fact that more samples are selected for spectral smoothing which lead to less number of sub arrays which implies a covariance matrix is estimated with data

that are not properly de-correlated. This results conforms what was shown by [Le 07].

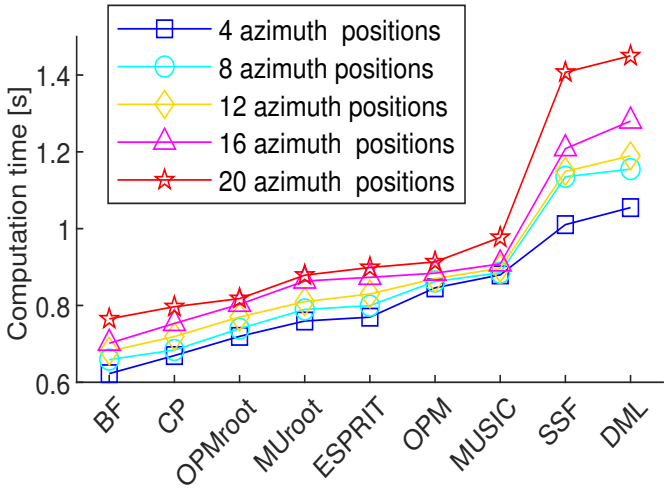

Figure 2.27: Computation time of Specan techniques for different array widths for 2 targets with an azimuth spacing of $dx = 4.75$ cm.

Finally, the computational time of different Specan algorithms were analysed for varying numbers of azimuth sampling positions and presented in Fig. 2.27. The parameters of the computer on which the simulations were run are: Intel(R) Core(TM) i5-10210U CPU @ 1.60GHz 2.11 GHz with RAM memory of 16,0 Go and 64-bit operating system, x64 processor.

Non parametric methods (BP and CP) are simple to implement so they have the lowest computation time. Furthermore, BP and CP methods do not require the number of signals to be known in advance like the rest of the Specan methods studied in this work.

OPM-based (OPM and Root-OPM) methods have low computation time compared with MUSIC-based (MUSIC and Root-MUSIC) methods, as they do not use eigenvalue decomposition to estimate the noise subspace.

Root methods (Root-OPM and Root-MUSIC) have smaller computational time compared with the corresponding peak-search versions (OPM and MUSIC). This is because root methods do not perform exhaustive search through all possible steering vectors but they give direct parameter estimation by finding roots of

polynomial of the objective function. Even though root methods are computationally attractive, they require to use uniform linear arrays.

Lastly, multidimensional methods (SSF and DML) have largest computational time since they need to solve a multidimensional non-linear optimisations problem to estimate required parameters. They are robust and accurate at the cost of heavy computational burden.

2.7 GPR imaging using Specan with heterogeneous targets

2.7.1 Geometrical Configuration

The simulation conditions used in this case are similar to the one in subsection 2.2.2.2.

Table 2.4: GPR scenarios for heterogenous targets

Scenario	Target radius	x_0	z_0	dx	N_a
1	$r_{PVC} = 100\ mm$, $r_{PEC} = 20\ mm$	$0.3\ m$	$0.8\ m$	$r_{PVC} + r_{PEC} = 120\ mm$	20
2	$r_{PVC} = 50\ mm$, $r_{PEC} = 20\ mm$	$0.3\ m$	$0.8\ m$	$r_{PVC} + r_{PEC} = 70\ mm$	20

Scenario 1 in Table 2.4 considers 20 azimuth sampling positions with one target consisting of a PVC pipe with permittivity of $\varepsilon_r = 1$ and 100 mm radius, whereas the other target is PEC pipe with radius of 20 mm. The targets touches each other since the azimuth offset dx which is from centre of the PVC target to the centre of the PEC target is the sum of their radius i.e $dx = r_{PVC} + r_{PEC} = 120$ mm as illustrated in Fig. 2.28a. The second scenario reduce the radius of the PVC target to 50 mm whereas the PEC target remains identical to the one of scenario 1. So their azimuth offset is $dx = r_{PVC} + r_{PEC} = 70$ mm as shown in Fig. 2.29a.

2.7.2 Imaging results

Fig. 2.28 presents the results of scenario 1 i.e $dx = r_{PVC} + r_{PEC} = 120$ mm. The range focused image is given in Fig. 2.28b and the hyperbolas for the two

targets are hardly identifiable.

BP focusing results indicate a very confusing situation where several peaks can be discriminated that could correspond to targets but it is hard to make a reliable decision.

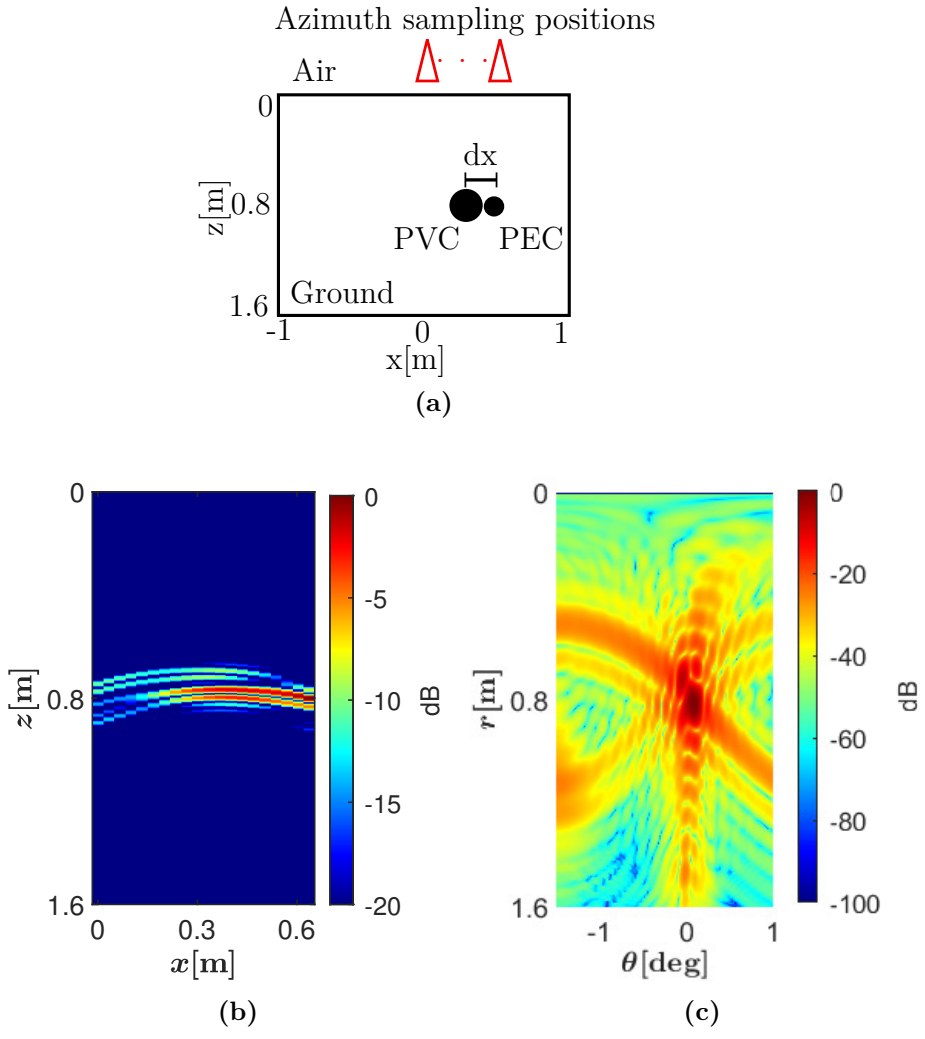

Figure 2.28: Scenario 1 with $dx = 120\ mm$ offset between 2 targets at the centre of the array and $N_a = 20$: (a) Setup configuration, (b) Range focused data and (c) BP focused results.

The second scenario results given in Fig. 2.29 indicate that it was impossible to see the two hyperbolas from the two heterogeneous targets in the range focused image as indicated in Fig. 2.29b. The corresponding BP focused results also could

not distinguish the two targets but instead due to poor resolution the two targets are interpreted as a single target.

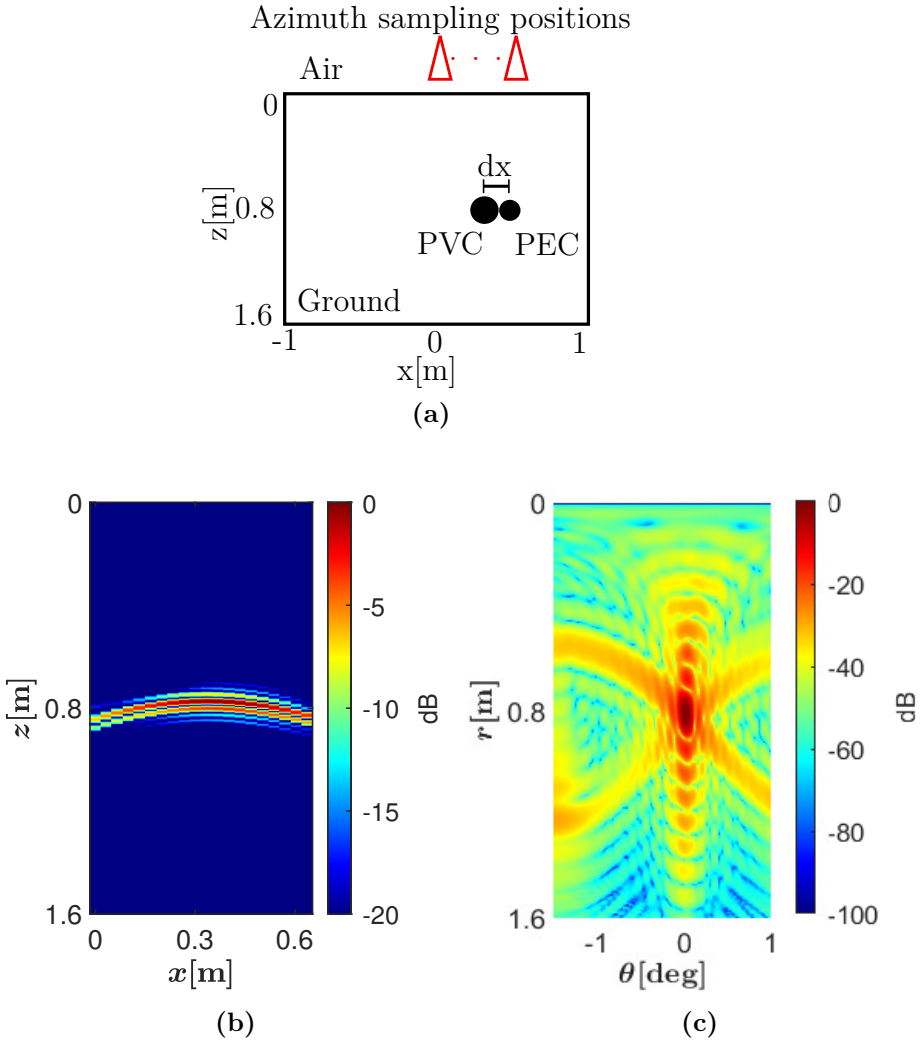

Figure 2.29: Scenario 2 with $dx = 70\ mm$ offset between 2 targets at the centre of the array and $N_a = 20$: (a) Setup configuration, (b) Range focused data and (c) BP focused results.

To improve resolution, spectral analysis techniques are implemented.

The results for scenario 1 ($dx = 120\ mm$) and scenario 2 ($dx = 70\ mm$) are presented in Fig. 2.30. We observe that, high resolution Specan methods except BF and CP are able to distinguish the two heterogeneous targets as shown in Fig. 2.30a and Fig. 2.30b for scenario 1 and scenario 2 respectively.

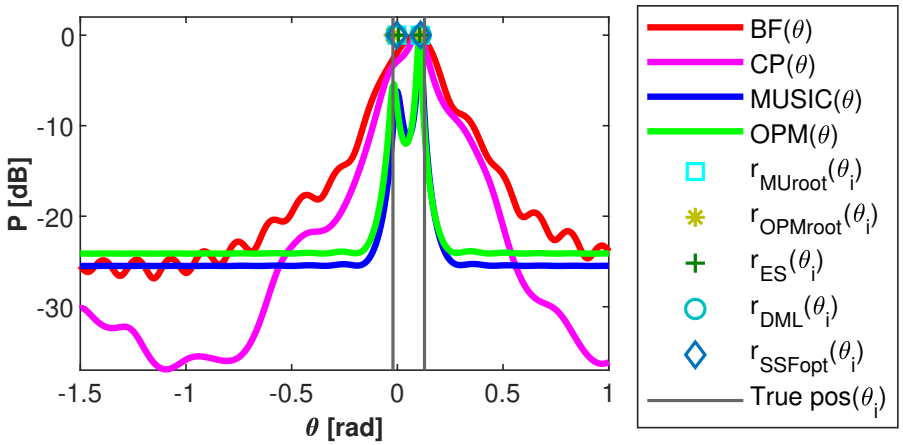

(a)

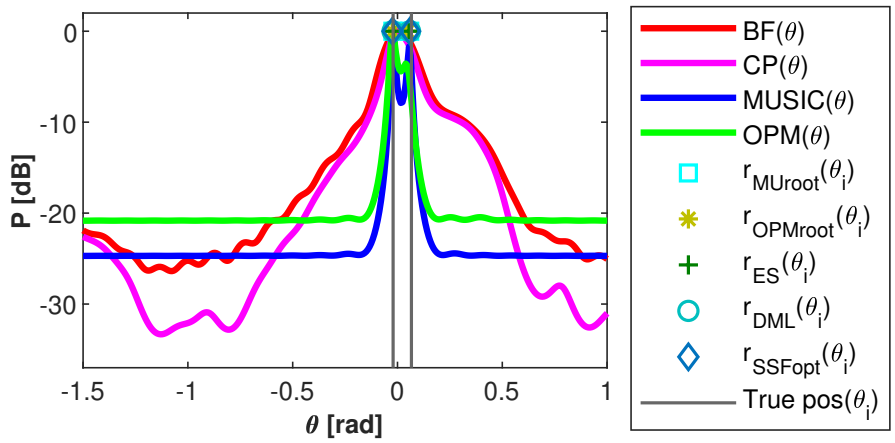

(b)

Figure 2.30: Specan objective function results for $N_a = 20$ with 2 targets at the centre of the array separated at: (a) $dx = 120\ mm$ (scenario 1) and (b) $dx = 70\ mm$ (scenario 2).

2.8 GPR Imaging using Specan within heterogeneous medium

In this section, target imaging is performed in the presence of clutter. The clutter in this study is simulated using a randomly distributed small spheres with different radii and different permittivity values whereas the target is a PEC cylinder (a cylinder will be a surface in 2D simulations).

2.8.1 Geometrical Configuration

The simulation conditions used in this case are similar to the one in subsection 2.2.2.2.

The target and clutter parameters are given in Table 2.5 whereby targets are PEC with a radius of 20 mm. The clutter is composed of spheres with different dielectric properties randomly sampled within the domain ε_r = [4 - 20] and different radii randomly selected in the domain [10 - 100] mm.

Table 2.5: Target and clutter parameters

Parameter	Distribution
Target radius	20 mm
Permittivity of target (ε_r)	PEC
Radius of clutter spheres	random selected within [10 - 100] mm
Permittivity of clutter spheres (ε_r)	random selected within [4 - 20]

Table 2.6: GPR scenarios

Scenario	Number of random spheres	Target position	N_a
1.a	0	$x_0 = 0.3015\ m$, $z_0 = 0.8\ m$	20
1.b	100	$x_0 = 0.3015\ m$, $z_0 = 0.8\ m$	20
2.a	0	$x_0 = 0.3015\ m$, $z_0 = 0.8\ m$	8
2.b	100	$x_0 = 0.3015\ m$, $z_0 = 0.8\ m$	8

The scenarios proposed to study the cluttered environment are given in Table 2.6. Scenario 1 corresponds to 20 azimuth sampling positions, with scenario 1.a simulating a single target in a homogeneous, clutter free medium as shown in Fig. 2.31a. Scenario 1.b simulating the same target in presence of clutter as indicated in Fig. 2.32a. Scenario 2 reduce the number of azimuth sampling positions to 8, whereby scenario 2.a simulate 1 target in homogeneous medium while scenario 2.b simulate a target in the medium with clutters.

2.8.2 Imaging results

The results of scenario 1.a are presented in Fig. 2.31.

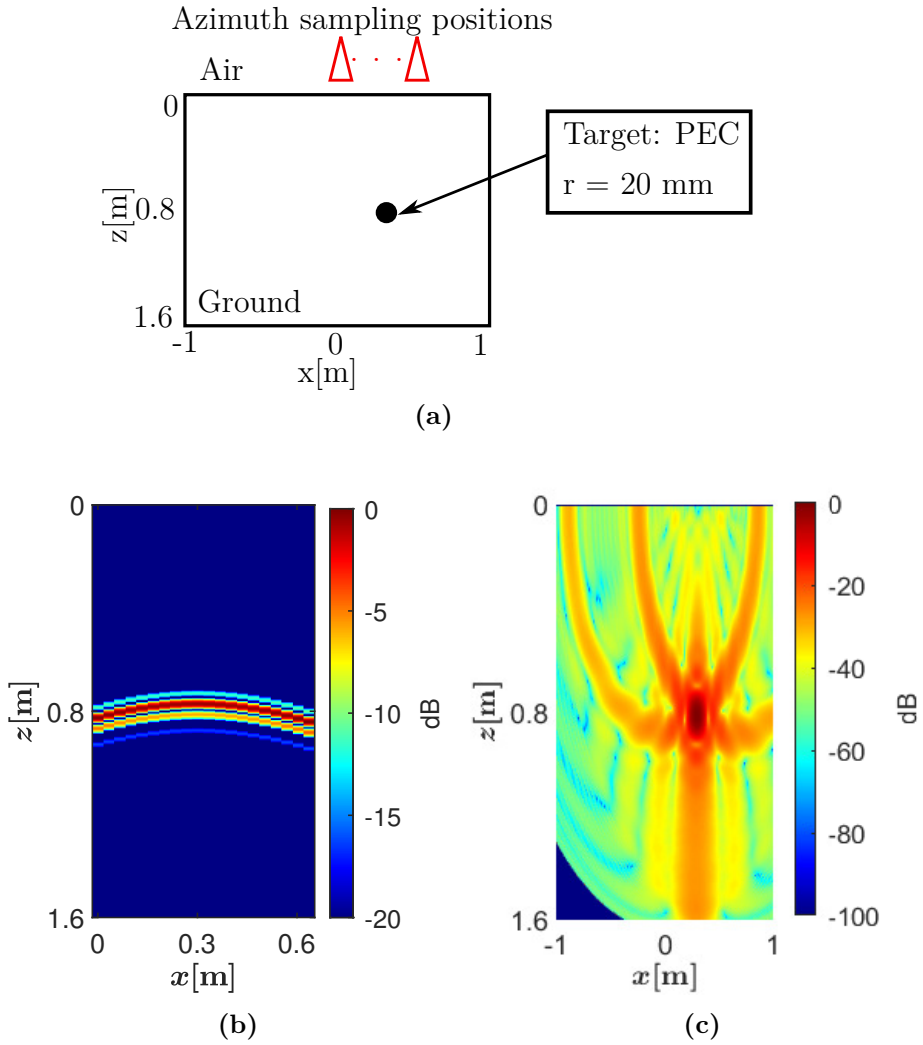

Figure 2.31: Scenario 1.a with 1 target at the centre of the array and $N_a = 20$: (a) Setup configuration, (b) Range focused data and (c) BP focused results.

Both the range focused and the 2D focused images in Fig. 2.32 show that the clutter response highly affects the imaging results and does not allow to perceive the presence of the PEC target in the middle. With this image it is impossible to identify the true position of the target.

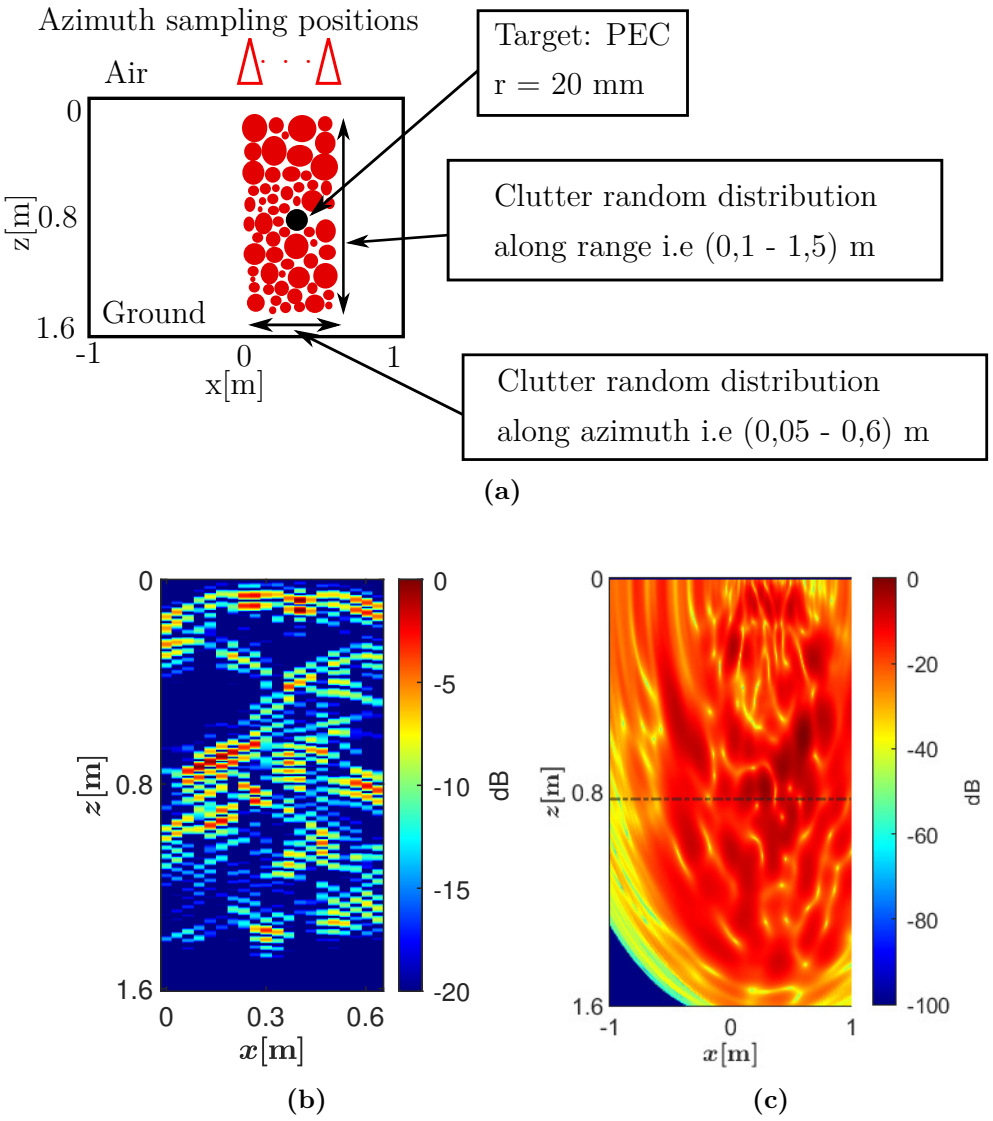

Figure 2.32: Scenario 1.b with 1 target at the centre of the array and $N_a = 20$ in a medium with 100 number sphere (a sphere will be a surface in 2D) clutter: (a) Setup configuration, (b) Range focused data and (c) BP focused results.

To estimate the true azimuth position of the targets, the proposed Specan are applied over the specific range location of the target and the results are given in Fig. 2.33.

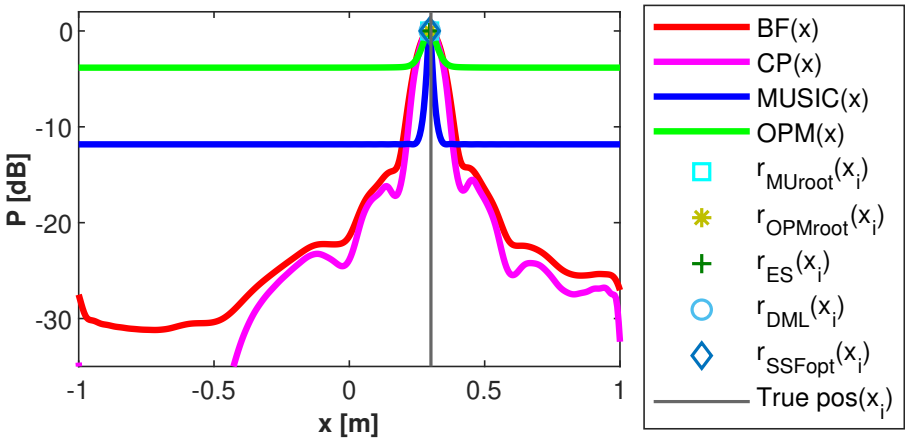

(a)

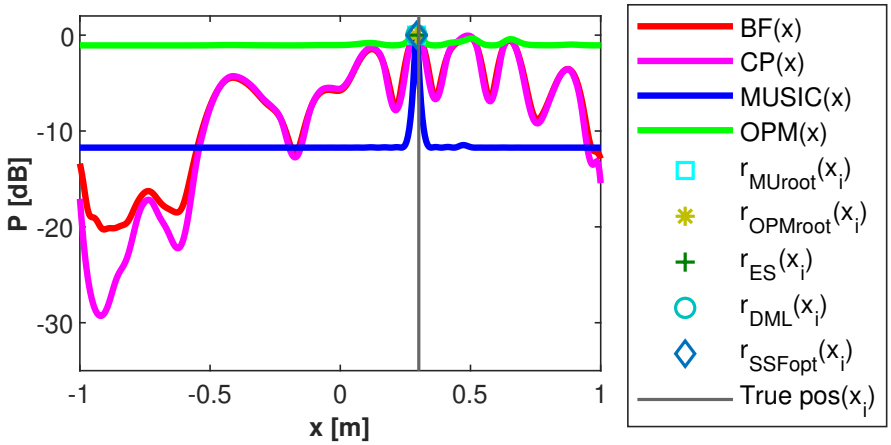

(b)

Figure 2.33: Specan objective function results for scenario using $N_a = 20$ with 1 target at the centre of the array: (a) In a medium without clutter (scenario 1.a) and (b) In a medium with 100 number of sphere (a sphere will be a surface in 2D) clutter (scenario 1.b).

By doing this it was possible to estimate the true position of the target as shown in Fig. 2.33b. This results indicate that high resolution techniques such as MUSIC are able to accurately localise the target in the azimuth direction while non parametric BF and CP techniques are strongly affected by the presence of clutter.

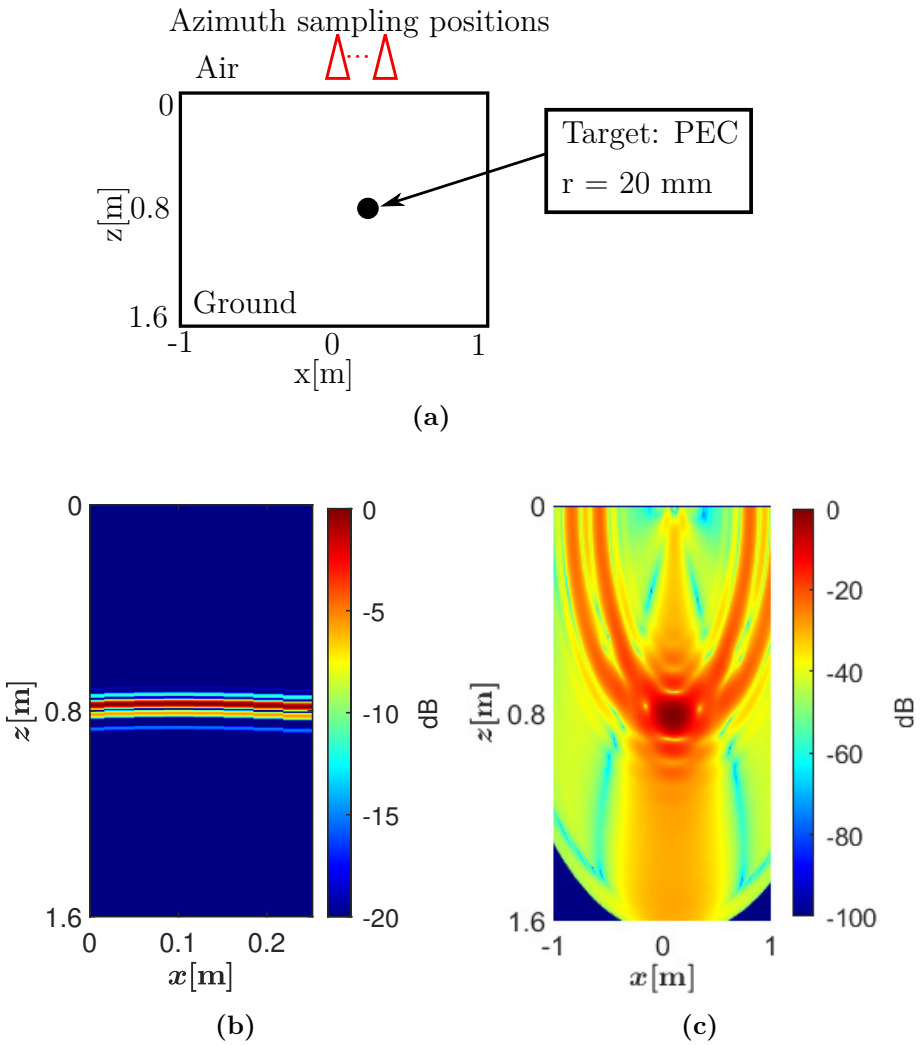

Figure 2.34: Scenario 2.a with 1 target at the centre of the array and $N_a = 8$:(a) Setup configuration, (b) Range focused data and (c) BP focused results.

Scenario 2 reduces the number of azimuth sampling positions to only 8. The results of range focused and BP focused for scenario 2.a are given in Fig. 2.34b and Fig. 2.34c respectively.

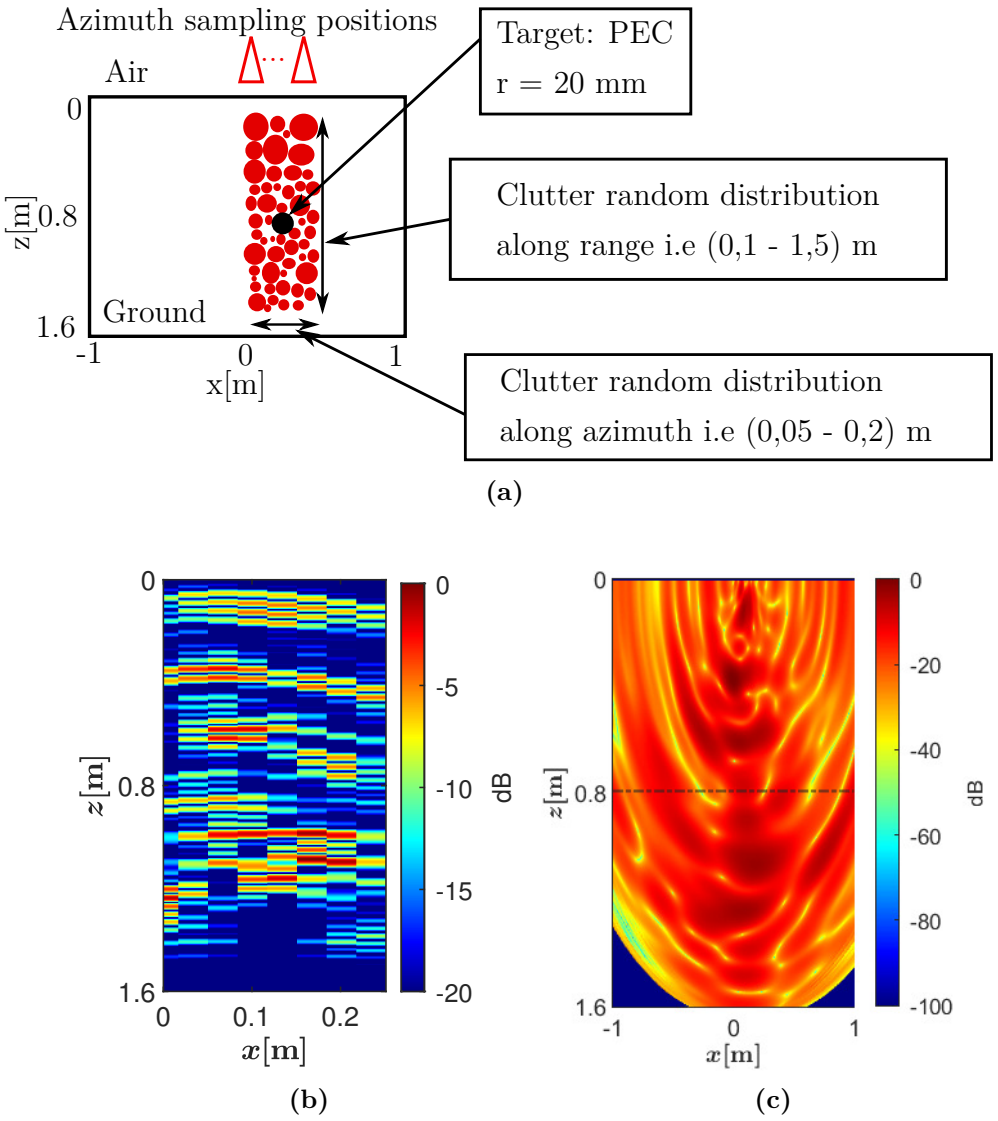

Figure 2.35: Scenario 2.b with 1 target at the centre of the array and $N_a = 8$ in a medium with 100 number of clutter: (a) Setup configuration, (b) Range focused data and (c) BP focused results.

Similarly to the previous case the clutter response strongly affect the image results and hence impossible to localise the targets as shown in Fig. 2.35b and Fig. 2.35c for scenario 2.b, hence Specan techniques are applied. The Specan techniques are able to localise the target in the presence of clutter as shown in Fig. 2.36b

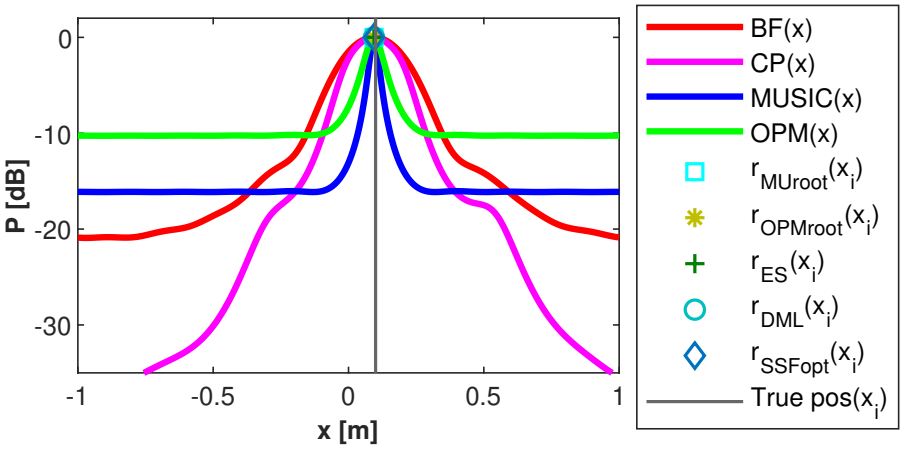

(a)

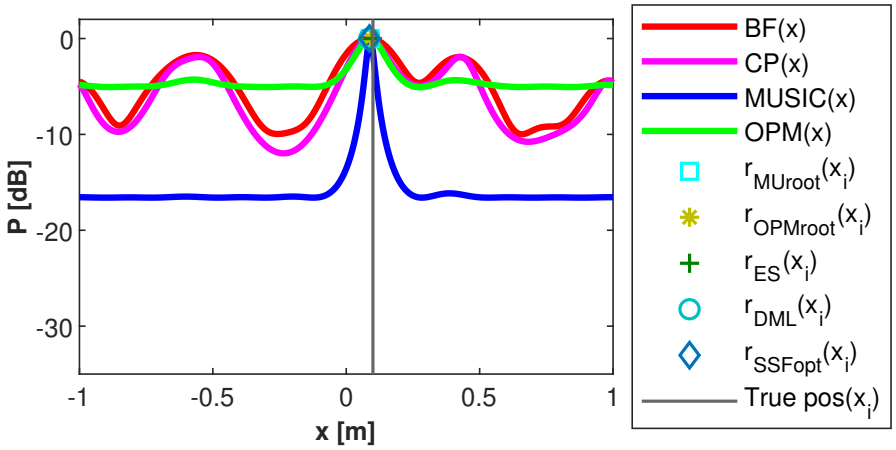

(b)

Figure 2.36: Specan objective function results for scenario using N_a with 2 targets at the centre of the array separated at: (a) $dx = 120\ mm$ (scenario 1) and (b) $dx = 70\ mm$ (scenario 2).

2.9 GPR Imaging using Specan on dispersive medium

Finally in this last section, Specan methods developed are applied in the case of dispersive host medium. The parameter of dispersive characteristic are elaborated using a one Debye relaxation scheme.

2.9.1 Geometrical Configuration

The simulation conditions used in this case are similar to the one in subsection 2.2.2.2. According to 1 Debye relaxation, the permittivity function versus frequency may be defined as:

$$\varepsilon_r(f) = \varepsilon_{r\infty} + \frac{\Delta\varepsilon_r}{1 + i2\pi f\tau}, \qquad \text{where} \quad \Delta\varepsilon_r = \varepsilon_{rs} - \varepsilon_{r\infty} \tag{2.12}$$

where by ε_{rs} is the zero frequency relative permittivity for given pole, $\varepsilon_{r\infty}$ is the relative permittivity at infinite frequency, τ is the relaxation time and f is the frequency

Table 2.7: Debye relaxation parameters

Parameter	Value
ε_{rs}	25.05
$\varepsilon_{r\infty}$	5.3
τ	300 ps
σ	0,003 S/m

The results in Fig. 2.37 shows the evolution of permittivity versus frequency over the bandwidth. We observe the impact of one Debye relaxation on the medium in which the permittivity varies significantly with respect to frequency along the bandwidth.

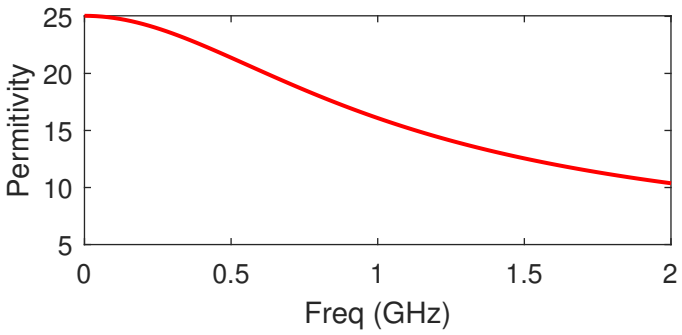

Figure 2.37: Permittivity function versus frequency.

Table 2.7 shows the simulated target parameter setup that is studied in this work concerning the imaging of targets embedded in a dispersive medium as

presented in Fig. 2.38a.

Table 2.8: Target setup parameters

Target parameter	Value
Permittivity of target	PEC
Radius of target	10 cm
Target position	$x_0 = 0.2\ m$, z_0=0.8 m, $dx = 4.75\ cm$

2.9.2 Imaging results

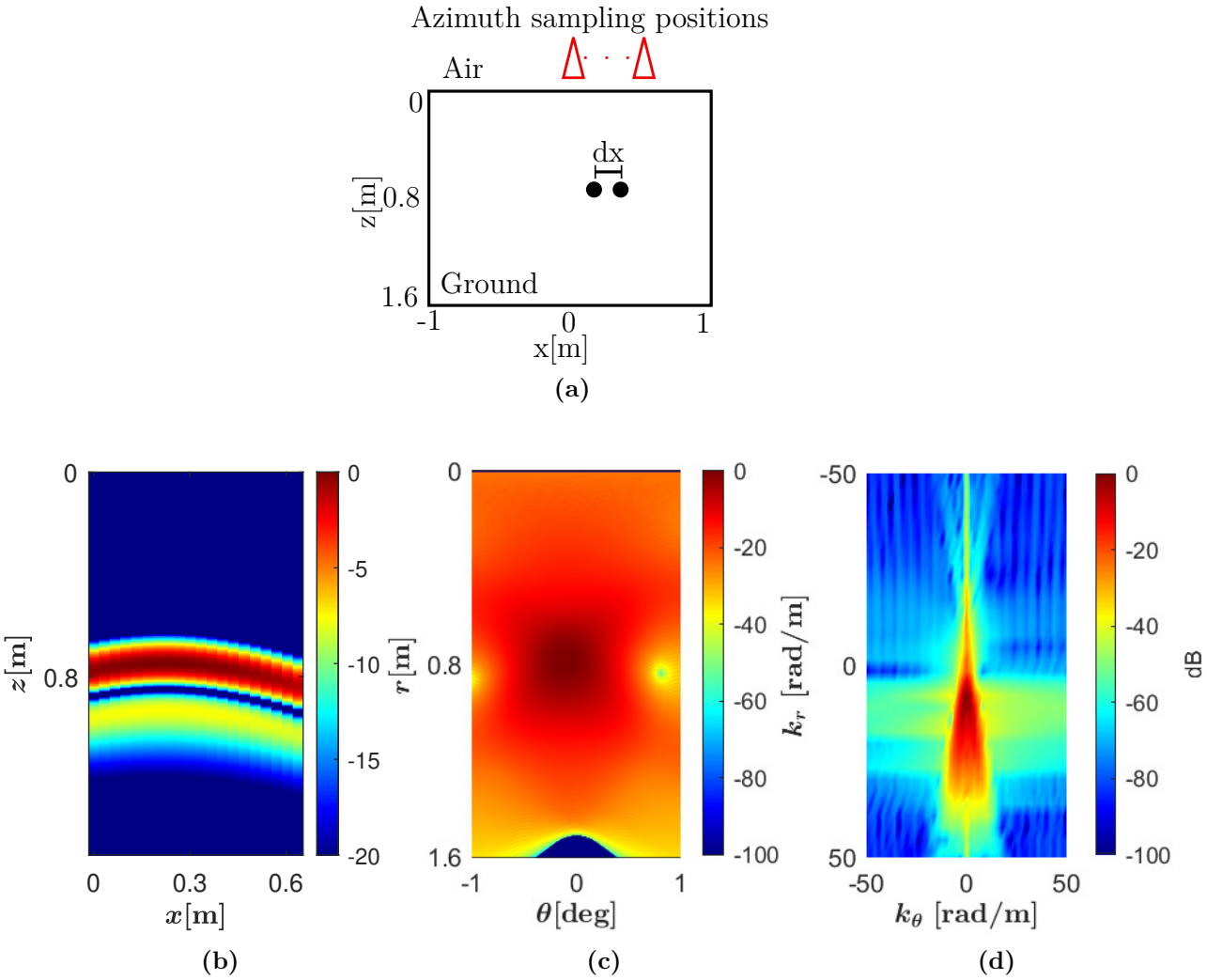

Figure 2.38: Dispersive medium scenario with $dx = 4.75\ cm$ offset between 2 targets and 20 azimuth sampling positions: (a) Setup configuration, (b) Range focused data (c) BP image and (c) BP image Spectrum.

Range focused results of hyperbola in dispersive medium is given in Fig. 2.38b.

The BP image and its spectrum shown in Fig. 2.38c and Fig. 2.38d indicate the strong defocusing due to the varying direct properties over the frequency domain covered by the measurement. This is due to the fact that the processing performed during BP does not corresponds anymore to a matched filter for received signal to the varying propagation conditions with frequency.

Specan methods are applied to improve azimuth resolution and the results are shown in Fig. 2.39. The results show that BP, CP and OPM methods were not able to separate the targets while the rest of the high resolution methods are able to distinguish two targets.

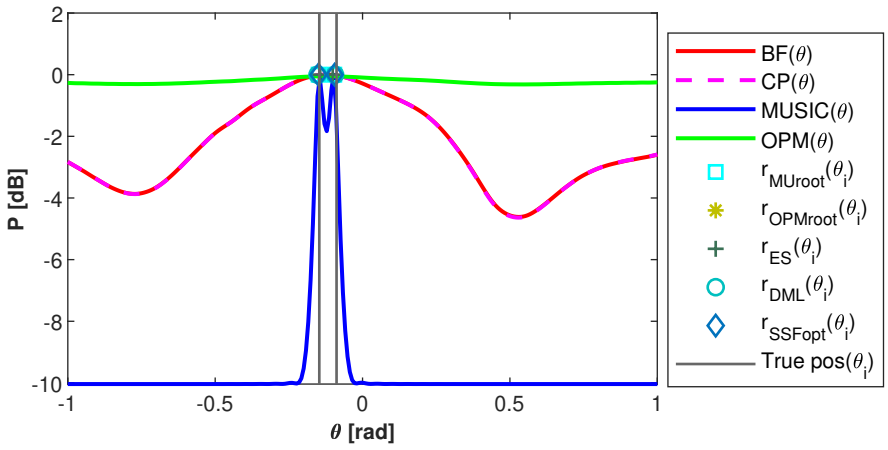

Figure 2.39: Specan objective function results for dispersive medium scenario using 20 azimuth sampling positions with 2 targets separated at $dx = 4.75\ cm$.

2.10 Conclusion

Spectral analysis techniques, usually based on narrow-band far field wave assumptions, have been adapted to near-field and broadband configurations for focusing GPR signals.

We have shown that Specan techniques have significant high resolution estimation capability along azimuth and range directions when compared to conventional methods which have resolution which is limited by Fourier azimuth and range resolution respectively. Two targets separated by less than the azimuth

resolution and range resolution are correctly distinguished by applying Specan techniques to the focused data where near field wide band effects have been compensated.

Also we have shown that, by using Specan techniques it is possible to reduce significantly the number of azimuth sampling positions while maintaining high estimation accuracy provided that the number of targets are less than the available number of elements.

On the other hand, detection of targets in heterogeneous environment which is more close to real life environment is studied. We showed that for heterogeneous targets, conventional methods had poor resolution when the azimuth offset between the targets is small, but thanks to high resolution focusing ability of Specan methods, it is possible to separate two heterogeneous targets with small azimuth offset.

Furthermore, detection of target in a environment with clutter with different dielectric properties and different sizes is studied. It is possible to estimate correct azimuth position of the target by Specan techniques when the specific range cell is selected.

Finally, GPR imaging using Specan methods is applied on dispersive and lossy medium. One Debye relaxation is used to simulate the medium dispersive property. We observed that BP could not separate two targets that were having the offset that was less than azimuth resolution. Hence Specan methods are used to improve resolution where by except BP, CP and OPM methods, other Specan are able to distinguish the two targets present in a dispersive medium environment.

So to conclude, we showed that, Specan methods may be useful to detect targets in a real life environment with high accuracy and resolution compared to conventional migration methods which have limitation of azimuth resolution which depend on the available number of azimuth sampling positions.

Chapter 3

Implementation of Spectral Analysis techniques on GPR Measured data

Contents

3.1 Introduction

This chapter applies the developed spectral analysis techniques to real GPR measurement.

The second section introduces the problem configuration and the measurement setup. In the third section, strengths and limitations of conventional migration techniques are illustrated on different scenarios considering different numbers of

antenna positions. The potential of Spectral analysis techniques for overcoming these limitation is then demonstrated. The fourth section studies the impact of irregular aperture sampling on the performance of the estimation. The fifth section analyses data acquired in the presence of clutter. Both migration techniques and Specan methods are implemented and compared.

3.2 Measurement setup

The measurement campaign was performed at CEA Leti Grenoble in a sand box of dimension $3 \times 2.864 \times 1.3\ m^3\ xyz$. The setup scenario is presented in Fig. 3.1 for inside view and Fig. 3.2 for outside view .

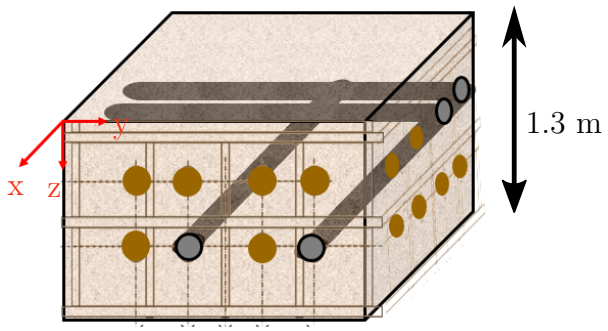

Figure 3.1: Setup scenario for measurement data : inside view.

The sand inside the box was estimated to have permittivity of $\varepsilon_r = 5$. The frequency response between the two antennas is measured using a Vector Network Analyser (VNA) using 401 frequency points uniformly distributed between 100 MHz and 2.1 GHz. The transmitted power is 10 dBm and the intermediate frequency (IF) is set to 100 Hz

As illustrated in Fig. 3.2, the VNA is connected to a PC which controls the gantry axis controller with a program developed in Matlab. The antennas are mounted on the gantry using a mechanical support and are connected via a VNA which is controlled by a PC giving the position of the antennas set by a controller connected to the gantry. The alignment of the gantry with the pipes is achieved using a laser. The elevation of the antennas from the sand is around $1,5 - 2,5$ cm.

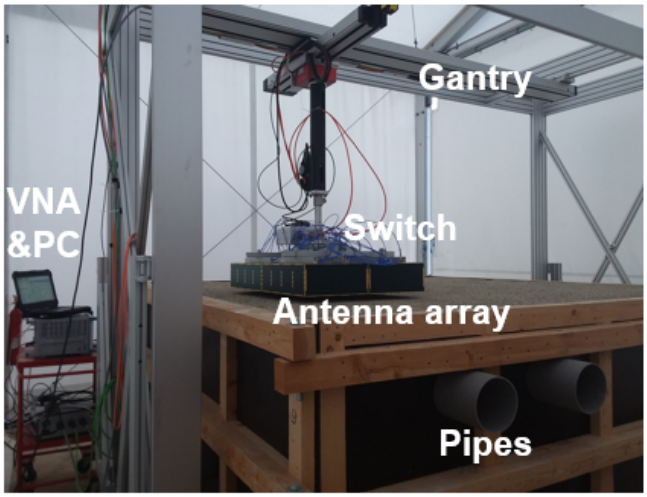

Figure 3.2: Setup scenario for data acquisition measurement data : outside view.

Table 3.1: Targets considered in this study

Parameter	Pipe 1	Pipe 2
Type	empty PVC	empty PVC
Radius	10 cm	10 cm
Thickness	0.3 cm	0.3 cm
Length	350 cm	350 cm
Orientation of cylinder axis	y	y

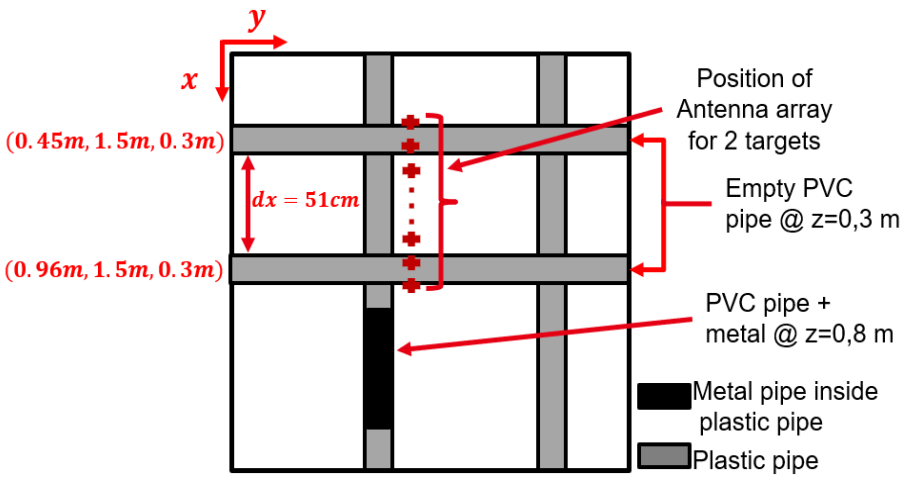

Figure 3.3: Measurement scene description.

The targets considered in this case study are plastic pipes filled with air at a depth of 0.3 m as indicated in Table 3.1 and in Fig. 3.3 where by the black segment represents the location of the metal pipe inside the PVC pipe. The acquisition are performed using an array of Bow-tie antennas with scanning step of 50 mm, hence resulting into 35 azimuth sampling positions. Fig. 3.3 shows in red the position of the antenna array used for Bscan range.

3.3 ULA GPR data analysis

In this experiment the data were acquired with regular spacing along a linear scan in azimuth corresponding to Uniform Linear Array (ULA) conditions.

3.3.1 GPR scenarios

Table 3.2 describes the three scenarios analysed from the experiment.

Table 3.2: GPR scenario Case 3: Measurement data

Scenario	x_0	z_0	dx	N_a
1 (2 targets)	0.45 m	0.3 m	51 cm	35
2 (2 targets)	0.45 m	0.3 m	51 cm	7
3 (2 targets)	0.45 m	0.3 m	51 cm	3

Scenario 1 considers a full antenna array with 35 azimuth sampling positions, whereas scenario 2 uses a portion of antenna array with only 7 sampling positions selected at the centre of the scene. Finally, scenario 3 takes into account only 3 azimuth sampling positions also taken at the centre of a scene.

3.3.2 Results

Fig. 3.4 shows the results for scenario 1. Over the range focused image one may observe the ground coupling response at the top followed by the PVC pipes with hyperbolas whose apex is located at the depth 0.3 m. The PVC pipe with metal inside is observed at 0.8 m. Lastly we observe an aluminium plate at 1.3 m which is at the bottom of the sand box for calibration purposes.

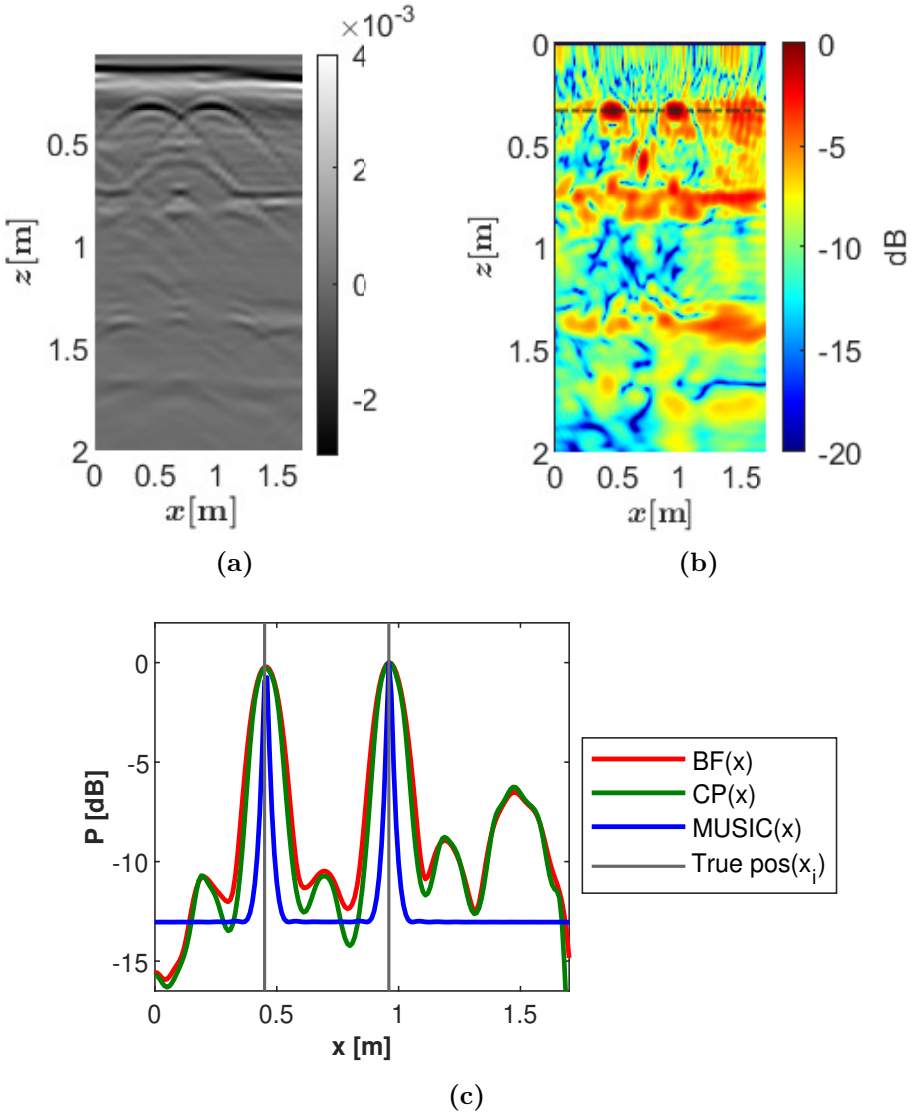

Figure 3.4: Focusing results using $N_a = 35$: (a) Range focused data, (b) 2D focused BP results, (c) Specan objective functions at z=0.3m.

The corresponding 2D focused image is given in Fig. 3.4b which shows the ability of BP to detect the two targets at 0.3 m while at 0.8 m the PVC pipe with the metal may observed along with the aluminium plate at 1.3 m. Fig. 3.4c shows the Specan analysis results in which both targets are clearly detected and well localised.

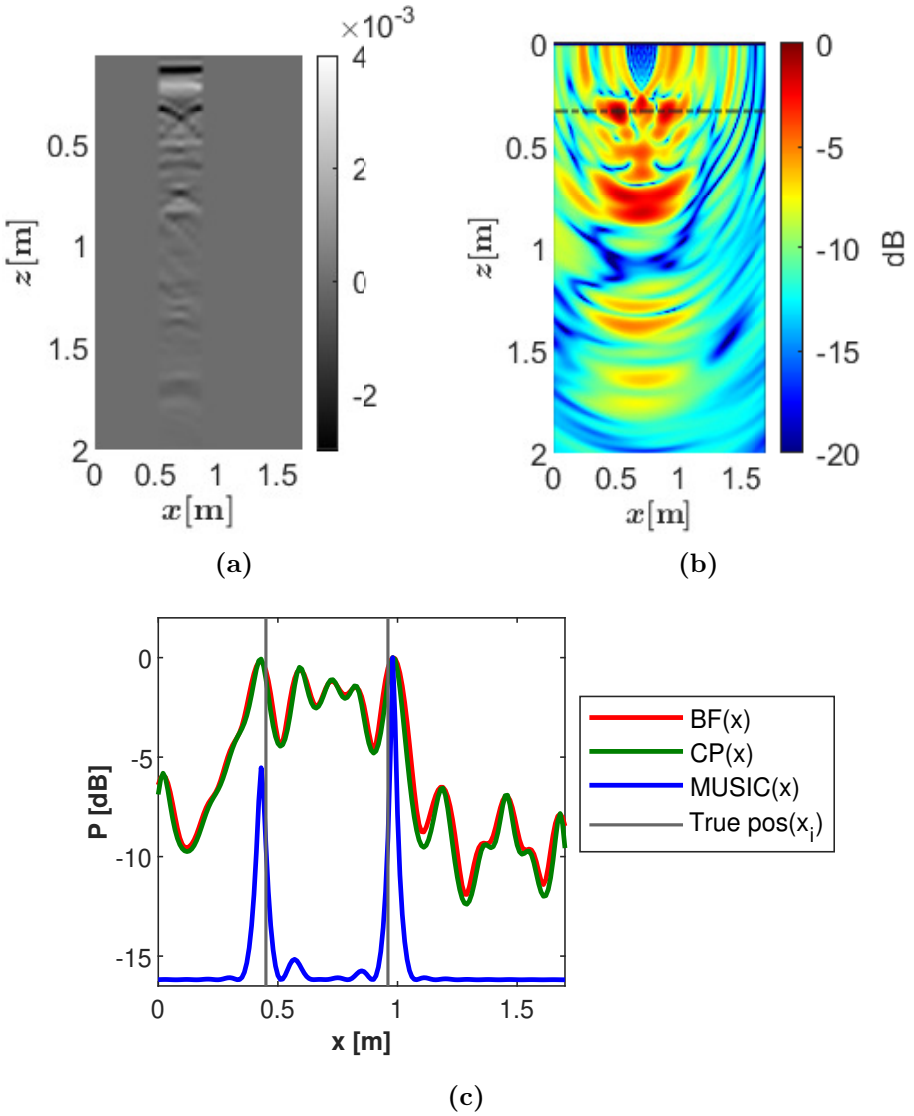

Figure 3.5: Focusing results using $N_a = 7$: (a) Range focused data, (b) 2D focused BP results, (c) Specan objective functions at z=0.3m.

The results for the scenario that considered part of the antenna array, i.e 7 azimuth sampling positions are given in Fig. 3.5. Here only a small portion of hyperbolas of the two targets at $z = 0.3\ m$ can be seen as shown in Fig. 3.5a. And we observe in Fig. 3.5b that BP was able to resolve the two targets but with poor image quality due the to reduced aperture length.

On the other hand, thanks to the high resolution focusing ability of Specan

methods as indicated in Fig. 3.5c, it is possible to reduce the level of side lobes and to clearly distinguish the presence of both targets especially with high resolution techniques results.

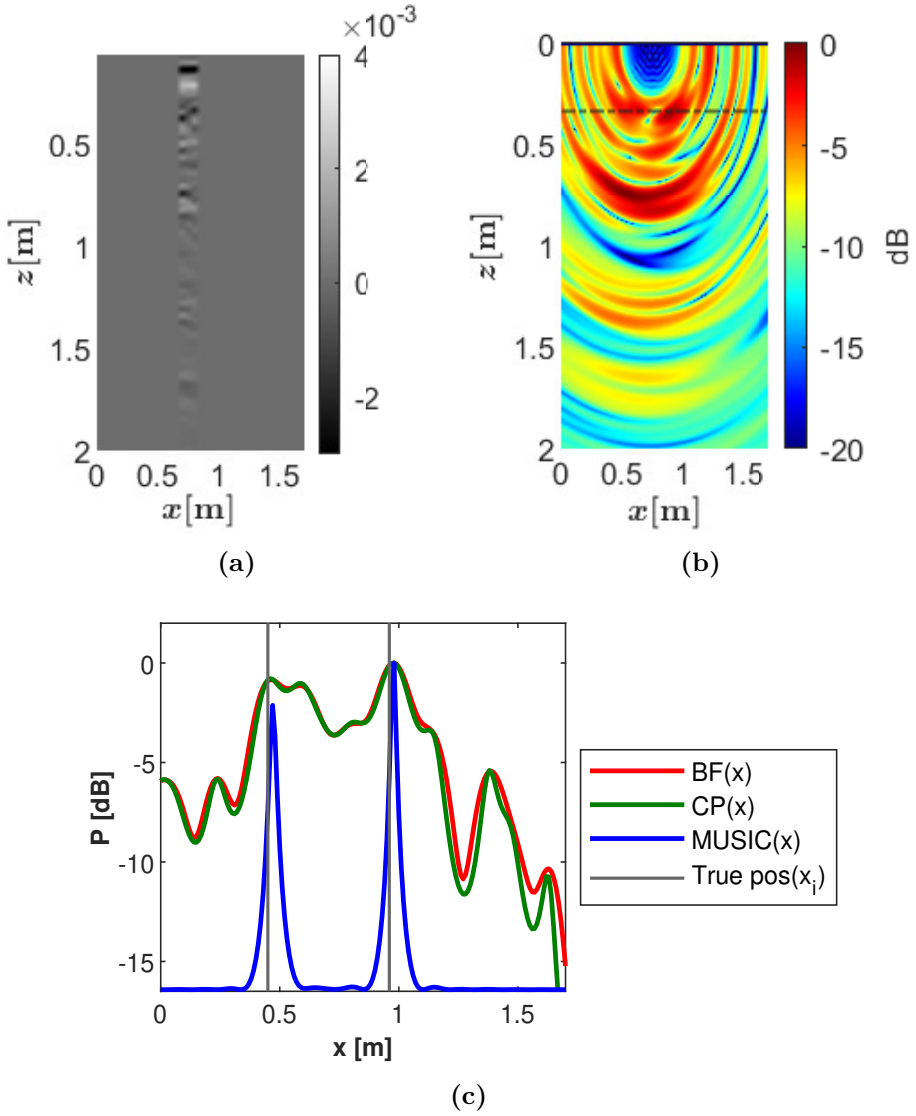

Figure 3.6: Focusing results using $N_a = 3$: (a) Range focused data, (b) 2D focused BP results, (c) Specan objective functions at z=0.3m.

For the final configuration, only 3 azimuth sampling positions are considered and the corresponding measurements are given in Fig. 3.6. The range focused data image is given in Fig. 3.6a where, the hyperbolas can not be observed.

The corresponding BP focused image has a poor resolution as seen in Fig. 3.6b. Specan methods are applied and the results shown in Fig. 3.6c clearly indicate that the both targets can be resolved when using high resolution techniques.

As previously stated, estimating the actual backscattered intensity using high resolution techniques requires to implement an additional estimation step which can be performing using Least Square estimation [SM+05].

Moreover, as non-parametric techniques BP and CP can be applied without specifying the number of targets. One may use them to construct a continuous image by applying them at arbitrary depth as presented in Fig. 3.7.

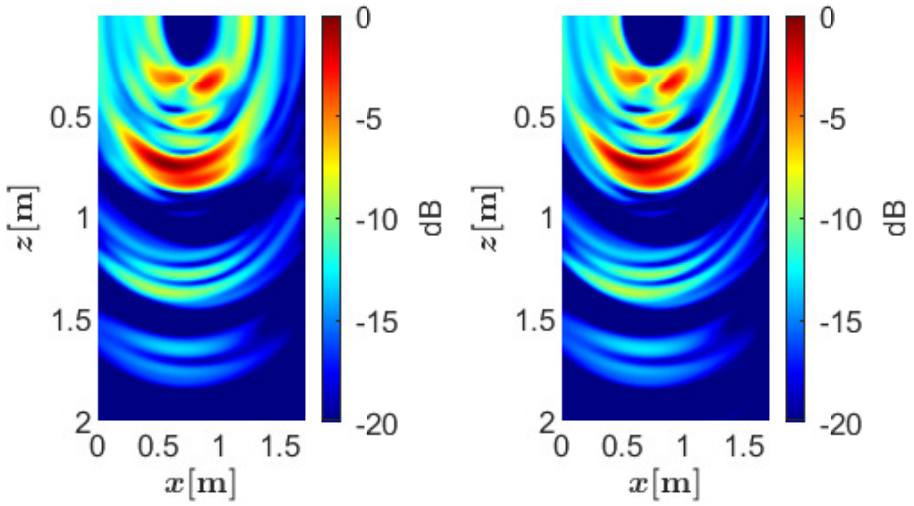

Figure 3.7: Focusing results using 3 antennas: (a) BF image, (b) CP image.

Noise was added to the final configuration with only 3 number of azimuth sampling positions before applying the Specan methods, with a SNR of -20 dB with 100 noise realisations. The Specan results are presented in Fig. 3.8. We observe that BF and CP resolution degrade with presence of noise when compared to noiseless scenario in Fig. 3.6c. But with high resolution methods like SSF, when noise floor is low enough it is still able to estimate the targets in noise environment.

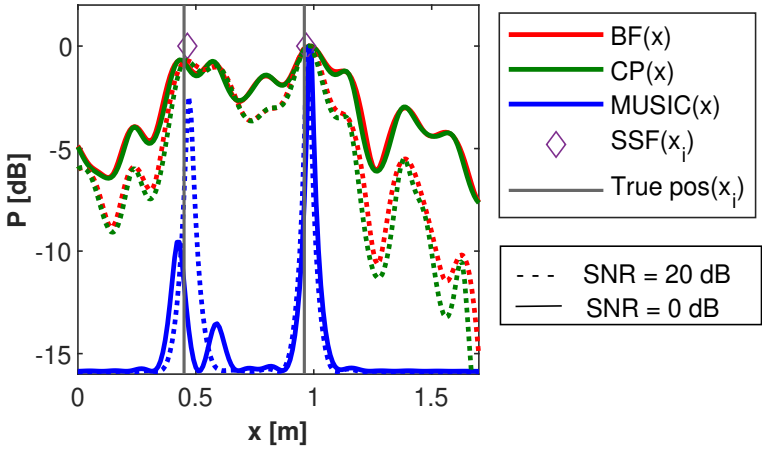

Figure 3.8: Focusing results using 3 antennas: Specan objective functions at z=0.3m with noise SNR = 0 dB (i.e for BF, CP, MUSIC, and SSF) and noise SNR = 20 dB (i.e for BF, CP and MUSIC).

3.4 Analysis of non ULA GPR data

In this section, we study the impact of irregular azimuth sampling for a given synthetic aperture length.

3.4.1 GPR scenarios

Table 3.3: GPR scenario Case 3: Data acquisition conditions

Scenario	Size of synthetic aperture	Number of azimuth sampling positions	Azimuth sampling
4.a	1.7 m	35	Regular
4.b	1.7 m	10	Irregular
5.a	1 m	21	Regular
5.b	1 m	6	Irregular
6.a	0.55 m	12	Regular
6.b	0.55 m	4	Irregular

Tab. 3.3 and Fig. 3.9 introduce the scenario that is used to study the impact of irregular azimuth sampling on a given synthetic aperture lengths based on the measurement data described in section. 3.2.

Scenario 4.a consider a complate synthetic aperture i.e 1.7 m with regular azimuth sampling and 35 antenna positions, whereas scenario 4.b keep the same aperture and instead take into account irregular azimuth sampling positions with 10 antenna positions.

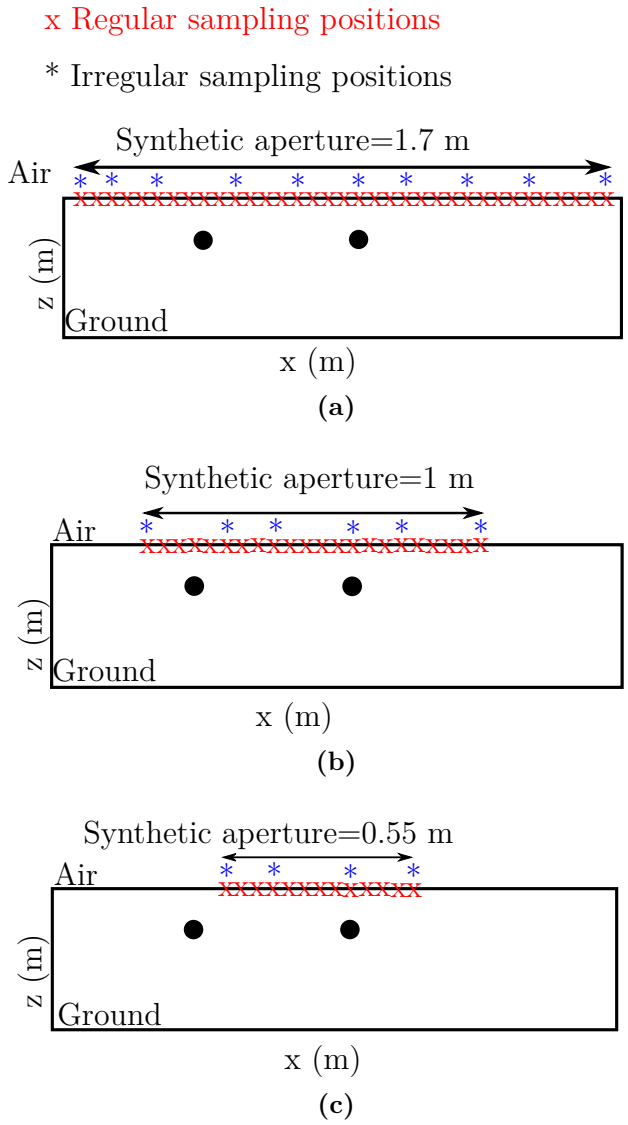

Figure 3.9: Azimuth sampling description setup: (a) Scenario 4, (b) Scenario 5 and (c) Scenario 6

Scenario 5.a reduced the synthetic aperture to 1 m with 21 regular azimuth positions, whereas scenario 5.b uses 6 irregular sampled azimuth positions.

The last scenario 6.a reduces the synthetic aperture even further i.e 0.55 m, with 12 azimuth sampling positions in the regular case and 4 positions in the irregular configurations as presented in Fig. 3.9.

3.4.2 Irregular azimuth sampled data results

First of all, the results of scenario 4 which considered synthetic aperture of 1.7 m are given in Fig. 3.10.

The BP focusing results of uniform azimuth sampled measurement data that used 35 antenna positions are given in Fig. 3.10a (scenario 4.a). This BP image have better resolution when compared to the results of irregular azimuth sampled data in Fig. 3.10b (scenario 4.b) which used 10 antenna position.

The resolution of BP focused results for the case of irregular sampled data degraded gradually in spite of the fact that both scenario 4.a and 4.b had the same synthetic aperture.

To improve resolution, Specan methods were applied to the scenario 4.b that involved irregular azimuth sampling and result are given in Fig. 3.10c.

The results shows that, spectral analysis techniques are able to distinguish both targets in the scenario with MUSIC having high resolution compared to BF and CP. Therefore in comparison to Fig. 3.10b, Specan techniques are able to successfully identify the targets with better resolution at given depth $z = 0.3\ m$.

The obtain Specan results in Fig. 3.10c implies that, classical GPR focusing methods have resolution limitation depending on the number of azimuth samples considered, thanks to high resolution capability of Specan methods it is possible to overcome this resolution limitation and successfully detect and localise the targets present in the scene.

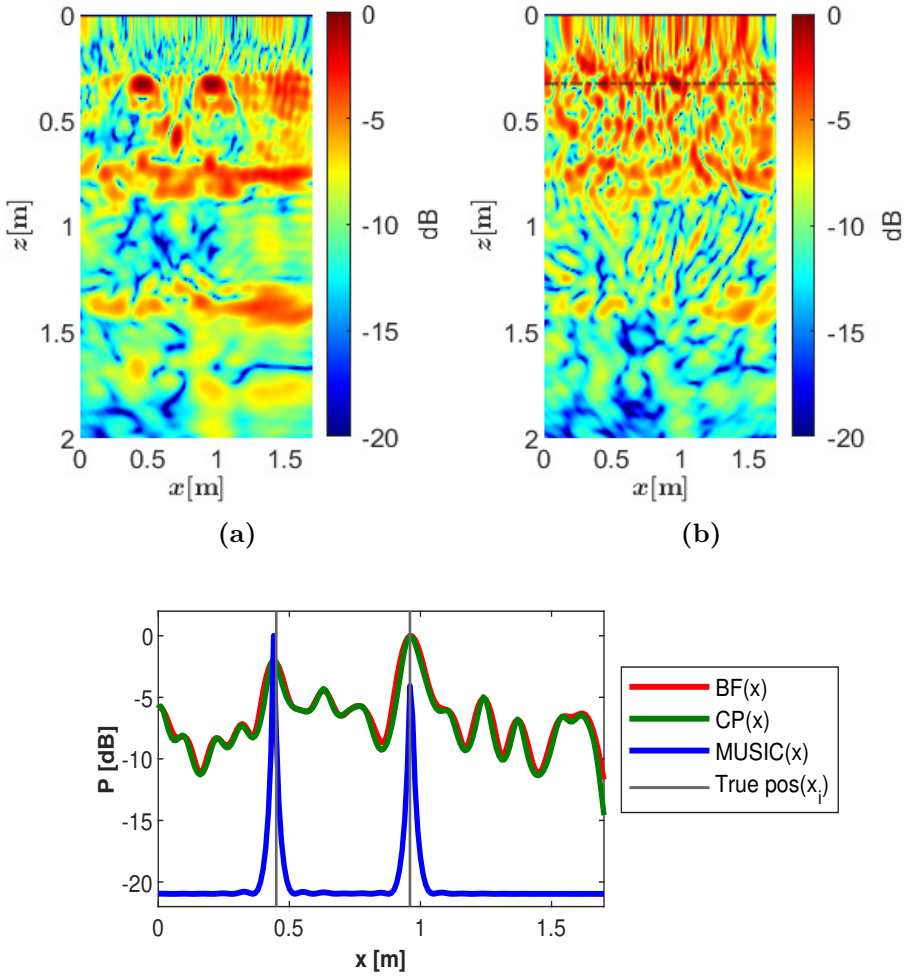

Figure 3.10: Scenario 4 having 1.7 m size of synthetic aperture: (a) BP results of regular sampled data with 35 number of azimuth sampling positions (scenario 4.a), (b) BP results of irregular sampled data with 10 number of azimuth sampling positions (scenario 4.b), (c) Specan objective function for irregular sampled data with 10 number of azimuth sampling positions (scenario 4.b).

Secondly, the results for case 5 that took into account synthetic aperture of 1 m are given in Fig. 3.11. The regular azimuth sampled BP focusing results that used 21 number of azimuth sampling positions is given in Fig. 3.11a where the BP focusing results of irregular azimuth sampling data which had 6 number

of azimuth sampling positions are indicated in Fig. 3.11b. Again, BP results of irregular sampling data (scenario 5.b) are poor compared to regular azimuth sampled data (scenario 5.a). To improve resolution of irregular sampled data scenario, Specan techniques were applied and results are shown in Fig. 3.11c. All the Specan methods were able to distinguish the two targets in the scene.

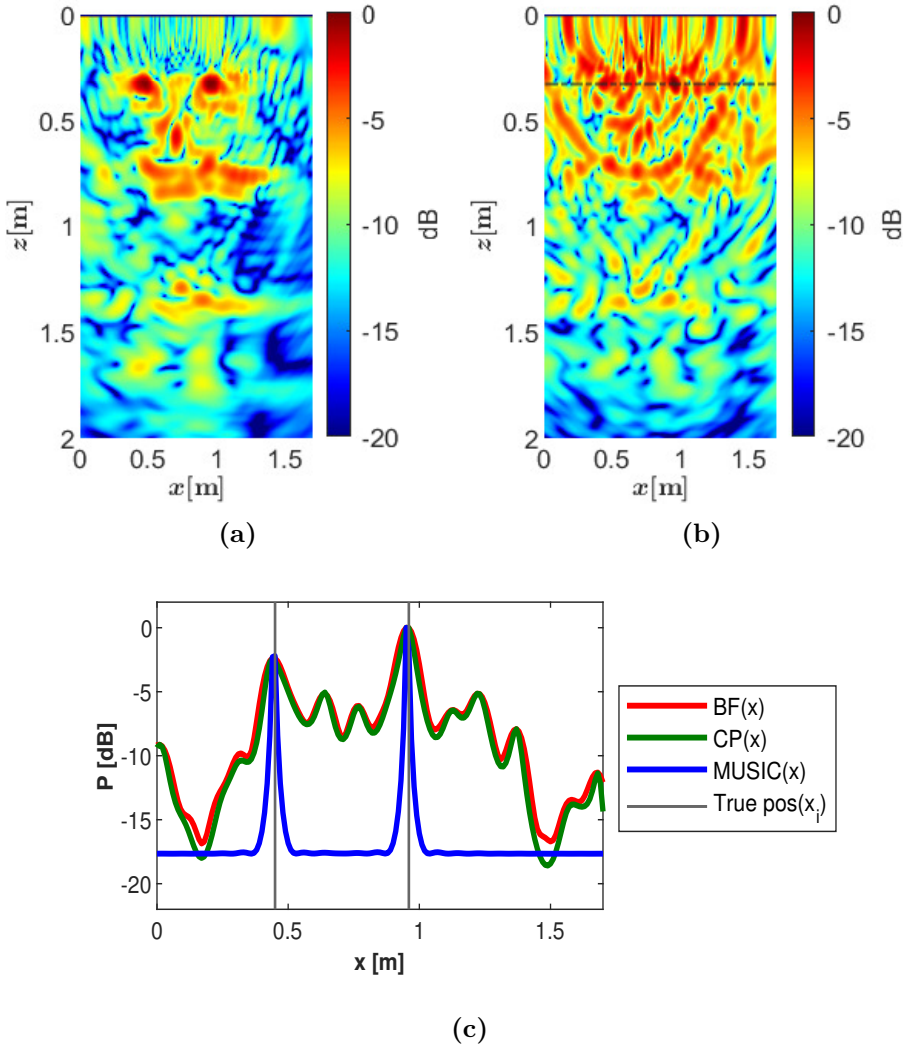

Figure 3.11: Scenario 5 having 1.0 m size of synthetic aperture: (a) BP results of regular sampled data with 21 number of azimuth sampling positions (scenario 5.a), (b) BP results of irregular sampled data with 6 number of azimuth sampling positions (scenario 5.b), (c) Specan objective function for irregular sampled data with 6 number of azimuth sampling positions (scenario 5.b).

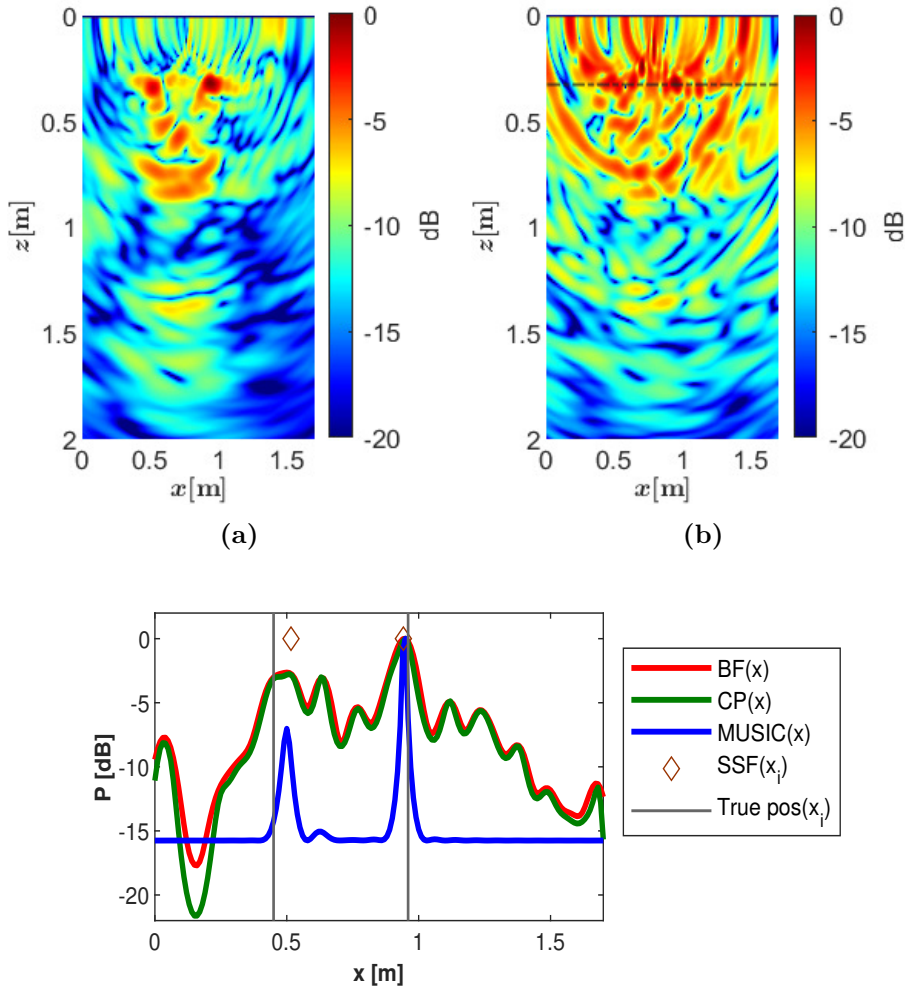

Figure 3.12: Scenario 6 having 0.55 m size of synthetic aperture: (a) BP results of regular sampled data with 12 antenna positions (scenario 6.a), (b) BP results of irregular sampled data with 4 number of azimuth sampling positions (scenario 6.b), (c) Specan objective function for irregular sampled data with 4 number of azimuth sampling positions (scenario 6.b).

Finally, the results of last scenario that considered 0.55 m size of synthetic aperture are given in Fig. 3.12.

Like in the previous cases, BP results of irregular azimuth sampled data that used only 4 number of azimuth sampling positions has poor resolution image as shown in Fig. 3.12b compared to BP results with regular azimuth samples

which had 12 number of azimuth sampling positions as illustrated in Fig. 3.12a. Again Specan methods were applied to the case with poor resolution i.e irregular azimuth sampled data with 4 number of azimuth sampling positions and results are presented in Fig. 3.12c. High resolution technique i.e MUSIC had better resolution compared to BF and CP, due to the fact that the performance of later depends on the number of samples available for covariance matrix data estimation.

3.5 Measurement performed through a diffused layer of clutter

3.5.1 Geometrical Configuration

The measurement were conducted with 8 antennas separated with distance of 12.70 cm. The medium was estimated to have permittivity of $\varepsilon_r = 5$. The measurement bandwidth was from 200 MHz to 1.6 GHz.

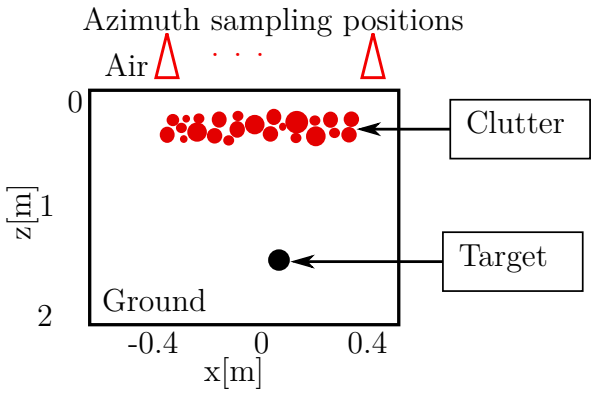

Figure 3.13: Setup configuration for scenario with 1 target and 8 number of azimuth sampling positions.

The setup scenario for the clutter medium scenario is presented in Fig. 3.13. The the target is positioned at $x = 0.02\ m$ and $z = 1.4\ m$ while the clutters are present around $z = 0.2\ m$ and $z = 0.3\ m$.

3.5.2 Imaging results

The obtained results of GPR measurement data in presence of clutter are presented in Fig. 3.14.

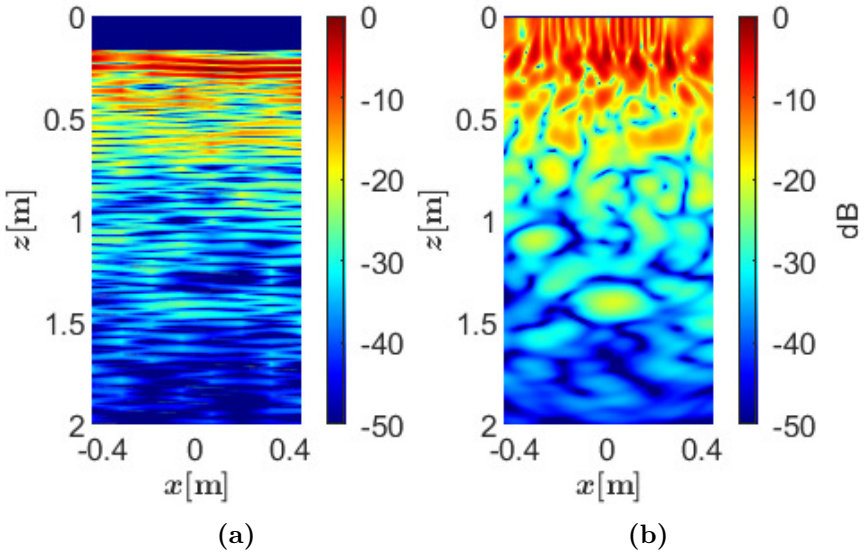

Figure 3.14: Measurement data with clutter medium: (a) Range focused measurement data and (b) BP focused results.

The range focused image is given in Fig. 3.14a in which the presence of clutters is observed around $z = 0.2\ m$ and $z = 0.3\ m$. And from the image is difficult to observe the presence of target in the scenario.

Fig. 3.14b shows the corresponding focused image with BP focusing method. Again with these results it was difficult to tell the number of targets present in the scenario.

So Specan methods will be applied to improve resolution first along azimuth then along range directions.

3.5.2.1 Simulation results on azimuth position

To improve resolution along azimuth direction, the Specan methods were applied to selected the range cell as indicated in Fig. 3.15a. The obtained results are presented in Fig. 3.15b.

The results shows that all the Specan methods were able to detect the target present in the scene along with estimating the target at correct azimuth position i.e $x = 0.02\ m$.

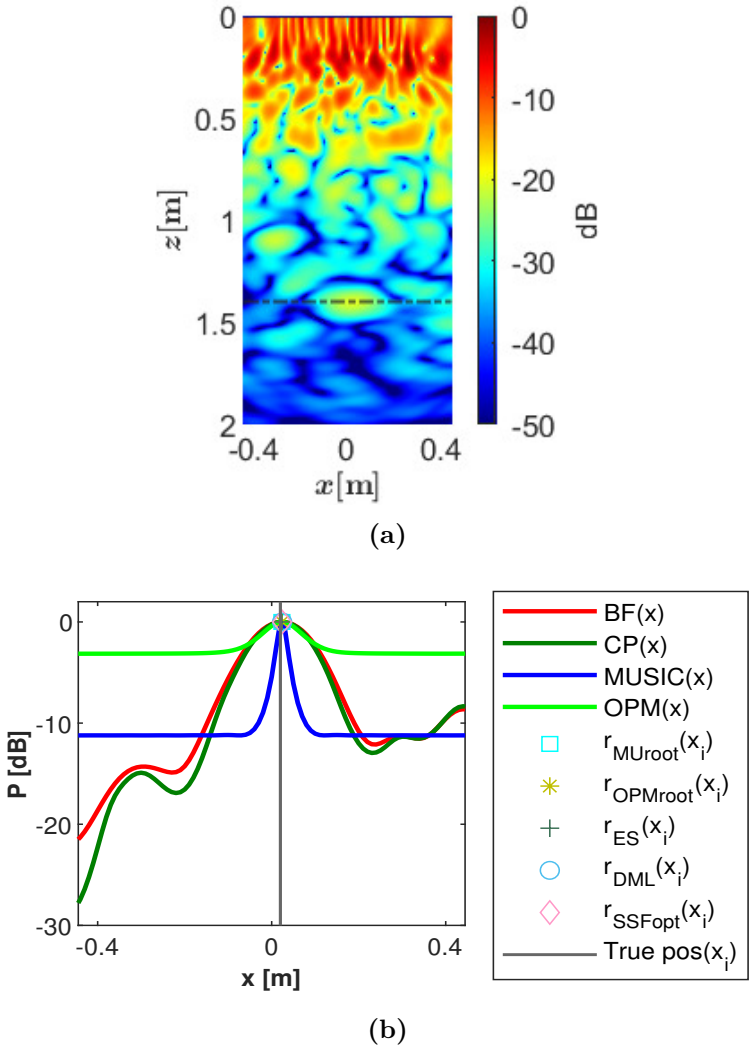

Figure 3.15: Measurement data with clutter medium: (a) BP focused results and (b) Specan objective functions.

3.5.2.2 Simulation results on range position

To improve resolution along range direction, the Specan methods are applied along azimuth cell as shown in Fig. 3.16b.

The azimuth cell was selected from the BP focused image by taking into account only the zone around which the target was detected by focusing BP method. By doing so, the Specan methods were all able to detect the true range position of the target which was $z = 1.4\ m$

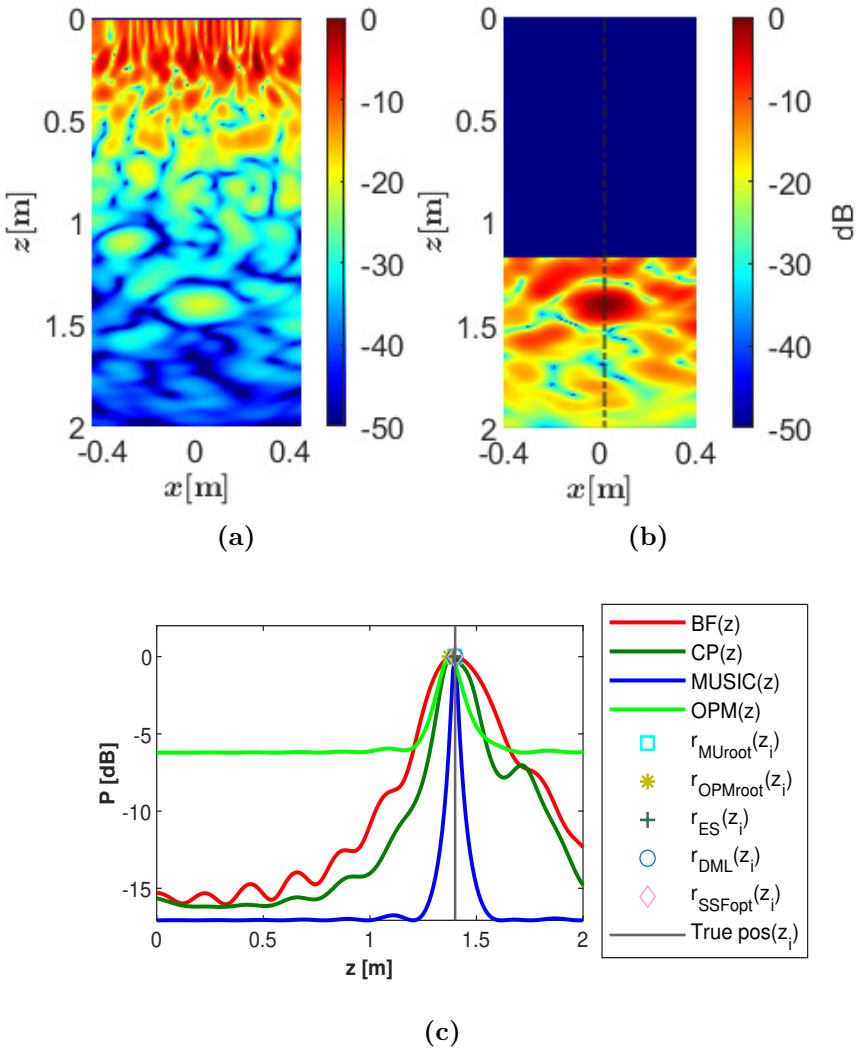

Figure 3.16: Measurement data with clutter medium: (a) BP focused data, (b) BP focused results, (c) Specan objective functions.

3.6 Conclusion

Spectral analysis methods developed in this work were tested in real life environment i.e on GPR measurement data We have shown that Specan techniques have significant high resolution estimation capability along azimuth directions when compared to conventional methods which have resolution which is limited by Fourier azimuth resolution. In addition to that, we have shown that, for a given fixed size synthetic aperture, when the data are collected with irregular

azimuth samples, the performance of classical migration techniques degrade gradually. The focused images have poor resolution hence it is difficult to separate the available targets in the scene. To improve resolution, this work proposed to use Spectral analysis techniques which were able to distinguish the targets in the irregular azimuth sampled data even with the case where only few number of azimuth sampling positions (i.e only 4 number of azimuth sampling positions were available). Finally we have shown that Specan methods may be used to estimate the target position in a cluttered medium environment on both azimuth and range positions.

Chapter 4

Conclusions & Perspectives

Contents

4.1 Introduction

In this research, the general basics of GPR was studied along with various GPR configuration. Propagation modelling of GPR scenarios was done using was FDTD free software (gprMax) which was validated by conducting quantitative comparison with theory based model developed at CEA.

Since raw GPR image shows up as an hyperbola, the focusing (migration) techniques were required to focus the hyperbola to the true target position. The traditional migration algorithms which were studied in this thesis include: Hyperbolic summation, Phase shift, FK migration and Back projection method. These algorithms were implemented by using data simulated by gprMax. The results showed limitation of these classical methods when the offset between targets were less than azimuth or range resolution. This is due to the fact that, two targets were interpreted as single targets due to poor resolution of conventional migration techniques which is limited by the bandwidth and the number of antennas (synthetic aperture).

We also observed that, in most GPR configurations, azimuth resolution is always poor compared to range resolution. Therefore, this research focused on improving the azimuth resolution by applying 1D spectral analysis techniques.

Spectral analysis techniques were initially developed for far field narrow band configurations. So to use these techniques with GPR data obtained in near field wide band, required the necessary adjustment in order to facilitate the accuracy of the Specan methods. The compensation of near field wide band effects was done by using focusing algorithm in this thesis back-projection focusing method was used. Then the Specan methods were applied on the focused data on a given selected range cell for azimuth resolution or azimuth cell for range resolution.

Moreover, from the state of the art, we have seen that Specan methods require the data to be uncorrelated or partially correlated. So in this research we have used a 2D spectral smoothing technique which allows to keep full length of an array hence facilitate high resolution capability of Specan methods.

The proposed algorithms have been validated by applying them on real life scenarios i.e measurement data where, the Specan methods showed high resolution ability to distinguish data with: reduced number of antennas, irregular azimuth samples, cluttered medium environment and dispersive medium environment.

This work led to two communications in international conferences and to an article to be submitted to an international journal.

4.2 Perspectives

Proposed future approach include the following:

First of all, the proposed algorithms in this thesis are 1D techniques. This implies they are are applied to specific selected azimuth cell or range cell. Therefore, in the future, these 1D techniques may be extended to 2D techniques in order to take into account all range cell or azimuth cell. this will allow the construction of GPR image with better resolution when compared to image developed with classical migration techniques.

Secondly, the proposed algorithm may be applied in medical field. For instance for detection of close blood vessels. This has been done partially during this

thesis. Due to confidential reasons detailed of configuration will not be disclosed but some of the initial results are presented in Fig. 4.1, where by the range focused image of the blood vessels is given in Fig. 4.1. The FK migration was used to focus the image and results are shown in Fig. 4.1b. Due to poor resolution of this conventional method, it was not possible to separate the two blood vessel present in the scene. To improve resolution, Specan methods were applied on the selected range cell as shown in Fig. 4.1b and the results are presented in Fig. 4.1c. The results show that only root based Specan methods and Multidimensional Specan methods were able to detect the two blood vessels.

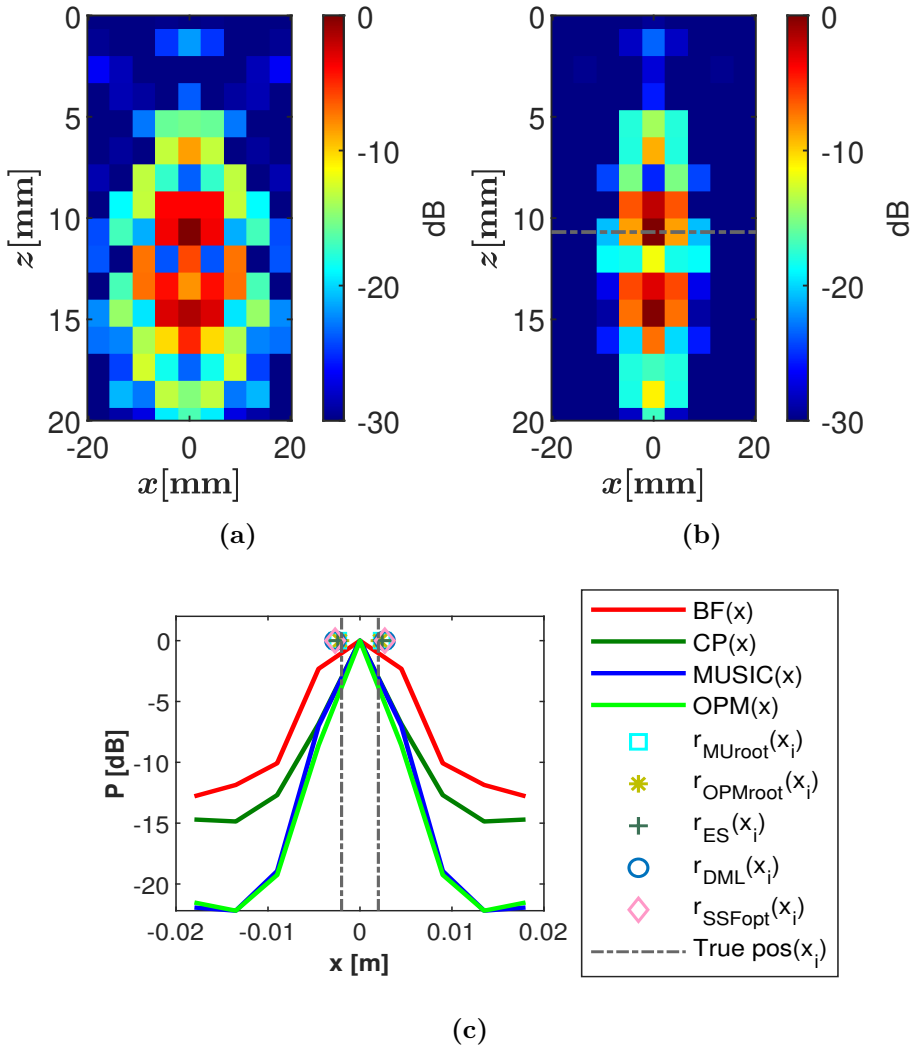

Figure 4.1: Measurement data with blood vessels: (a) Range focused measurement data, (b) BP focused results, (c) Specan objective functions.

Finally, the Specan techniques may be applied to detect targets that are buried in multi layers (layers with different permittivity) environment.

Appendix A

Appendix

The Specan methods may be categorised based on how they manipulate the covariance matrix to estimate the parameters as:

- Peak-search approaches
- Root methods approaches
- Multidimensional approaches

A.1 Peak search methods

These methods estimate parameter as coordinates of local maxima of continuous objective function. In this category we have Beamforming, Capon's method, MUSIC and Orthogonal Projector method (OPM).

A.1.1 Beamforming

The basic idea behind BF techniques is to "steer" the array in one direction at a time and measure the output power. When the "steered" direction coincides with a $\boldsymbol{a}(\omega)$ of the signal, the maximum output power will be observed [CGY10]. Given the knowledge of array steering vector, an array can be steered electronically just as a fixed antenna can be steered mechanically.

A weight vector $\boldsymbol{g}$ can be designed and then used to linearly combine the data received by the array elements to form a single output signal x:

$$x = \boldsymbol{g}^H \boldsymbol{y} \tag{A.1}$$

The total averaged output power of data with N realisation can be expressed as:

$$\begin{aligned} P(\boldsymbol{g}) &= \frac{1}{N}\sum_{n=1}^{N}|x|^2 = \frac{1}{N}\sum_{n=1}^{N}\boldsymbol{g}^H\boldsymbol{y}\boldsymbol{y}^H\boldsymbol{g} \\ &= \boldsymbol{g}^H\boldsymbol{R}\,\boldsymbol{g} \end{aligned} \tag{A.2}$$

In the convention beamforming approach, $\boldsymbol{g}$ has a response of an ideal scatterer hence $\boldsymbol{g} = \boldsymbol{a}(\omega)$ with $\boldsymbol{a}(\omega)$ being the steering matrix previously in equation (1.18). For each ω, the average power output $P(\omega)$ of the steered array is then measured or computed with (A.2). In other words, the output power versus ω is recorded with (A.2). It can be shown that When $\omega = \omega_m$, an impinging angle of the signal from source m, the output power $P(\omega)$ will reach a peak or maximum point. At this moment, $\boldsymbol{g} = \boldsymbol{a}(\omega - \omega_m)$ aligns the phases of the signal components received by all the elements of the array, causing them to add constructively and produce a maximum power. In practical computations, $\boldsymbol{g} = \boldsymbol{a}(\omega)$ is normalised as:

$$\boldsymbol{g} = \boldsymbol{g}_{BF} = \frac{\boldsymbol{a}(\omega)}{\sqrt{\boldsymbol{a}^H(\omega)\boldsymbol{a}(\omega)}} \tag{A.3}$$

By inserting the weight vector equation (A.3) into (A.2), the output power is obtained as [CGY10] :

$$\boldsymbol{P}_{BF} = \frac{\boldsymbol{a}^H(\omega)\hat{\boldsymbol{R}}\boldsymbol{a}(\omega)}{\boldsymbol{a}^H(\omega)\boldsymbol{a}(\omega)} \tag{A.4}$$

The weight vector (A.3) can be interpreted as a spatial filter; it is matched to the impinging spatial angles of the incoming signal to produce a peak but attenuate the output power for signals not coming from the angles of the incoming signals. Intuitively, it equalises the different signal delays experienced by the array elements and maximally combine their respective contributions to form a peak in output power at the angles of the incoming signals [CGY10].

BF is simple to implement but the width of the beam associated with a peak and the height of the sidelobes, are relatively large; they limit the method's effectiveness when signals arriving from multiple directions or sources are present. This technique has poor resolution. Although it is possible to increase the resolution of beamformer by adding more array elements due to the fact that width of the

beam associated with a peak and the height of the sidelobes reduce with increase of antenna elements. But this leads to the increase in the numbers of receivers and the amount of storage required for the data.

A.1.2 Capon beamformer

The beamforming described earlier use all the degrees of freedom available to the array in forming a beam in the required look direction. This works well when there is only one incoming signal present. But when there is more than one signal present, the array output power contains signal contributions from the desired angle as well as from the undesired angles [CGY10].

Capon's method overcomes this problem by using the degrees of freedom to form a beam in the look direction and at the same time the nulls in other directions in order to reject other signals [KV96].

In terms of the array output power, forming nulls in the directions from which other signals arrive can be accomplished by constraining a beam (or at least maintaining unity gain) in the look direction.

Thus, for a particular look direction, Capon's method uses all but one of the degrees of the freedom to minimise the array output power while using the remaining degrees of freedom to constrain the gain in the look direction to be unity:

$$\min P(\boldsymbol{g}) \text{ subject to } \boldsymbol{g}^H \boldsymbol{a}(\omega) = 1 \tag{A.5}$$

The resulting weight vector is shown to be given

$$\boldsymbol{g} = \boldsymbol{g}_{CP} = \frac{\boldsymbol{R}^{-1}\boldsymbol{a}(\omega)}{\boldsymbol{a}^H(\omega)\boldsymbol{R_{yy}}^{-1}\boldsymbol{a}(\omega)} \tag{A.6}$$

By substituting the above weight vector into (A.2), the following spatial power spectrum is obtained:

$$\boldsymbol{P}_{CP} = \frac{1}{\boldsymbol{a}^H(\omega)\hat{\boldsymbol{R}}^{-1}\boldsymbol{a}(\omega)} \tag{A.7}$$

CP Provides a better resolution in comparison with the conventional beamforming technique. But Capon's method fails if the signals that are correlated are present because it uses the correlation matrix $\boldsymbol{R_{yy}}^{-1}$, which becomes singular for the correlated signals. Hence, the correlated components will be combined destructively in the process of minimizing the output power. CP method requires the computation of a matrix inverse, which can be expensive for large arrays.

The common advantage of these two non-parametric methods is that they do not assume anything about the statistical properties of the data and, therefore, they can be used in situations where we lack information about these properties. On the other hand, in the cases where such information is available, for example in the form of a covariance model of the data, a nonparametric approach does not give the performance that one can achieve with a parametric (model based) approach.

A.1.3 MUSIC

The MUSIC algorithm was firstly proposed by Schmidt [Sch86], which started the era of high resolution technique. MUSIC applies the Eigenvalue decomposition (EVD) to the covariance matrix and gets its signal subspace and noise subspace. According to the orthogonality between these two subspaces, the MUSIC algorithm can successfully estimate the position parameters. The covariance matrix in (1.20) can be written in form of its eigenvalues and eigenvectors as [SM+05; Mar+98; Sun+19]:

$$\boldsymbol{R} = \boldsymbol{V}_s \boldsymbol{\Lambda}_s \boldsymbol{V}_s^H + \sigma^2 \boldsymbol{V}_n \boldsymbol{\Lambda}_n \boldsymbol{V}_n^H \tag{A.8}$$

$\boldsymbol{\Lambda}_s$ is the diagonal matrix containing the L largest eigenvalues with their associated eigenvectors in the columns of $\boldsymbol{V}_s$ (the matrix of signal eigenvectors), $\boldsymbol{\Lambda}_n$ is a diagonal matrix containing the $M - L$ smallest eigenvalues, with their associated eigenvectors arranged in $\boldsymbol{V}_n$ (the matrix of noise eigenvectors) and σ^2 is the noise variance. The MUSIC principle is based on the fact that $\boldsymbol{V}_n$ is orthogonal to $\boldsymbol{V}_s$ and, consequently, to the mode matrix $\boldsymbol{A}$ such that:

$$\boldsymbol{V}_n^H \boldsymbol{a}(\omega) = 0, \quad \omega \in \{\omega_1, ..., \omega_M\} \tag{A.9}$$

Therefore, the MUSIC pseudospectrum is then defined as [Sun+19]:

$$P_{MUSIC}(\omega) = \frac{1}{\boldsymbol{a}^H(\omega)\boldsymbol{V}_n\boldsymbol{V}_n^H\boldsymbol{a}(\omega)} \tag{A.10}$$

The ω_m of the multiple incident signals can be estimated by locating the peaks of $(A.10)$. The m largest peaks in the MUSIC spectrum above correspond to the ω_m of the signals impinging on the array. MUSIC has high resolution compared to BF and CP but it uses EVD which involve a large computational burden.

A.1.4 Orthogonal Projector Method

To solve the problem of large computational burden of MUSIC which comes from the use of EVD, propagator-based techniques such as the orthogonal propagator method (OPM), are proposed to estimate the position parameters by using linear operations without EVD or singular value decomposition (SVD). The OPM is based on the structure of the covariance matrix $\boldsymbol{R}$ which partitions the steering matrix $\boldsymbol{A}$ into submatrices [Mar+98]:

$$\boldsymbol{A} = \begin{bmatrix} \boldsymbol{A_1} \\ \boldsymbol{A_2} \end{bmatrix} \tag{A.11}$$

Where $\boldsymbol{A_1}$ and $\boldsymbol{A_2}$ are $L \times L$ and $(K-L) \times L$-dimensional matrices, respectively. There exists a $L \times (K-L)$-dimensional linear operator $\boldsymbol{P}$, such that $\boldsymbol{P}^H\boldsymbol{A_1} = \boldsymbol{A_2}$ or $\boldsymbol{Q} = [\boldsymbol{P}^H, \boldsymbol{I}_{K-L}]^H$ where $\boldsymbol{I}_{K-L}$ is an $(K-L) \times (K-L)$-dimensional identity matrix. Similar to MUSIC $\boldsymbol{Q}_0$ may be defined as $\boldsymbol{Q}_0 = \boldsymbol{Q}(\boldsymbol{Q^H Q})^{-1/2}$ which is orthogonal to $\boldsymbol{A}$ as given below:

$$\boldsymbol{Q}_0^H\boldsymbol{a}(\omega) = 0, \quad \omega \in \{\omega_1, ..., \omega_M\} \tag{A.12}$$

As a result OPM pseudospectrum is given as [Mar+98]:

$$P_{OPM}(\omega) = \frac{1}{\boldsymbol{a}^H(\omega)\boldsymbol{Q_0}\boldsymbol{Q_0}^H\boldsymbol{a}(\omega)} \tag{A.13}$$

The position parameters can then be estimated by searching the peak positions of (A.13). Since $\boldsymbol{A}$ is full rank, the linear operator $\boldsymbol{P}$ is unique. On the other

hand $\boldsymbol{P}$ is generally unknown in reality but can be estimated from the property of covariance matrix as [Mar+98]: $\boldsymbol{P} = (\boldsymbol{A_1}^H \boldsymbol{A_1})\boldsymbol{A_1}^H \boldsymbol{A_2}$. However, propagator-based methods are developed with signal models under ideal conditions and without the consideration of noise. Hence, their performance is degraded in low-SNR scenarios [Sun+19].

A.2 Roots methods

These methods do not involve an exhaustive search through all possible steering vectors to estimate parameter positions. Instead they perform estimation by finding the roots of a polynomial of the objective function, thus they provide direct parameter estimation. This reduces the computation load and storage requirements in large extent compared to Peak-search approaches.

A.2.1 Root-MUSIC

The Root-MUSIC is the polynomial-rooting version of (A.10), the previously described MUSIC technique. Unlike MUSIC which involves plotting the pseudospectrum against the angles and searching for the peaks, Root-MUSIC involves finding the roots of a polynomial. Starting with the pseudospectrum of MUSIC algorithm given in equation $(A.10)$.

$$P_{MUSIC}(\omega) = \frac{1}{\boldsymbol{a}^H(\omega)\boldsymbol{C}\boldsymbol{a}(\omega)} \tag{A.14}$$

By defining $\boldsymbol{C} = \boldsymbol{V}_n \boldsymbol{V}_n^H$, where $\boldsymbol{V}_n$ is noise subspace eigen vector matrix, the denominator of (A.14) can be rewritten as [WKL14]:

the $l{-}th$ element $a_l(\omega)$ of steering vector is defined as:

$$a_l(\omega) = e^{-jl\omega} \quad l = 0, ..., L-1 \tag{A.15}$$

The denominator, thus can be rewritten as:

$$\boldsymbol{a}^H(\omega)\boldsymbol{C}\boldsymbol{a}(\omega) = \sum_{l=0}^{L-1}\sum_{p=0}^{L-1} e^{-jl\omega} C_{lp} e^{jk\omega} = \sum_{q=-L+1}^{L-1} C e^{jq\omega} \tag{A.16}$$

Where C_q is the sum of the elements along the q_{th} diagonal of $\boldsymbol{C}$. Letting $z = e^{j\omega}$

in equation A.16 above simplifies to:

$$\boldsymbol{D}(z) = \sum_{\ell=-L+1}^{L-1} C_q z^q \tag{A.17}$$

The roots of $\boldsymbol{D}(z)$ that lie closest to the unit circle correspond to the poles of the MUSIC pseudospectrum. These $2(N-1)$ roots can be written as:

$$z_i = |z_i| e^{j \arg(z_i)}, \quad i = 1, 2, \ldots, 2(L-1) \tag{A.18}$$

Choosing those roots inside the unit circle whose magnitude $|z_i| \simeq 1$ and comparing $e^{j \arg(z_i)}$ to e^{jw} gives [WKL14]:

$$\omega_{MUroot_i} = \arg(z_i) \tag{A.19}$$

A.2.2 Root - OPM

Similar to Root-MUSIC, Root-OPM is the polynomial rooting version of (A.13), described in OPM technique. Therefore by defining $\boldsymbol{C} = \boldsymbol{Q}_0 \boldsymbol{Q}_0^H$, where $\boldsymbol{Q}_0$ is the estimated noise subspace by linear propagator P. Substituting $\boldsymbol{C}$ in (A.13) like previously explained in Root-MUSIC, the polynomial-rooting version of the OPM will be defined as[Mar+98]:

$$\omega_{OPMroot_i} = \arg(z_i), \quad i = 1, 2, \ldots, 2(L-1) \tag{A.20}$$

A.2.3 ESPRIT

ESPRIT stands for Estimation of Signal Parameters via Rotational Invariance Techniques which is another subspace based estimation algorithm. It does not involve an exhaustive search through all possible steering vectors to estimate source signals and hence reduces the computational and storage requirements in large extent compared to peak search methods.

The method relies on the property of the Eigen decomposition of the covariance matrix given in (A.8). The method define the sub-matrices $\boldsymbol{A_{1_u}}$ and $\boldsymbol{A_{2_d}}$ by

deleting the first and last rows from $\boldsymbol{A}$ in (1.19) respectively as [KV96]:

$$\boldsymbol{A} = \begin{bmatrix} \boldsymbol{A_{1_u}} \\ \\ \text{last row} \end{bmatrix} = \begin{bmatrix} \text{first row} \\ \\ \boldsymbol{A_{2_d}} \end{bmatrix} \tag{A.21}$$

Where by $\boldsymbol{A_{1_u}}$ and $\boldsymbol{A_{2_d}}$ are related by:

$$\boldsymbol{A_{2_d}} = \boldsymbol{A_{1_u}}\boldsymbol{\Phi} \tag{A.22}$$

Where $\boldsymbol{\Phi}$ is a diagonal matrix having the roots $e^{j\phi m}, m = 1, ..., M$ on the diagonal. Thus estimation parameters problem may be reduced to to that of finding $\boldsymbol{\Phi}$. The $\boldsymbol{V}_s$ in (A.8) can be partitioned conformably with $\boldsymbol{A}$ in (1.19) into the submatrices $\boldsymbol{V}_{s1}$ and $\boldsymbol{V}_{s2}$ such that:

$$\boldsymbol{V}_{s1} = \boldsymbol{A_{1_u}}\boldsymbol{T}, \quad \boldsymbol{V}_{s2} = \boldsymbol{A_{2_d}}\boldsymbol{T}, \tag{A.23}$$

$$\boldsymbol{T} = \boldsymbol{R_{ss}}\boldsymbol{A}^H\boldsymbol{V}_s(\Lambda_s - \sigma^2\boldsymbol{I})^{-1} \tag{A.24}$$

Where $\boldsymbol{T}$ is the full rank M matrix. Combining (A.22) and (A.23) yields:

$$\boldsymbol{V}_{s2} = \boldsymbol{A_{1_{up}}}\boldsymbol{\Phi}\boldsymbol{T}, \quad \boldsymbol{V}_{s1} = \boldsymbol{T}^{-1}\boldsymbol{\Phi}\boldsymbol{T}, \tag{A.25}$$

Which by defining $\boldsymbol{\Psi} = \boldsymbol{T}^{-1}\boldsymbol{\Phi}\boldsymbol{T}$, becomes

$$\boldsymbol{V}_{s2} = \boldsymbol{V}_{s1}\boldsymbol{\Psi} \tag{A.26}$$

Since $\boldsymbol{\Psi}$ and $\boldsymbol{\Phi}$ are related by similar transformation so they have the same eigenvalues. As the latter is given by $e^{j\phi m}, m = 1, ..., M$ and are related to the parameter estimation as in (A.19), we get [KV96]:

$$\omega_{ESPRIT_i} = \arg(z_i), \quad i = 1, 2, \ldots, 2(L-1) \tag{A.27}$$

Where by z is the root of the polynomial of $\boldsymbol{\Psi}$ eigenvalues.

A.3 Multi-dimensional methods

These methods perform estimation of parameters through the optimisation of concentrated criterion. They have improved accuracy of estimated parameters with exchange of heavy computational cost.

A.3.1 Deterministic Maximum Likelihood (DML)

DML estimate position parameters by maximising a likelihood function which is the probability density function (PDF) of all observation given unknown parameters. Given a finite data set $\boldsymbol{y}(t)$ observed over $t = 1, 2, ..., N$. Assuming that data are independent in data model presented in (1.17), the likelihood function is complex L-variate Gaussian given as [KV96]:

$$L_{DML}(\omega, \boldsymbol{s}(t), \sigma^2) = \prod_{t=1}^{N} (\pi\sigma^2)^{-L} e^{-\|\boldsymbol{y}(t) - \boldsymbol{A}_{(\omega)}\boldsymbol{s}(t)\|^2/\sigma^2} \tag{A.28}$$

where $\|\cdot\|$ denotes Euclidean norm. As indicated above, the unknown parameters in the likelihood function are the signal parameter ω, the source signal waveforms $\boldsymbol{s}(t)$ and the noise variance σ^2. The ML estimates of these unknowns are calculated as the maximising arguments of $L(\omega, \boldsymbol{s}(t), \sigma^2)$, the aim being that these values make the probability of the observation as large as possible. For convenience, the ML estimates are alternatively defined as the minimising arguments of the negative log-likelihood function -log$L(\omega, \boldsymbol{s}(t), \sigma^2)$. Normalising by N and ignoring the parameter-independent L log π-term, we get:

$$l_{DML}(\omega, \boldsymbol{s}(t), \sigma^2) = L \log \sigma^2 + \frac{1}{\sigma^2 N} \sum_{t=1}^{N} \|\boldsymbol{y}(t) - \boldsymbol{A}(\omega)\boldsymbol{s}(t)\|^2 \tag{A.29}$$

whose minimising arguments are the DML estimates. As well known, explicit minima with respect to σ^2) and $\boldsymbol{s}(t)$ are given by [KV96]:

$$\hat{\sigma}^2 = \frac{1}{L} Tr\{\Pi_A^{\perp} \boldsymbol{R}\}, \quad \Pi_A^{\perp} = \boldsymbol{I} - \Pi_A, \quad \Pi_A = \boldsymbol{A}\boldsymbol{A}^{\dagger}. \tag{A.30}$$

$$\hat{\boldsymbol{s}}(t) = \boldsymbol{A}^{\dagger}\boldsymbol{y}(t), \quad \boldsymbol{A}^{\dagger} = (\boldsymbol{A}^H \boldsymbol{A})^{-1} \boldsymbol{A}^H \tag{A.31}$$

Where $\boldsymbol{R}$ is the covariance matrix in (1.20), $\boldsymbol{A}^{\dagger}$ is the Moore-Penrose pseudo-inverse of $\boldsymbol{A}$ and $\Pi_A^{\perp}$ is the orthogonal projector onto the nullspace of $\boldsymbol{A}^H$. Substituting (A.30) and (A.31) in (A.28) shows that the DML parameter estimation are obtained by solving the following minimisation problem [KV96]:

$$\hat{\omega}_{DML} = \arg\{\min_{\omega} \mathrm{Tr}\{\Pi_A^{\perp}\boldsymbol{R}\}\} \tag{A.32}$$

To calculate the DML estimates, the non-linear M-dimensional optimisation problem (A.32) must be solved numerically and if the initial guess is poor, the search process may converge to local minimum and never reach the desired global minimum. A spectral-based method is a natural choice for initial estimator, provided all sources can be resolved. To reduce computational cost of this numerical optimisation problem in (A.32), Alternating projection technique of [ZW90] may be used.

A.3.2 Signal Subspace Fitting (SSF)

This method was introduced to overcome computational cost of DML method. SSF is based on the structure of Eigen decomposition of the data covariance matrix previously explained in (A.8). By expressing the identity in (A.8) as $\boldsymbol{I} = \boldsymbol{V}_s\boldsymbol{V}_s^H + \boldsymbol{V}_n\boldsymbol{V}_n^H$ and compare it to (A.8), the $\sigma^2\boldsymbol{V}_n\boldsymbol{V}_n^H$-term wil be cancelled and yields [KV96]:

$$\boldsymbol{A}\boldsymbol{R}_{\boldsymbol{ss}}\boldsymbol{A}^H + \sigma^2\boldsymbol{V}_s\boldsymbol{V}_s^H = \boldsymbol{V}_s\boldsymbol{\Lambda}_s^H\boldsymbol{V}_s^H \tag{A.33}$$

Post multiplying on the right by $\boldsymbol{V}_s$ (note that $\boldsymbol{V}_s^H\boldsymbol{V}_s = \boldsymbol{I}$) and re-arranging gives the relation:

$$\boldsymbol{V}_s = \boldsymbol{A}\boldsymbol{T} \tag{A.34}$$

Where $\boldsymbol{T}$ is full rank M matrix as defined previously in (A.23). The relation in (A.34) forms the basis of the SSF approach where by SSF estimate is obtained by solving the following non-linear optimisation problem given that F is the Frobenius norm:

$$\{\hat{\omega}, \hat{\boldsymbol{T}}\} = \arg\min_{\omega,T} \|\hat{\boldsymbol{V}}_s - \boldsymbol{A}\boldsymbol{T}\|_F^2 \tag{A.35}$$

Similar to DML criterion (A.29), this is a separable nonlinear least square problem [KV96]. The solution for the linear parameter $\boldsymbol{T}$ (for fixed known $\boldsymbol{A}$) is:

$$\hat{\boldsymbol{T}} = \boldsymbol{A}^{\dagger}\hat{\boldsymbol{V}}_s \tag{A.36}$$

Which when substituted to (A.35) leads to concentrated criterion function:

$$\hat{\omega} = \arg\{\min_{\omega} \mathrm{Tr}\{\Pi_A^{\perp}\hat{\boldsymbol{V}}_s\hat{\boldsymbol{\Lambda}}_s\hat{\boldsymbol{V}}_s^H\}\} \tag{A.37}$$

Since the eigenvectors are estimated with a quality, commensurate with the closeness of the corresponding eigenvalues to noise variance, it is natural to introduce a weighting of the eigenvectors and arrive at [KV96]:

$$\hat{\omega}_{SSF} = \arg\{\min_{\omega} \mathrm{Tr}\{\Pi_A^{\perp}\hat{\boldsymbol{V}}_s\boldsymbol{W}\hat{\boldsymbol{V}}_s^H\}\} \tag{A.38}$$

To maximise the accuracy following the theory of weighted least squares [GV80] $\boldsymbol{W}$, should be a diagonal matrix containing the inverse of the covariance matrix of $\Pi_A^{\perp}(\omega)\hat{\boldsymbol{v}}_k, k = 1, ..., M$. Given that σ^2 is the noise variance, we get [SS90] :

$$\hat{\boldsymbol{W}}_{opt} = \left(\hat{\boldsymbol{\Lambda}}_s - \sigma^2\boldsymbol{I}\right)^2 \hat{\boldsymbol{\Lambda}}_s^{-1} \tag{A.39}$$

The estimator defined by (A.38) with weighting given by (A.39) is termed Weighted Subspace Fitting (WSF) method. Alternative subspace fitting may be obtained by using MUSIC relation [KV96].

List of Publications

Journal Paper

1. Pamela Manase, Raffaelle D'Errico, Laurent Ferro-Famil, "Enhancing Ground Penetration Radar Imaging by using Spectral analysis Techniques in Near field wide band configurations", to be submitted

Conference Papers

1. Pamela Manase, Raffaelle D'Errico, Laurent Ferro-Famil,"Techniques à haute résolution pour l'imagerie par géoradar" La 22ème édition des Journées Nationales Microondes (JNM) Conférence.
2. Pamela Manase, Raffaelle D'Errico, Laurent Ferro-Famil, "High Resolution Focusing for Near-field GPR Imaging using Spectral Analysis Techniques" 2022 IEEE International Symposium on Antennas and Propagation and USNC-URSI Radio Science Meeting. (accepted with "HONORABLE MENTION")
3. Pamela Manase, Raffaelle D'Errico, Laurent Ferro-Famil, "Improving Azimuth Resolution of GPR with Small Array Aperture in Near Field".2022 International Conference on Radar Systems, Murrayfield Stadium, Edinburgh, UK

Bibliography

[BT06] I. Bekkerman and J. Tabrikian. "Target Detection and Localization Using MIMO Radars and Sonars." In: *IEEE Transactions on Signal Processing* 54.10 (2006), 3873–3883. DOI: 10.1109/TSP.2006.879267.

[BP15] Andrea Benedetto and Lara Pajewski. *Civil engineering applications of ground penetrating radar*. Springer, 2015.

[Cat15] Mathieu Cattenoz. "MIMO Radar Processing Methods for Anticipating and Preventing Real World Imperfections." Theses. Université Paris Sud - Paris XI, May 2015. URL: https://tel.archives-ouvertes.fr/tel-01197253.

[CGY10] Zhizhang Chen, Gopal Gokeda, and Yiqiang Yu. *Introduction to Direction-of-arrival Estimation*. Artech House, 2010.

[Cla85] Jon F Claerbout. *Imaging the earth's interior*. Vol. 1. Blackwell scientific publications Oxford, 1985.

[Con13] Lawrence B Conyers. *Ground-penetrating radar for archaeology*. AltaMira Press, 2013.

[Cou+07] Tegan Counts et al. "Multistatic ground-penetrating radar experiments." In: *IEEE transactions on geoscience and remote sensing* 45.8 (2007), 2544–2553.

[Cui+01] Tie Jun Cui et al. "Detection of buried targets using a new enhanced very early time electromagnetic (VETEM) prototype system." In:

IEEE Transactions on Geoscience and Remote Sensing 39.12 (2001), 2702–2712. DOI: 10.1109/36.975004.

[Dan04] David J Daniels. *Ground penetrating radar*. Vol. 1. Iet, 2004.

[DeG98] S.R. DeGraaf. "SAR imaging via modern 2-D spectral estimation methods." In: *IEEE Transactions on Image Processing* 7.5 (1998), 729–761. DOI: 10.1109/83.668029.

[Elb+05] F Elbahhar et al. "Comparison between DS-CDMA and modified Gegenbauer functions for a multiuser communication ultra-wideband system." In: *IEE Proceedings-Communications* 152.6 (2005), 1021–1027.

[Fis+06] E. Fishler et al. "Spatial Diversity in Radars—Models and Detection Performance." In: *IEEE Transactions on Signal Processing* 54.3 (2006), 823–838. DOI: 10.1109/TSP.2005.862813.

[Gaz78] Jenö Gazdag. "Wave equation migration with the phase-shift method." In: *Geophysics* 43.7 (1978), 1342–1351.

[GV80] Gene H Golub and Charles F Van Loan. "An analysis of the total least squares problem." In: *SIAM journal on numerical analysis* 17.6 (1980), 883–893.

[Góm14] Oscar Gómez. "Radar MIMO utilisant des antennes colocalisées : étude théorique, simulations et développement d'une plateforme expérimentale." Theses. Université Paris-Est, June 2014. URL: https://tel.archives-ouvertes.fr/tel-01124326.

[GGB00] G Grandjean, JC Gourry, and A Bitri. "Evaluation of GPR techniques for civil-engineering applications: study on a test site." In: *Journal of applied geophysics* 45.3 (2000), 141–156.

[Gra+11] Fabio Grasso et al. "GPR prospecting in Renaissance and baroque monuments in Lecce (Southern Italy)." In: *2011 6th International Workshop on Advanced Ground Penetrating Radar (IWAGPR)*. IEEE. 2011, 1–4.

[GY02] Jeroen Groenenboom and Alexander Yarovoy. "Data processing and imaging in GPR system dedicated for landmine detection." In: *Subsurface Sensing Technologies and Applications* 3.4 (2002), 387–402.

[HBC07] Alexander M Haimovich, Rick S Blum, and Leonard J Cimini. "MIMO radar with widely separated antennas." In: *IEEE signal processing magazine* 25.1 (2007), 116–129.

[Har+20] Lekhmissi Harkati et al. "Low complexity portable MIMO radar system for the characterisation of complex environments at high resolution." In: *IET Radar, Sonar & Navigation* 14.7 (2020), 992–1000.

[HE00] Jens F Hjelmstad and Egil S Eide. "3-D Imaging using Novel Techniques in Ultra-Wideband Radar." In: *2000 30th European Microwave Conference*. IEEE. 2000, 1–4.

[HB05] Bo Hu and Norman C Beaulieu. "Pulse shapes for ultrawideband communication systems." In: *IEEE Transactions on wireless communications* 4.4 (2005), 1789–1797.

[HF20] Yue Huang and Laurent Ferro-Famil. "3-D characterization of urban areas using high-resolution polarimetric sar tomographic techniques and a minimal number of acquisitions." In: *IEEE Transactions on Geoscience and Remote Sensing* 59.11 (2020), 9086–9103.

[JLZ12] Tian Jin, Jun Lou, and Zhimin Zhou. "Extraction of landmine features using a forward-looking ground-penetrating radar with MIMO array." In: *IEEE Transactions on Geoscience and Remote Sensing* 50.10 (2012), 4135–4144.

[Jol08] Harry M Jol. *Ground penetrating radar theory and applications*. elsevier, 2008.

[Jou+17] A. Jouade et al. "High resolution radar focusing using spectral estimation methods in wide-band and near-field configurations Application to millimeter-wave near-range imaging." In: *Progress In Electromagnetics Research B* 79 (2017), 45–64. DOI: 10.2528/PIERB17082402. URL: https://hal-univ-rennes1.archives-ouvertes.fr/hal-01739927.

[KV96] Hamid Krim and Mats Viberg. "Two decades of array signal processing research: the parametric approach." In: *IEEE signal processing magazine* 13.4 (1996), 67–94.

[Le 07] Cédric Le Bastard. "Apport de techniques de traitement du signal super et haute résolution à l'amélioration des performances du radar-chaussée." PhD thesis. UNIVERSITE DE NANTES, 2007.

[Le +08] Alice Le Gall et al. "An Imaging HF GPR Using Stationary Antennas: Experimental Validation Over the Antarctic Ice Sheet." In: *IEEE Transactions on Geoscience and Remote Sensing* 46.12 (2008), 3975–3986. DOI: 10.1109/TGRS.2008.2000718.

[LS96] Jian Li and P. Stoica. "An adaptive filtering approach to spectral estimation and SAR imaging." In: *IEEE Transactions on Signal Processing* 44.6 (1996), 1469–1484. DOI: 10.1109/78.506612.

[LS07] Jian Li and Petre Stoica. "MIMO radar with colocated antennas." In: *IEEE Signal Processing Magazine* 24.5 (2007), 106–114.

[Mar+98] Sylvie Marcos et al. "Les méthodes à haute résolution." In: *Hermes* 42 (1998).

[Mar17] Delphine Helena Natasha Marpaung. "Study of diversity techniques for ultra-wideband ground penetrating radar." PhD thesis. 2017. DOI: 10.32657/10356/72338.

[Mot06] Harold Mott. *Remote sensing with polarimetric radar*. John Wiley & Sons, 2006.

[Özd+14] Caner Özdemir et al. "A review on migration methods in B-scan ground penetrating radar imaging." In: *Mathematical Problems in Engineering* 2014 (2014).

[Pag+14] David W Paglieroni et al. "Imaging modes for ground penetrating radar and their relation to detection performance." In: *IEEE Journal of Selected Topics in Applied Earth Observations and Remote Sensing* 8.3 (2014), 1132–1144.

[Per14] Raffaele Persico. *Introduction to ground penetrating radar: inverse scattering and data processing*. John Wiley & Sons, 2014.

[Pie+06] M Pieraccini et al. "Advanced processing techniques for step-frequency continuous-wave penetrating radar: The case study of "Palazzo Vecchio" Walls (Firenze, Italy)." In: *Research in Nondestructive Evaluation* 17.2 (2006), 71–83.

[Sam+11] L Sambuelli et al. "Comparison between GPR measurements and ultrasonic tomography with different inversion algorithms: an application to the base of an ancient Egyptian sculpture." In: *Journal of Geophysics and Engineering* 8.3 (2011), S106–S116.

[ST09] Motoyuki Sato and Kazunori Takahashi. "Development of dual sensors and deployment in mine affected countries." In: *Anti-personnel Landmine Detection for Humanitarian Demining*. Springer, 2009, 27–44.

[Sat+14] Motoyuki Sato et al. "Archaeological survey by GPR for recovery from 3.11 Great Earthquake and Tsunami in East Japan." In: *Proceedings of the 15th International Conference on Ground Penetrating Radar*. IEEE. 2014, 25–30.

[Sch01] Bart Scheers. "Ultra-wideband ground penetrating radar with application to the detection of anti personnel landmines." In: *Royal Military Academy, Brussels* (2001).

[Sch86] Ralph Schmidt. "Multiple emitter location and signal parameter estimation." In: *IEEE transactions on antennas and propagation* 34.3 (1986), 276–280.

[SS10] Francesco Soldovieri and Raffaele Solimene. "Ground Penetrating Radar Subsurface Imaging of Buried Objects." In: *Radar Technology*. Ed. by Guy Kouemou. Rijeka: IntechOpen, 2010. Chap. 6. DOI: 10.5772/7176. URL: https://doi.org/10.5772/7176.

[Sol+11] Mercedes Solla et al. "GPR analysis of a masonry arch for structural assessment." In: *2011 6th International Workshop on Advanced Ground Penetrating Radar (IWAGPR)*. IEEE. 2011, 1–6.

[Sou99] Mehrdad Soumekh. *Synthetic aperture radar signal processing*. Vol. 7. New York: Wiley, 1999.

[SM+05] Petre Stoica, Randolph L Moses, et al. *Spectral analysis of signals*. Vol. 452. Pearson Prentice Hall Upper Saddle River, NJ, 2005.

[SS90] Petre Stoica and Kenneth C Sharman. "Maximum likelihood methods for direction-of-arrival estimation." In: *IEEE Transactions on Acoustics, Speech, and Signal Processing* 38.7 (1990), 1132–1143.

[Sto78] Robert H Stolt. "Migration by Fourier transform." In: *Geophysics* 43.1 (1978), 23–48.

[Sun+19] Meng Sun et al. "Advanced signal processing methods for ground-penetrating radar: Applications to civil engineering." In: *IEEE Signal Processing Magazine* 36.4 (2019), 74–84.

[Taf95] Allen Taflove. "Advances in finite-difference time-domain methods for engineering electromagnetics." In: *Ultra-Wideband, Short-Pulse Electromagnetics 2*. Springer, 1995, 381–401.

[War21] Craig Warren. "GprMax - Open Source Software to Simulate Electromagnetic Wave Propagation for Ground Penetrating Radar." In: 2021.1 (2021), 1–2. ISSN: 2214-4609. DOI: https://doi.org/10.3997/2214-4609.202152258. URL: https://www.earthdoc.org/content/papers/10.3997/2214-4609.202152258.

[WKL14] Njeri P Waweru, Dominic Bernard Onyango Konditi, and Philip Kibet Langat. "Performance analysis of MUSIC, root-MUSIC and ESPRIT DOA estimation algorithm." In: *International Journal of Electronics and Communication Engineering* 8.1 (2014), 209–216.

[Yar+07] Alexander G Yarovoy et al. "UWB array-based sensor for near-field imaging." In: *IEEE Transactions on Microwave Theory and Techniques* 55.6 (2007), 1288–1295.

[Yil01] Öz Yilmaz. *Seismic data analysis: Processing, inversion, and interpretation of seismic data*. Society of exploration geophysicists, 2001.

[Zen+15] Zhaofa Zeng et al. "Improving Target Detection Accuracy Based on Multipolarization MIMO GPR." In: *IEEE Transactions on Geoscience and Remote Sensing* 53.1 (2015), 15–24. DOI: 10.1109/TGRS.2014.2312937.

[Zha+13] Hui Zhang et al. "Radar subsurface imaging by phase shift migration algorithm." In: *2013 European Radar Conference*. IEEE. 2013, 531–534.

[ZY11] X Zhuge and AG Yarovoy. "Sparse multiple-input multiple-output arrays for high-resolution near-field ultra-wideband imaging." In: *IET microwaves, antennas & propagation* 5.13 (2011), 1552–1562.

[ZY10] Xiaodong Zhuge and Alexander G Yarovoy. "A sparse aperture MIMO-SAR-based UWB imaging system for concealed weapon detection." In: *IEEE Transactions on Geoscience and Remote Sensing* 49.1 (2010), 509–518.

[ZW90] Ilan Ziskind and Mati Wax. "Maximum likelihood localization of diversely polarized sources by simulated annealing." In: *IEEE Transactions on Antennas and Propagation* 38.7 (1990), 1111–1114.